

SEARCH FOR RESONANT PRODUCTION OF TOP ANTITOP PAIRS DECAYING
INTO MULTI-JETS AT THE COLLIDER DETECTOR AT FERMILAB

By
YURI OKSUZIAN

A DISSERTATION PRESENTED TO THE GRADUATE SCHOOL
OF THE UNIVERSITY OF FLORIDA IN PARTIAL FULFILLMENT
OF THE REQUIREMENTS FOR THE DEGREE OF
DOCTOR OF PHILOSOPHY

UNIVERSITY OF FLORIDA

2009

© 2009 Yuri Oksuzian

I dedicate this work to my parents, Artur and Valentina.

ACKNOWLEDGMENTS

First of all, I would like to express my sincere gratitude and deep appreciation to my advisors, Prof. Jacobo Konigsberg and Prof. Andrey Korytov, for their expertise, constant guidance, support, encouragement and inspiring discussions. In particular, I want to mention Andrey's priceless help in the early years of my graduate studies and Jacobo's dedication to his work and commitment to his students. These people tremendously helped me to develop as the physicist.

I would like to take this opportunity to thank Dr. Roberto Rossin and Dr. Alexander Sukhanov for sharing their knowledge in detector operations. Without their clear explanations and support, I would not be able to appreciate the beauty of the hardware part in high energy physics. They as well contributed in developing tools, which were widely used in my analysis.

I also thank all my friends from Tbilisi State University and from high school, who are now scattered all over the world, but still keep in touch. In particular, I will be forever grateful to Sergo Jindariani and Nicholas Sambelashvili, who helped in many aspects. Only with their help and suggestions, I was able to enter graduate school at University of Florida and to have a great opportunity work on my favorite subject. The influence I received from them helped me to develop as the better physicist and person in general. I would like to mention all the friends I met in Gainesville, Victor Barashko and Artem Nahapetyan in particular.

During my time at CDF, I drew much knowledge from interacting with many people such as Dr. Fabrizio Margaroli, Dr. Florencia Canelli, Dr. Daniel Whiteson, Dr. Nathan Goldschmidt, Dr. Alexandre Pronko and Dr. Song Ming Wang, who helped me greatly getting up to the speed of the experimental physics at CDF. Also I want to mention and thank Jim Lungu for many interesting discussions during our regular work outs we had.

In the end, I want to thank my parents, Artur Oksuzyan and Valentina Skubak, whom I dedicate this work. Without their constant love and support I could never have written this thesis.

TABLE OF CONTENTS

	<u>page</u>
ACKNOWLEDGMENTS	4
LIST OF TABLES	8
LIST OF FIGURES	9
ABSTRACT	11
CHAPTER	
1 INTRODUCTION	12
1.1 History of Elementary Particle Physics	12
1.2 The Standard Model	15
1.3 Beyond the Standard Model	17
1.4 Top Quark Physics	18
2 EXPERIMENTAL APPARATUS	25
2.1 Accelerator	25
2.1.1 Proton Source	25
2.1.2 Main Injector	26
2.1.3 Antiproton Source	26
2.1.4 Tevatron	27
2.2 The CDF II Detector	28
2.2.1 Tracking and Vertexing Systems	29
2.2.2 Calorimetry	33
2.2.3 Other Systems	34
2.2.4 Trigger System and Data Acquisition	38
2.2.5 Good Run Requirements	39
2.3 Jet Reconstruction	40
2.3.1 Jet Clustering	40
2.3.2 Jet Corrections	42
3 DATA SAMPLE AND EVENT SELECTION	52
3.1 Data and Monte Carlo Samples	52
3.2 Event Selection	53
3.2.1 Neural Net	56
3.2.2 QCD Background Modeling	58
4 FLAME ALGORITHM	70
4.1 Construction of the Likelihood	70
4.2 The Matrix Elements (ME)	71

4.3	Approximations. Change of Integration Variables.	73
4.4	Transfer Functions	73
4.4.1	$M_{t\bar{t}}$ Reconstruction	74
4.4.2	Signal and Background Templates	75
5	SENSITIVITY	78
5.1	Upper Limit Setting and Sensitivity Calculation	78
5.2	Method	78
5.3	Implementation	80
5.3.1	Templates	80
5.3.2	Templates Weighting	80
5.3.3	Z' Contamination in QCD Template	81
5.3.4	Data Structure and Algorithm	81
5.3.5	Calculation of Posterior	82
5.3.6	Cross Section Measurement & Limit Calculation	82
5.4	Systematic Errors Accounting	83
5.4.1	Shape Systematics	84
5.4.2	Jet Energy Scale	84
5.4.3	ISR & FSR	84
5.4.4	PDFs Uncertainty	85
5.4.5	Overall Shape Systematic Uncertainties	85
5.4.6	Incorporating the Shape Systematics	85
5.4.7	Expected Sensitivity With Shape Systematics	86
6	RESULTS	93
6.1	Conclusion	94
	REFERENCES	99
	BIOGRAPHICAL SKETCH	103

LIST OF TABLES

<u>Table</u>		<u>page</u>
1-1	List of most important particle discoveries led to deeper insight in the understanding of nature	23
1-2	Three quark generations	23
1-3	Three lepton generations	23
1-4	Force carriers	24
2-1	Summary of the current Tevatron performance characteristics.	28
2-2	Summary of quantities characterizing CDF calorimetry.	34
3-1	$t\bar{t}$ decay channels. l corresponds to electron or muon only	52
3-2	Number of events in the multi-jet data after the clean-up cuts and tagging. The integrated luminosity is $L = 2.8fb^{-1}$	55
3-3	Number of events in the SM $t\bar{t}$ Monte Carlo sample.	56
3-4	Number of events in the M_{X_0} Monte Carlo samples.	56
3-5	Table of acceptances for M_{X_0} Monte Carlo samples.	58
4-1	Definition of the binning in parton pseudo-rapidity for the transfer functions parameterization.	74

LIST OF FIGURES

<u>Figure</u>	<u>page</u>
1-1 Negative log probability	22
2-1 Overview of the Fermilab accelerator complex. The chain consists of several individual components: Proton Source (Cockcroft-Walton, Linac and Booster), Main Injector, Antiproton Source (Debuncher, Accumulator and Recycler) and the Tevatron. The detectors, CDF and D0, are also shown.	43
2-2 Beam structure at the Tevatron.	44
2-3 The total integrated luminosity delivered by the Tevatron from the beginning of Run II which started in April 2001.	44
2-4 The schematic cross-section view of the CDF detector.	45
2-5 The schematic r - z view of one quadrant of the CDF tracking system. Its components: Central Outer Tracker (COT) and the silicon detectors: Layer00 (L00), Silicon Vertex Detector (SVX), and Intermediate Silicon Layers (ISL) are shown.	46
2-6 Transverse view of the nominal cell layout for COT superlayer 2. The arrow shows the radial direction. The electric field is roughly perpendicular to the field panels. The magnetic field is perpendicular to the plane. The angle between wire-plane of the central cell and the radial direction is 35°	47
2-7 1/6th of the COT east end plate. Shown are the wire-plane slots grouped into eight superlayers.	47
2-8 SVX bulkhead design. Placement of ladders is shown in two adjacent wedges. . .	48
2-9 Schematic picture of one quadrant of the plug calorimeter including the electromagnetic and hadronic parts. The plug calorimeter has full 2π coverage and extends to $1.1 < \eta < 3.6$	49
2-10 The Cherenkov Luminosity Counter at CDF. The detector modules are located within the “3-degree holes” inside the forward and backward calorimeters. . . .	50
2-11 Functional block diagram of the CDF data flow. The crossing rate at the Tevatron is actually only 2.5 MHz, but the trigger system was designed for the originally envisioned 7.5 MHz crossing.	51
2-12 The ratio $\beta = p_T^{probe}/p_T^{trigger}$ of transverse momenta of the “probe” and the “trigger” jets using the 70 GeV jet trigger, obtained using two different methods (missing E_T projection fraction and dijet balancing. The “probe” trigger jet has to be in a central region $0.2 < \eta < 0.6$, while the probe jet may be anywhere in the calorimeter.	51
3-1 Negative log probability	59

3-2	Neural net input variables	60
3-3	Neural net input variables	61
3-4	Neural net Structure	62
3-5	Neural net training	62
3-6	Neural net training	62
3-7	Neural net training	63
5-1	Linearity test. The top plots show the input versus the reconstructed cross section after 1000 PEs at integrated luminosity $\int \mathcal{L} = 1000 \text{ pb}^{-1}$. Bottom plots shows deviation from linearity in expanded scale. We estimate the deviation to be about 2%(Red dotted line).	86
5-2	Posterior probability function for the signal cross section. The most probable value is assumed as estimator for the cross section. From the posterior we also extract 95% CL upper limit and lower limit. The red arrow and the quoted value correspond to the 95% CL UL_0	87
5-3	Cross section shift due to JES uncertainty for luminosity scenarios $\int \mathcal{L} = 2.8 \text{ fb}^{-1}$.The shift is assumed to be the uncertainty on the cross section due to JES.	88
5-4	Cross section shift due to ISR and FSR uncertainties.	89
5-5	Total shape systematic uncertainty versus input signal cross section.	90
5-6	Posterior probability function for the signal cross section. The smeared p.d.f. (green) shows a longer tail than the unsmeared one (black). As a consequence the UL_0 quoted on the plot is shifted to higher values with respect to the one calculated on unsmeared posterior.	91
5-7	Upper limits at 95% CL. The curves shows the results for two luminosity scenarios and both including or excluding the contribution from shape systematic uncertainties.	92

Abstract of Dissertation Presented to the Graduate School
of the University of Florida in Partial Fulfillment of the
Requirements for the Degree of Doctor of Philosophy

SEARCH FOR RESONANT PRODUCTION OF TOP ANTITOP PAIRS DECAYING
INTO MULTI-JETS AT THE COLLIDER DETECTOR AT FERMILAB

By

Yuri Oksuzian

December 2009

Chair: Jacobo Konigsberg

Major: Physics

We performed a search for “*non-standard model $t\bar{t}$ resonances in the all jets final state channel.*” The main goal was to examine top-antitop invariant mass spectrum for the presence of narrow resonant states. The data analysis used $2.8fb^{-1}$ of CDF data; events were produced at the Tevatron collider in $p\bar{p}$ collisions with center-of-mass energy of 1.96 TeV. 2086 data events were analyzed and compared to Standard Model expectation. No evidence for new $t\bar{t}$ resonant production mechanisms was found. Upper limits were placed on the cross-section times branching ratio for resonance production at $805\text{ GeV}/c^2$. For signal modeling we considered leptophobic Z' boson in a topcolor-assisted technicolor model with the width of $\Gamma = 1.2\%M_{X0}$.

CHAPTER 1 INTRODUCTION

1.1 History of Elementary Particle Physics

The idea that all matter is composed of elementary objects was proposed by ancient Greek philosophers: Leucippus, Democritus, and Epicurus, who believed that nature is composed of small $\alpha\tau o\mu o\xi$, meaning invisible. Later, in 19th century J.Dalton concluded that each element of nature was composed of a single, unique type of particle which was promptly named atom. One of the philosophical motivations behind this theory was the reductionist desire to explain the diversity of matter by the existence of few fundamental and indivisible particles. In the second half of the century, the Russian chemist D. Mendeleev classified the elements according to their chemical properties, he noticed patterns that led him to postulate his Periodic Table. However, near the end of the century, physicists discovered that atoms were not the fundamental particles of nature. In 1897, J.J. Thomson discovered the electron and measured its charge to mass ratio. Also he proposed his plum-pudding model of the atom, where the electrons are small, negatively charged and distributed inside the massive, positively charged atom. It was already known that some atoms decay spontaneously producing three types of radiations: α -rays, β -rays, bent significantly in a magnetic field, and γ -rays, not affected by the magnetic field. Therefore the atoms were no longer seen as fundamental.

In 1900, working on the problem of black body radiation, Max Planck postulated that electromagnetic energy could be emitted only in quantized form. In other words, the energy could only be a multiple of an elementary unit $E = h\nu$, where $h = 6.625 \times 10^{-34} Js$ is Planck's constant and ν is frequency of the radiation. In 1905, Einstein found the explanation of the photoelectric effect, which was another proof of quantum theory of light.

In 1909, Rutherford through his discovery and interpretation of α -particles scattering in his gold foil experiment, discovered that atoms have their positive charge concentrated

in a very small nucleus. He stated: "For concreteness, consider the passage of a high speed Alpha particle through an atom having a positive central charge Ne , and surrounded by a compensating charge of N electrons."

However, In Rutherford's model, the electron will release electromagnetic radiation while orbiting a nucleus according to the classical theory of electromagnetism. Because the electron would lose energy, it would gradually spiral inwards, collapsing into the nucleus. To overcome this difficulty, Niels Bohr proposed, in 1913, what is now called the Bohr model of the atom. He suggested that electrons could only travel in special orbits. The electron can move from one orbit to another by releasing or receiving a photon with an energy equal to the energy difference between the orbits.

In 1926, Schrodinger published his famous matter wave equation, which gave the correct energy eigenvalues for the hydrogen-like atom. Simultaneously, Heisenberg introduced the uncertainty principle which helped explain the concept of matter as both waves and particles. This constitutes the starting point of the quantum mechanics.

In 1928, relativistic quantum mechanical wave equation was formulated by British physicist Paul Dirac which provides a description of elementary spin- particles, such as electrons, consistent with both the principles of quantum mechanics and the theory of special relativity. The Dirac equation demands the existence of negative energy states which lead to the prediction of antiparticles. In 1931, Anderson discovered the positron, the anti-particle of the electron. In 1955, and a year later antiproton and antineutron was discovered.

In 1935, Yukawa published his theory of mesons and tried to explain the bound states of protons and the neutrons inside the nucleus via strong force. To account for all possible interactions between the nucleons it was expected that the pion exists in three charge states: positive, neutral and negative. In 1937, Anderson observed a new particle, but it wasn't exhibiting the expected properties of the pion. Therefore the scientists decided

that the new particle wasn't the pion, but a different new particle they called the muon, denoted μ .

In 1934, Enrico Fermi introduced a weaker version of the nuclear force in order to explain β decay of nuclei. A neutron spontaneously decays into an electron and a proton with the half-life of about 10 minutes, which can not be associated with the strong or electromagnetic force. It was observed as well that energy was not conserved during β decay. It was explained by the existence of a new particle, neutrino, which takes away the extra energy and escapes undetected. It was later discovered by Reines in 1956.

In 1950's, after discoveries of pions and kaons it became obvious that they could not all be elementary particles. In 1964, Gell-Mann and Zweig introduced the quark model containing three varieties of quarks: up, down and strange. All hadrons were classified as either mesons or baryons where two or three quarks are combined respectively.

In 1962, Lederman, Schwartz and Steinberger discovered muon-neutrino. The existence was motivated by leptonic charge conservation, which prevents a muon decay into an electron and photon.

In 1963, Sheldon Glashow proposed that the weak nuclear force, electricity and magnetism could arise from a partially unified electroweak theory. In 1967, Abdus Salam and Steven Weinberg independently revised Glashow's theory. This unified theory was governed by the exchange of four particles: the photon for electromagnetic interactions, a neutral Z particle and two charged W particles for weak interaction. As a result of the spontaneous symmetry breaking, the weak force becomes short range and the Z and W bosons acquire masses of 80.4 and 91.2 GeV/c^2 , respectively. In 1983, the Z and W bosons were first produced at CERN by Carlo Rubbia.

In 1964, we had three quarks - u , d , s , and four leptons - electron and muon with their neutrinos as well as all antiparticles. At this point, physicists started believing in the existence of a fourth quark. In 1970, G.I.M.(Glashow, Iliopoulos, Maiani) mechanism was proposed, which provided suppression for $\Delta S = 2$ transitions, as well as F.C.N.C.

processes in the weak interactions. As a consequence, fourth quark was introduced. In 1974, Richter and Ting found the charm-anticharm meson called J/Ψ .

In 1976, Martin Perl discovered first particle of the third generation, τ lepton. In 1977, a group of physicists led by Leon Lederman observed a Υ meson, which is a meson formed from a bottom (b) quark and its antiparticle. It was the first confirmation of the existence of third generation quark. In 1989, the experiments at SLAC and CERN strongly supported the hypothesis of only three generations of fundamental particles by measuring the lifetime of Z^0 -boson. In 1995, Fermilab collaboration made an observation of the remaining third generation quark, top quark (t). In 2000, the third generation was complete by the discovery of tau neutrino.

As a summary, we list all major discoveries in elementary particles physics in the table [1-1](#)

1.2 The Standard Model

The Standard Model is the quantum field theory, which describes three¹ fundamental interactions between the elementary particles that make up all matter. As of today, almost all experimental results have agreed with their Standard Model predictions. The Standard Model is based on the principle of the local gauge invariance of the group $SU(3)_c \times SU(2)_L \times U(1)_Y$. $SU(3)_c$ represents the symmetry group of the strong interaction while $SU(2)_L \times U(1)_Y$ represents the symmetry group of the unified electroweak interaction.

The Standard Model consists of elementary particles grouped into two classes: bosons (particles that transmit forces) and fermions (particles that make up matter). The bosons have particle spin that is either 0, 1 or 2. The fermions have spin 1/2.

The fundamental fermionic constituents of matter are quarks and leptons. Having spin 1/2, they follow the Pauli exclusion principle in accordance with the spin-statistics

¹ Gravity is not included in the Standard Model.

theorem giving them their material quality. Quarks, but not leptons, engage in the strong interaction as a consequence of their color charge - red, green or blue. The quarks, fall into two classes according to their charge. Up-type quarks(u, c, t) have electric charge $+2/3$ and down-type quarks(d, s, b) have charge $-1/3$, enabling both classes to participate in electromagnetic interactions as well.

Similar to quarks, there are three lepton types: electron(e, ν_e), muon(μ, ν_μ) and tau(τ, ν_τ). They fall into two classes according to electric charge, the neutral neutrinos(up-type) (ν_e, ν_μ, ν_τ), and the negatively charged(down-type) (e^-), (μ^-), (τ^-). Only the down-type leptons participate in electromagnetic interactions. The properties of quarks and leptons are listed in tables 1-2 and 1-3.

The force-mediating particles described by the Standard Model all have an intrinsic spin whose value is 1, making them bosons. As a result, they do not follow the Pauli Exclusion Principle. The photons mediate the familiar electromagnetic force between electrically charged particles (these are the quarks, electrons, muons, tau, W -boson). They are massless and are described by the theory of quantum electrodynamics. The W and Z gauge bosons mediate the weak nuclear interactions between particles of different flavors (all quarks and leptons). They are massive, with the Z -boson being more massive than the W -boson. These three gauge bosons along with the photons are grouped together which collectively mediate the electroweak interactions, as described by the Glashow-Salam-Weinberg (GSW) theory. Each quark carries any one of three color charges - red, green or blue, enabling them to participate in strong interactions mediated by the eight gluons. Gluons are massless. The eight-fold multiplicity of gluons is labeled by a combinations of color and an anticolor charge. Because the gluon has an effective color charge, they can interact among themselves. The gluons and their interactions are described by the theory of quantum chromodynamics (QCD). The properties of gauge bosons are summarized in the table 1-4.

The only particle predicted by Standard Model yet to be discovered is the Higgs boson (H). This boson plays a key role in explaining the origins of the mass of other elementary particles, in particular the difference between the massless photon and the very heavy W and Z bosons. It is also needed to give fermions their masses. Masses arise in a gauge invariant way, due to a process known as the Higgs mechanism [1]. In this mechanism, the local $SU(2)_L \times U(1)_Y$ symmetry of the electroweak interactions is spontaneously broken. This aspect of the theory correctly predicts the existence of the weak gauge bosons as well as the ratio of their masses. It also predicts the existence of a spin 0 particle: the Higgs boson. The search for the Standard Model Higgs boson remains one of the top priorities at the Tevatron and the future LHC experiments.

To date, almost all experimental tests of the three forces described by the Standard Model have agreed with its predictions. The most impressive is the agreement between the predicted and measured values of the W and Z gauge bosons masses. The Standard Model predictions have also lead to the discovery of top quark at the Tevatron. Still, the Standard Model falls short of being a complete theory of fundamental interactions, primarily because of its lack of inclusion of gravity, but also because of the large number of numerical parameters (such as masses and coupling constants) that must be put “by hand” into the theory rather than being derived from first principles.

1.3 Beyond the Standard Model

The Standard Model has managed to explain very well a vast amount of experimental data, however there are reasons to believe it is an incomplete theory

- Gravity is left out altogether
- The observed masses of particles are completely unexplained. The Higgs mechanism is just a way by which particles would ”acquire” mass.
- The gauge anomaly of the electroweak theory is canceled only if we have an equal number of quark and lepton generations, and the charges of the particles within one generation obey a certain constraint equation. This implies that there is some deeper

connection between quark and leptons which might also explain why we have only three generations.

- Besides particle masses, there are still quite many arbitrary parameters in the Standard Model, like the relative strengths of the interactions, the Weinberg angle $\sin(\theta_W)$, the elements of the Cabibbo-Kobayashi-Maskawa matrix which describes the strength of cross-generation direct coupling of quarks via charged currents.
- There are significant indications that neutrinos oscillate.
- The amount of known matter in the Universe is less than what would be necessary to produce a flat geometry as observed, and it is believed that there must exist other types of matter, dark matter, besides a non-zero cosmological constant or dark energy, which would explain the discrepancy. But these conclusions rely on the validity of General Relativity in describing the Universe as a whole, which is not quite obvious. Many theories beyond the Standard Model have been proposed, like Supersymmetry, String theories, Grand Unified Theories (GUTs), extra dimensions theories, Technicolor, quark compositeness theories and others. Some are basically impossible to test at current available energies, but most have a large parameter space and it is difficult to rule them out completely. In this work we decided to adopt a model independent approach to our search for Physics beyond the Standard Model, at least as much as it is possible.

1.4 Top Quark Physics

Top quark was discovered by the CDF and D0 experiments in 1995 [2]. The existence of an isospin partner for the b -quark is strongly motivated by arguments of theoretical consistency of the Standard Model, absence of flavor changing neutral current in B meson decays and studies of Z boson decays [3]. However, the large mass of the top quark, nearly $175 \text{ GeV}/c^2$, was in itself a surprise at the time. In this regard, the top quark separates itself from all other quarks. For example, it is the most massive fermion by a factor of nearly 40 (the bottom being the closest competitor).

Here we present some of the measurements which both confirm the Standard Model nature of the top quark and serve as tests of the Standard Model itself:

- $t\bar{t}$ production cross section

An accurate measurement of the $t\bar{t}$ production cross section is the precision test of the Standard Model. A cross section significantly higher than the theoretical expectation would be a sign of non-Standard Model mechanisms, for example the decay of a heavy resonant state into $t\bar{t}$ pairs. The excess observed with respect to the background in the various channels translates immediately into measurements of the pair production cross section. The value obtained from the combination of the measurements in the various channel led to the 1992-1995 (Run I) measurement of $t\bar{t} = 7.5_{-1.6}^{+1.9}$ pb to be compared with the theoretical cross section calculation by Laenen et al. [36] of 4.8 pb at $176 \text{ GeV}/c^2$. The apparent disagreement between theoretical and experimental values has vanished with the most recent theoretical calculation and the 2002-2009 measurement (Run II) performed combining the various decay modes, as can be seen in Fig. 1-1.

- Single top production

The CDF and D0 Collaborations recently presented the first observation for the production of single top quarks at the Tevatron [10]. The total integrated luminosity included in CDF's analysis is 3.2 fb^{-1} and D0's analysis has 2.3 fb^{-1} . A Bayesian analysis is used to extract the cross section from the distributions of multivariate discriminants provided by the collaborations. For a top quark mass $m_t = 170 \text{ GeV}/c^2$, they measure a cross section of $2.76_{-0.47}^{+0.58} \text{ pb}$. They extract the CKM matrix element $|V_{tb}| = 0.88 \pm 0.07$ with a 95% C.L. lower limit of $|V_{tb}| > 0.77$.

- Top quark charge

The most recent analyses on CDF presents a measurement of the electric charge of the top quark using soft lepton tagging. They trigger on high P_T leptons and reconstruct lepton+jet events offline. The analysis uses 2.7 fb^{-1} of good silicon data.

They require events to have two b tagged jets, one using SECVTX and the other using SLT tags (SLT_e and SLT). A kinematic fitter is used to determine which b-jet is associated with the leptonically decaying W and which is associated with the hadronically decaying W. Combining the information of the charge of the SLT tag, and the charge of the associated high P_T lepton determines whether the top has a charge of $2/3$ or $-4/3$. With this method, they find 29 events consistent with the standard model and 16 events consistent with a $-4/3$ charge top quark. This results in a 95% exclusion of the $-4/3$ charge hypothesis.

- $t \rightarrow Wq$ branching ratio

A measurement of the ratio of top quark branching fractions $R = BR(t \rightarrow Wb)/BR(t \rightarrow Wq)$ using lepton+jets and dilepton data sets has been performed by the CDF collaboration. This measurement is derived from the relative numbers of $t\bar{t}$ events with different multiplicity of identified secondary vertices, setting a lower limit of $R > 0.61$ at 95% confidence level.

- W helicity in top quark decays

The top quark is predicted by the Standard Model to decay into a bottom quark and a W boson by the electroweak interaction. The spin-one W boson can have 3 different helicities or orientations of its spin relative to the direction of motion. Due to heavy top quark mass relative to the W boson mass, the top decays mostly to a longitudinal W boson(70%). However, because the weak interaction violates parity maximally, the remaining time it decays to left-handed W bosons(30%). The purpose of this analysis is to test whether the $V - A$ rule holds true for the top quark. By taking advantage of a relationship between the helicity of the W boson, and the invariant mass of the charged lepton from the W decay and the b quark from the top decay, it is possible to distinguish between left-handed and right-handed W bosons. The measured helicity fraction is consistent with the Standard Model.

All of the above measurements test our knowledge of the production and decay mechanism in the framework of the Standard Model theory of fundamental interactions. No discrepancy has yet been observed in the top quark sector.

Interestingly, the top quark can be used as a mean to explore physics at the highest achievable mass scale. Looking at its production and decay mechanism, one can find hints of new physics to show up, for example, in possible resonant production. A number of measurements have been performed setting limits to new particle production:

- $t \rightarrow H^+ b$ branching ratio

Extensions of the Standard Model predict the existence of charged Higgs bosons (H^\pm). In such models the branching ratio $BR(t \rightarrow H^+ b)$ can be large thus competing with the Standard Model decay ($t \rightarrow Wb$). This search is based on the cross section measurements of $t\bar{t}$ production in three exclusive decay channels: the dilepton, lepton+jets and lepton+ τ channels. Assuming the charged Higgs decays into $c\bar{s}$, $\tau\nu$, t^*b and Wh^0 , limits to the ($t \rightarrow H^+ b$) branching ratio are obtained.

- Search for resonant $t\bar{t}$ production

Both CDF and D0 collaborations performed multiple searches for non-Standard Model resonant production of $t\bar{t}$ pairs in the lepton+jets channel. The $t\bar{t}$ invariant mass ($M_{t\bar{t}}$) is reconstructed and the resulting distribution is then tested for possible resonant production (X_0). One of the analysis was performed by University of Florida group at CDF. The data set corresponds to integrated luminosity of $680 pb^{-1}$ of data collected at Fermilab during Run II. 95% confidence level upper limits on the cross section times branching ratio were set. Assuming a specific topcolor-assisted technicolor production model, the leptophobic Z' with the width of $\Gamma = 0.012 M_{X_0}$, we exclude the mass range of $M_{X_0} < 725 \text{ GeV}/c^2$ at 95% confidence level.

- Search for a massive top

The CDF collaboration searched for the heavy top quark (t') pair production decaying to $W q$ final states in lepton+jets events. Masses below 311 GeV/c² have been excluded for Standard Model fourth-generation (t') quark at 95% C.L.

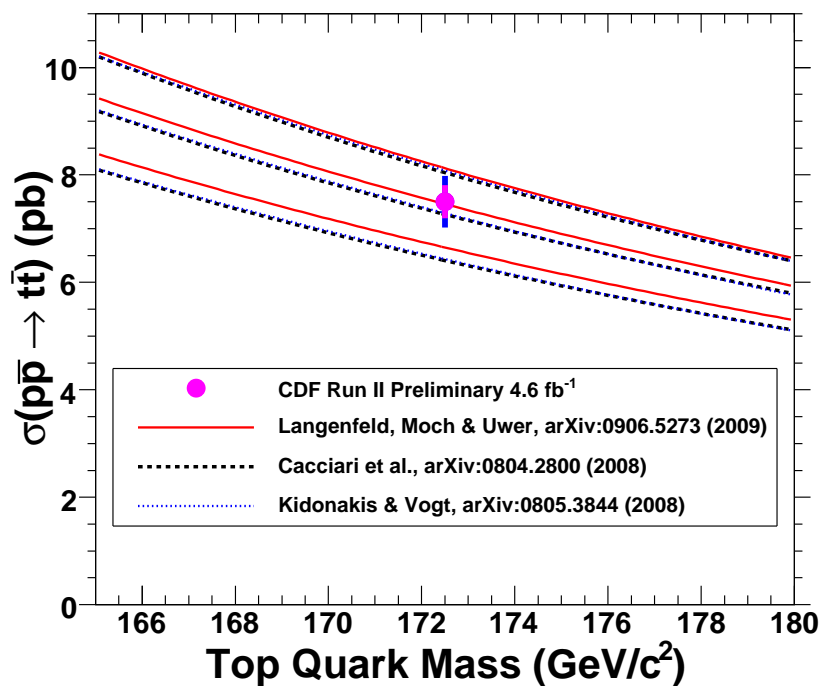


Figure 1-1. Combination of Preliminary Results compared to theoretical predictions as a function of top quark mass. A top quark mass value of 172.5 GeV is assumed for the experimental result

Particle	Year	Nobel Prize	Method
e^-	1879	Thomson	Discharge in gases
p	1919	Rutherford	Natural radioactivity
n	1932	Chadwick	Natural radioactivity
e^+	1933	Anderson	Cosmic Rays
μ^\pm	1937	Neddermeyer, Anderson	Cosmic Rays
π^\pm	1947	Powell, Occhialini	Cosmic Rays
K^\pm	1949	Powell	Cosmic Rays
π^0	1949	Bjorklund	Accelerator
K^0	1951	Armenteros	Cosmic Rays
ν_e	1956	Cowan, Reines	Nuclear reactor
ν_{μ}	1962	Lederman	Accelerator
J/ψ (c quark)	1975	Ting, Richter	Accelerator
τ	1974-77	Perl	Accelerator
Υ (b quark)	1977	none (E288 collaboration)	Accelerator
W^\pm, Z^0	1984	Rubbia, van der Meer	Accelerator
t quark	1995	none (CDF & D0 collaboration)	Accelerator
ν_τ	2000	none (DONUT (E872) collaboration)	Accelerator

Table 1-1. List of most important particle discoveries led to deeper insight in the understanding of nature

Quark	Electric charge (e)	Mass (MeV/c^2)
u up	+2/3	1.4-4
d down	-1/3	4-8
s strange	-1/3	80-130
c charm	+2/3	$1.15 - 1.35 \times 10^3$
b beauty	-1/3	$4.1 - 4.9 \times 10^3$
t top	+2/3	173.1×10^3

Table 1-2. Three quark generations

Lepton	Electric charge (e)	Mass (MeV/c^2)
e	-1	0.51099892
ν_e	0	$< 3 \times 10^{-6}$
μ	-1	105.658369
ν_μ	0	< 0.19
τ	-1	1777
ν_τ	0	< 18.2

Table 1-3. Three lepton generations

Boson	Spin (e)	Mass (GeV/c^2)
γ	1	0
g gluon	1	0
W^\pm	1	80.40
Z^0	1	91.188
graviton	2	?
H (Higgs)	1	?

Table 1-4. Force carriers

CHAPTER 2

EXPERIMENTAL APPARATUS

Fermilab is a world class laboratory in high energy physics, located in Batavia, Illinois. The hadron collider, called the Tevatron, is the world's most powerful accelerator so far. The Tevatron is a superconducting synchrotron that is four miles in circumference. At Tevatron bunches of protons and anti-protons collide at the center-of-mass energy of $\sqrt{s} = 1.96$ TeV.

The Collider Detector at Fermilab (CDF) and D0 are two general purpose detectors built at almost opposite collision points along the Tevatron. The CDF detector itself weighs 5000 tons and is about 12 meters in all three dimensions. In this analysis we use data collected by the CDF collaboration during the period 2002-2009.

In this chapter we give a brief overview of the accelerator chain and the CDF II detector used to collect the data for the measurements.

2.1 Accelerator

Tevatron allows to accelerate particles to the energy of 980 GeV. In order to produce such high energy $p\bar{p}$ collisions a sequence of several individual components is needed: Proton Source (Cockcroft-Walton, Linac and Booster), Main Injector, Antiproton Source (Debuncher, Accumulator and Recycler) and the Tevatron. The schematic picture of the Fermilab accelerator chain is shown in Fig. [2-1](#).

2.1.1 Proton Source

The process leading to the $p\bar{p}$ collisions begins with hydrogen atoms, used to create protons. The atoms are placed in an electric field to strip away electrons and create positively charged ions H^+ . The protons then will congregate on metal surface with cesium. If the proton gets two electrons from the metal, it becomes negatively charged (H^-) and is forced away from the surface. The acquired atoms are then accelerated to 750 keV by a Cockcroft-Walton electrostatic generator.

The next component in the chain is a 150 m linear RF accelerator (the Linac) which boosts their energy to 400 MeV. Before the next stage, the H^- ions are passed through a graphite foil which strips them of their electrons and leaves a pure proton beam.

The protons are injected into the Booster, a synchrotron accelerator about 150 meters in diameter. Dipole magnets steer the beam of protons so that they travel in a circle while quadrupole magnets focus the beam by successively squeezing it along both axes perpendicular to the direction of the beam. Once the bare protons are collected in the Booster, they are accelerated to an energy of 8 GeV by the RF cavities.

2.1.2 Main Injector

The Main Injector is a synchrotron with 3.3 km in circumference. The primary goal of Main Injector is to provide 120 GeV protons for the Antiproton Source and to accelerate protons and antiprotons from 8 to 150 GeV. Since protons and antiprotons have opposite charge, the Main Injector can accelerate both particles moving in opposite directions simultaneously. It also accepts 150 GeV antiprotons from the Tevatron and decelerates them to 8 GeV for transfer to the Recycler.

2.1.3 Antiproton Source

The rate of the antiproton production is the main limitation to the performance of Tevatron. In order to produce anti-protons, 120 GeV protons are transported from the Main Injector to a nickel target. From the interaction sprays of secondary particles are produced, including anti-protons. Those anti-protons are selected and stored into the Debuncher ring where they are stochastically cooled to reduce the momentum spread. At the end of this process, the anti-protons are stored in the Accumulator. As the stack size in the Accumulator ring increases, there comes a point when the stacking rate starts to decrease. By emptying the contents of the Accumulator into the Recycler periodically, the Accumulator is always operating in its optimum antiproton intensity regime.

2.1.4 Tevatron

Tevatron is the final component of the acceleration process, it is currently the highest energy hadron collider in the world. The Tevatron accelerates beams of protons and antiprotons to the energy of 980 GeV, providing a center of mass energy of 1.96 TeV.

The circumference of the Tevatron is 6.28 km. The protons are accelerated by RF cavities in the clockwise direction and antiprotons in the counterclockwise direction. Each of the beams are divided into three “trains”, each containing 12 bunches. The time separation between bunches is 396 ns. Each “train” is followed by a gap called “abort gap”. These gaps are used to remove the beam from the Tevatron without producing any damage. The beam configuration is illustrated in Fig. 2-2. The antiprotons are usually injected after the protons and their bunch ensemble is the mirror image of the proton spacing.

The rate of produced events for a particular process directly depends on instantaneous luminosity (i.e. the intensity of colliding proton and antiproton beams). The instantaneous luminosity is defined:

$$L = \frac{N_B N_p N_{\bar{p}} f}{2\pi(\sigma_p^2 + \sigma_{\bar{p}}^2)}, \quad (2-1)$$

where N_B is the number of bunches; N_p and $N_{\bar{p}}$ are number of protons and antiprotons per bunch, respectively; f is the bunch revolution frequency; and σ_p and $\sigma_{\bar{p}}$ are the average cross-sectional areas of the bunches. Making σ_p , $\sigma_{\bar{p}}$ smaller and N_p , $N_{\bar{p}}$ larger increases the rate of collisions. It is achieved by focusing the beams directly before impact, using the so called low-beta quadrupole magnets. During a store the instantaneous luminosity is decreasing exponentially due to collisions and transverse spreading of the beams which leads to losses of protons and anti-protons. Typical store duration is about 20 hours.

Summary of the current Tevatron performance characteristics is given in Table 2-1. The total integrated luminosity measured at CDF is shown in Fig. 2-3 from the beginning

Table 2-1. Summary of the current Tevatron performance characteristics.

center-of-mass energy	1.96 TeV
bunch crossing separation	396 ns
number of protons per bunch	240×10^9
number of antiprotons per bunch	25×10^9
peak luminosity	$350 \times 10^{30} \text{ cm}^{-2}\text{s}^{-1}$

of Run II. The live luminosity, which excludes integrated luminosity during all the detector dead-times is also shown. The peak instantaneous luminosity recorded is $350 \times 10^{30} \text{ cm}^{-2}\text{s}^{-1}$. The current goal for the Tevatron is to collect 10 fb^{-1} by the end of Run II.

2.2 The CDF II Detector

Data used in the analyses were collected with the CDF Run II detector [22], which is a multi-purpose detector; it is designed to study a wide range of physics processes produced at proton-antiproton interactions and characterized by final states with high transverse momenta particles. The detector is roughly cylindrically and backward-forward symmetric around the beam axis. It is about 10 meters high, extends about 27 meters from end to end, and weights over 5000 tons. The layout of CDF is shown in Fig. 2-4.

CDF has the following coordinate system: the z axis coincides with the direction of the proton beam, the x axis points radially outward the accelerator ring, and the y axis points vertically up. The center of the coordinate system roughly coincides with the center of the beam crossing point.

We can as well the more convenient polar (r, θ, ϕ) coordinate system, where θ is counted from the positive direction of the z axis, ϕ and θ is measured with respect to the positive direction of the x and y axis respectively. Commonly, θ is replaced by the pseudo-rapidity, (η) :

$$\eta = -\ln \tan\left(\frac{\theta}{2}\right). \quad (2-2)$$

The choice of η instead of θ is motivated by the fact that partons have fraction of protons and antiprotons energy, often with imbalanced longitudinal components of the momenta. This leads to large boosts in the observed physics interactions. The quantity called the rapidity:

$$\zeta = \frac{1}{2} \ln \frac{E + p_z}{E - p_z} \quad (2-3)$$

is invariant under Lorentz transformations. In the ultra-relativistic/massless particle limit, the rapidity can be replaced by the pseudo-rapidity.

2.2.1 Tracking and Vertexing Systems

Tracking and vertexing systems at CDF are located within a superconducting solenoid, which is 5 meters in length and 3.2 meters in diameter. It provides a 1.4 T magnetic field directed parallel to the z axis. As charged particles pass through the matter, they cause ionization. The ionization is typically localized near the trajectory of the particle in little clusters called hits. The tracking systems at CDF locate charged particles in space by sampling the deposited electrical charge due to ionization along the particle trajectory. The process is called tracking. Due to the magnetic field, electrically charged particles produced in the collisions follow a helical trajectory. The particle momentum in the $x - y$ plane and its electric charge are determined by observing the radius of curvature of the helix and its orientation relative to the magnetic field.

For many analysis it is critical to determine the point of origin of a particle. It cannot be obtained from a helix alone, all we know is that it is somewhere on the helix. Normally the point of origin is determined by intersecting the helix with at least one other helix corresponding to a particle which we believe has come from the same space point as a result of a decay of common parent particle. This process is called vertexing.

CDF tracking system consists of two major components. These are the Central Outer Tracker (COT) and the silicon detectors: Layer00 (L00), Silicon Vertex Detector (SVX),

and Intermediate Silicon Layers (ISL). Combined, these systems provide coverage up to $|\eta| < 2.0$. The schematic of one quadrant of the CDF tracking system is shown in Fig. 2-5. The components are described in details below.

Central Outer Tracker

The Central Outer Tracker (COT) [23] is an anchor of CDFs tracking system. It is a cylindrical open-cell drift chamber with a large tracking volume, designed to measure the three-dimensional trajectories of charged particles in the central region, $|\eta| < 1.0$. The COT occupies the radial region 40 to 138 cm, and measures 310 cm along the \hat{z} axis. It is filled with fast gas (50% argon, 50% ethane) to make drift times small enough so that the hits can be read out between each Tevatron bunch crossing.

The basic element of the COT is the *cell*, which spans the length of the COT. Within each cell are high-voltage field panels, potential wires and shaper wires which serve to support a regular electrostatic field. Charged particles traveling through the gas mixture leave a trail of ionization electrons. These electrons drift toward the sense wires by virtue of the electric field created by the field panels and potential wires. Because of the magnetic field along the \hat{z} axis, the drift is not in the direction of the electric field. In such crossed fields electrons move in the plane perpendicular to the magnetic field and at an angle α with respect to the electric field. The values of α depends on the magnitude of both fields and the gas properties, in the COT it is $\alpha \sim 35^\circ$. Since the electron drift velocity is known, the position of the track can be accurately measured by simply recording the time of the resulting current on the sense wires. A transverse view of a typical cell with the positions of individual wires is shown in Fig. 2-6.

The cells of the COT are arranged into eight radially spaced superlayers. Four of them have their wires arranged parallel to the \hat{z} axis, allowing track measurements in the $r - \phi$ plane. Other four superlayers have their wires tilted by 2° allowing to record stereo information, track measurements in the $r - z$ plane. The superlayer geometry is shown in

Fig. 2-7. The hit position resolution of COT is approximately $140 \mu m$, which translates into the transverse momentum resolution $\frac{\delta p_T}{p_T} \sim 0.0015 \frac{p_T}{GeV/c}$.

Silicon Detectors

The volume surrounding the beam-pipe is occupied by three silicon detector systems: Layer 00 (L00), Silicon Vertex Detector (SVX) and the Intermediate Silicon Layers (ISL) [23]. The primary purpose of the silicon detectors is to provide excellent spatial resolution for the charged-particle tracks. This is crucial for reconstruction of the displaced secondary vertexes, and, therefore, identification of b jets.

The principle on which the silicon tracking is based is somewhat similar to that of the drift chamber. When a charged particle goes through the silicon, it ionizes the atoms, producing electrons and holes - the remaining silicon atoms missing an electron. In the electric field electrons travel to one side and the holes in the other, leaving an electric signal that can be recorded. Due to the narrow width of the strips, the silicon detectors have much better resolution than COT. To provide excellent spacial resolution silicon detectors have to be positioned as close to the beam as possible, imposing an additional requirement, that the detector should be able to withstand large doses of radiation in the region close to the beam-pipe.

Layer 00 is a single-sided radiation hard silicon microstrip detector. It is mounted directly on the beam pipe, at the inner radius of 1.15 cm and an outer radius of 2.1 cm, so as to be as close as possible to the interaction point. It covers $|\eta| < 4.0$. L00 is designed to enhance the track impact parameter resolution (the impact parameter d_0 is defined as the shortest distance in the $r - \phi$ plane between the interaction point and the trajectory of the particle obtained by the tracking algorithm fit). There are six readout modules with two sensors bonded together in each module.

The Silicon Vertex Detector is composed of five layers of double-sided silicon microstrip detectors, it covers radial coverage from 2.5 to 10.6 cm and $|\eta| < 2.0$. SVX is built in three cylindrical barrels each 29 cm long. One side of each microstrip

detector provides tracking information in the $r - \phi$ plane, the other side provides tracking information in the $r - z$ plane, therefore SVX can reconstruct three-dimensional tracks. Three of the five SVX layers provide 90° stereo information, two SVX layers provide $\pm 1.2^\circ$ small-angle stereo information. The total number of channels in the system is 405,504. The SVX bulkhead design is shown in Fig. 2-8.

The primary goal of the SVX is to detect secondary vertices from heavy flavor decays. The secondary goal is to maximize tracking performance by combining the COT and SVX hit information. The alignment of the SVX detector is very important for the track reconstruction, every effort is made to position the SVX barrels in a coaxial manner. The process of combined COT and SVX track reconstruction [24] starts in COT. After COT-only track is reconstructed, it is extrapolated through the SVX. Because the track parameters are measured with uncertainties, the track is more like a tube of certain radius, determined by the errors on tracks parameters. At each SVX layer, hits that are within a certain radius are appended to the track and the re-fitting is performed to obtain the new set of parameters for the track. In this process there may be several track candidates associated to the original COT-only track. The best one in terms of the number of hits and fit quality is selected at the end.

The impact parameter resolution of the SVX is about $40 \mu\text{m}$. The resolution in z is about $70 \mu\text{m}$.

In the central region, a single ISL layer is placed at a radius of 22 cm. In the plug region, $1.0 < |\eta| < 2.0$, two layers of silicon are placed at radii of 20 cm and 28 cm. ISL improves the tracking coverage in the forward region of the detector. This system is useful for matching tracks within the COT to those within the SVX. Double sided silicon is used in the ISL, the single hit resolution is about $16 \mu\text{m}$ on the axial side and about $16 \mu\text{m}$ on the stereo side.

2.2.2 Calorimetry

The purpose of the calorimeters is to measure the energy of particles producing electromagnetic (photons and electrons) and hadronic (hadrons) showers as they transverse and interact with regions of dense material. CDF uses sampling calorimeters, with dense absorbers interleaved with layers of active scintillator. Wavelength-shifting fibers (WLS) are embedded within the layers of scintillator and transmit the scintillator light via acrylic light guides to photomultiplier tubes (PMTs) located at the tops of the towers. Integrating the charge collected by the PMT gives a measure of the energy deposited in the calorimeter.

The systems cover 2π in azimuth and the pseudorapidity region $|\eta| < 3.6$. The calorimeters are segmented into projectile towers (Fig. 2-9).

The calorimetry detectors at CDF [23] are mechanically subdivided into three regions: central, wall and plug. They are located just outside the solenoid magnet in the central region, and just outside the tracking volume in the plug region. The electromagnetic and hadronic components are called the Central Electro-Magnetic (CEM), Central Hadronic (CHA), Wall Hadronic (WHA), Plug Electromagnetic (PEM) and Plug Hadronic (PHA) calorimeters.

The CEM is divided into 15° wedges in azimuthal angle ϕ and into ten η towers subtending 0.1 units of pseudorapidity. It consists of alternating 1/8 inch absorber layers, made of aluminum-clad lead, and 5 mm layers of polystyrene scintillator, for a total depth of 18 radiation lengths of material. Embedded in the CEM at the approximate depth of maximum shower development are proportional wire chambers, Central Electromagnetic Strip (CES). With the position resolution of 2 mm, they contribute to e^\pm/γ identification, using the position measurement to match with tracks. A second set of proportional chambers, the Central Preshower (CPR), is located between the CEM and the magnet coil, and provide greatly enhanced photon and soft electron identification.

Table 2-2. Summary of quantities characterizing CDF calorimetry.

Name	Coverage	Thickness	Material	Resolution (E in GeV)
CEM	$ \eta < 1.1$	$19X_0$	3 mm Pb, 5 mm Scint.	$13.5\%/\sqrt{E} + 2\%$
PEM	$1.1 < \eta < 3.6$	$21X_0$	4.5 mm Pb, 4 mm Scint.	$16\%/\sqrt{E} + 1\%$
CHA	$ \eta < 0.9$	$4.7\lambda_0$	25 mm Fe, 10 mm Scint.	$75\%/\sqrt{E} + 3\%$
WHA	$0.7 < \eta < 1.3$	$4.5\lambda_0$	50 mm Fe, 10 mm Scint.	$75\%/\sqrt{E} + 3\%$
PHA	$1.2 < \eta < 3.6$	$7\lambda_0$	51 mm Fe, 6 mm Scint.	$80\%/\sqrt{E} + 5\%$

The CHA consist of alternating layers of iron absorber and naphthalene scintillator. They are segmented to match the CEM towers, 0.1 units of pseudorapidity per tower and 15° of azimuth per wedge, with a total thickness of 4.7 nuclear interaction lengths. The WHA is designed to compensate the limited forward coverage of the CHA, and covers the region $0.7 < |\eta| < 1.3$. It is also iron/scintillator based with the thickness of 4.5 nuclear interaction lengths.

The CDF plug calorimeters are similar in concept to the central calorimeters. They also have electromagnetic and hadronic component, as well as preshower and shower maximum detectors. The details of implementation, however, are slightly different. The segmentation is variable: in the lower η (less forward) region the plug calorimeters have 48 wedges, each subtending 7.5° in ϕ ; in the higher η (more forward) region they have 24 wedges, each subtending 15° in ϕ . The segmentation in η also varies from 0.1 to 0.15 units of pseudorapidity. The PEM alternates layers of lead with 4 mm layers of scintillating tiles, for a total of 21 radiation length at normal incidence. The first layer of scintillating tiles act as a preshower detector, Plug Preshower (PPR). At the position of maximum shower development is located a shower position detector (PES) made of scintillating strips. The PHA calorimeter alternates layers of iron with scintillating tile for a total depth of about 7 interaction length.

The measure of calorimeter performance is its resolution. Summary of CDF calorimeter characteristics, including the resolution, is given in Table 2-2.

2.2.3 Other Systems

Muon Detectors

Muons have low bremsstrahlung radiation (due to their relatively large mass), and are not subject to strong interaction with atomic nuclei. Thus, they can penetrate much more material than any other charged particle. In CDF, the muon detectors are placed behind the calorimetry and are generally the outermost detector systems, separated from the rest of the detector by steel shielding.

CDF uses four systems of scintillators and proportional chambers in the detection of muons over the region of $|\eta| < 2$ [23]: Central Muon Detector (CMU), Central Muon Upgrade (CMP), Central Muon Extension (CMX) and Intermediate Muon Detector (IMU). The CDF muon detectors consist of stacked argon-ethane drift tubes, some backed up with scintillator counters. Muons which pass through the drift tubes leave a trail of ionized gas along their trajectory; muons which pass through the scintillation panels induce light pulses which are collected by PMTs.

The CMU detector consists of four layer drift chamber directly behind the hadronic calorimeter. The layers are divided into rectangular drift cells each with a single sense wire. The detector covers $|\eta| < 0.6$ and detects muons with a minimum p_T of 1.4 GeV/c. The CMP sits behind an additional 60 cm layer of steel and is also composed of four layers of individual drift cells covering $|\eta| < 0.6$. The CMP detects muons down to p_T of 2.2 GeV/c. The CMX, composed of conical sections of drift chambers and scintillation counters, extends the muon $|\eta|$ coverage from 0.6 to 1.0, while measuring muons with a minimum p_T of 1.4 GeV/c. Finally, the IMU, which was a part of CDF Run II upgrade, extends muon coverage out to $|\eta| < 1.5$. The IMU is also composed of drift cells and scintillator counters, detects muon with minimum transverse momentum 1.4 – 2.0 GeV/c.

Having a track segment (stub) in the muon chambers is not sufficient for muon detection. Stubs can be due to a hadronic punch-through or just noise in the electronics. Only if a stub matches a certain track measured by the COT then the two are combined to make a muon.

Cherenkov Luminosity Counters

The purpose of the Cherenkov Luminosity Counter (CLC) [25] at CDF in Run II is to measure the luminosity. CLC successfully provides precise measurements at current peak instantaneous luminosities of $\sim 3 \times 10^{32} \text{ cm}^{-2}\text{s}^{-1}$.

The CLC utilizes the effect known as Cherenkov radiation. When a charged particle travels in a medium faster the speed of light in this medium (*i.e.* when $\beta = v/c > 1/n$, where n is the refraction index of the medium), it starts emitting light into a cone around its direction. Cone's opening angle depends on the ratio of the two speeds and the refraction index.

The detector consists of two modules (East and West) located within the “3-degree holes” inside the forward and backward calorimeters, it covers pseudorapidity range $3.75 < |\eta| < 4.75$. Each CLC module consists of 48 long and thin Cherenkov counters, filled with isobutane at pressure 1.5 times larger than atmospheric. The use of isobutane was motivated by its large index of refraction and good transparency for photons. The counters point toward the interaction region as shown schematically in Fig. 2-10. They are arranged around the beam-pipe in three concentric layers, 16 counters in each. This arrangement allows to make the detector much more sensitive to the particles coming directly from the interaction point because they transverse the full length of a counter and generate a large amount of light, which is read out by a photomultiplying tube. Particles coming from secondary interactions with material and from beam-halo interactions pass through the counters at large angles, producing significantly smaller signal than that of primary particles.

The luminosity is measured using the following relation between the instantaneous luminosity L and the number of primary interactions per bunch crossing μ :

$$\mu \cdot f_{BC} = \sigma_{p\bar{p}} \cdot L, \quad (2-4)$$

where $\sigma_{p\bar{p}}$ is the total $p\bar{p}$ cross-section at $\sqrt{s} = 1.96 \text{ TeV}$, and is known relatively well; and f_{BC} is the rate of bunch crossings in the Tevatron.

Therefore, in order to obtain the value of instantaneous luminosity one has to measure μ . At CDF this is done by counting “empty” bunch crossings, *i.e.* bunch crossings with zero primary interactions. The number n of primary interactions per bunch crossing follows Poisson statistics with mean μ :

$$P_n(\mu) = \frac{\mu^n e^{-\mu}}{n!}. \quad (2-5)$$

The probability of having an empty bunch crossing is then:

$$P_0(\mu) = e^{-\mu}. \quad (2-6)$$

Thus, measurement of the probability of having an empty crossing is enough to determine the average number of interactions μ , and, consequently, the value of instantaneous luminosity. This probability is measured by dividing the number of empty crossings (corrected for the detector acceptance) by the total number of bunch crossings in a certain time interval. For a crossing to be considered empty there should be no hits in either East or West CLC modules. The disadvantage of this method is that at very high luminosities the probability of having an empty crossing is small, making it difficult to maintain good precision.

Time-of-Flight

The Time-of-Flight system (TOF) expands CDFs particle identification capability in the low p_T region. TOF measures arrival time t of a particle with respect to the collision time t_0 . The particle mass m is then determined using the relation:

$$m = \frac{p}{c} \sqrt{\frac{(ct)^2}{L^2} - 1}, \quad (2-7)$$

where L is the path length and p is the momentum measured by the tracking system.

TOF has cylindrical geometry with 2π coverage in ϕ and roughly $|\eta| < 1$ in pseudorapidity. It consists of 216 scintillator bars installed at a radius of about 138 cm in the 4.7 cm space between the outer shell of the COT and the cryostat of the

superconducting solenoid. The complete description of the TOF detector can be found in [26].

2.2.4 Trigger System and Data Acquisition

Bunch crossings at the Tevatron occur every 396 ns, a rate of 2.5 MHz. Since data can be written to tape at a rate of ~ 75 Hz, there needs to be a system that allows to select quickly the most interesting events. CDF uses a three level trigger system, the data flow through it is schematically shown in Fig. 2-11. The elaborate description of the entire system is given in [23].

The Level-1 (L1) is a synchronous system with an event read in and an accept or reject decision made every bunch crossing. Within the DAQ electronics of each detector component, there is a 42 “bucket” data pipeline. The pipeline is synchronized with the Tevatron master clock, which has a period of 132 ns. Event data from each proton-antiproton bunch crossing enters the pipeline. A decision must be made before the data reaches the end of the pipeline, otherwise the data is lost. The decision time for L1 is $5.5 \mu\text{s}$ and it is based on the data from the calorimeters, the COT and the muon chambers. The calorimeter stream decision is based upon the energy deposited in calorimeter towers, along with the magnitude of unbalanced transverse energy. The Extremely Fast Tracker (XFT) [27] uses information from the COT to reconstruct tracks, events are accepted or rejected based on the track multiplicity and transverse momenta. The muon stream uses information from the XFT to match tracks to hits in the muon chambers to produce muon candidates. The maximum accept rate for L1 trigger is 20 kHz, a factor of few hundred smaller than the input rate of 2.5 MHz.

Events which meet the requirements of the L1 trigger are passed to the Level-2 (L2). At L2, an event is written into one of four buffers within the DAQ electronics for each detector component. These buffers are different from the data pipeline used in L1, the data here remains in the buffer until the decision is made. While event data are being processed, they cannot be overwritten by another event from L1. If an L1 accept occurs

while all four L2 buffers are occupied, the deadtime is incurred. In order to minimize deadtime, the latency of the L2 decision must be less than approximately 80% of the average time between L1 accepts. Therefore, the L2 latency is designed to be 20 μ s. To make a decision, L2 uses information from L1 as well as additional data from the shower maximum strip chambers (CES) in the central calorimeter and the $r - \phi$ strips of SVX. L2 extends XFT tracks inside the SVX volume and adds the measurement of the track impact parameter d_0 . Significant impact parameter indicates a displaced vertex, which is an extremely powerful signature. The maximum accept rate for the L2 trigger is 300 Hz.

The Level-3 (L3) trigger uses the entire detector data and consists of two components: the Event Builder and the processing farm. The read out event fragments are put in the proper order by the custom hardware system, called the Event Builder. Then, the arranged event fragments are channeled to a farm of conventional PCs running Linux. The farm consists of multiple sub-farms, each having one head node and 12-16 processor nodes. The head nodes receive ordered sequence of event fragments from the Event Builder and assemble those fragments into a block of data, called the event record. This event record is suitable for analysis by CDF software and from then becomes one and the only piece of information about a particular event. The L3 takes advantage of full detector information, a decision is made based upon detailed particle identification and event topology. The accept rate for the L3 trigger is approximately 75 Hz.

2.2.5 Good Run Requirements

The data passing the L3 trigger is being segmented into ten streams and written to tape in real time. However, not all of it is suitable for physics analysis. For this reason, good run requirements are established to determine which data runs should be used by physics groups and which are not. A run is defined as a continuous period of data taking without resetting the DAQ system. For a run to be marked “good”, all detector components and their readout should operate properly during the run. If one (or more) of detector components is experiencing problems, a “bad” flag is set. The run can still be

used in physics analysis, but only if the analysis does not need data from the problematic component. It is up to the CDF shift crew to decide which flag should be set to a run.

2.3 Jet Reconstruction

In theory, a “jet” is a collection of soft partons originating in a process of soft gluon showering by a primary parton. Quarks and gluons produced in high-energy collisions do not interact directly with the detector. Instead, they hadronize, forming a collimated groups of hadrons, often referred as “jets”, which pass through the detector. The definition of jet is rather vague, as one can come up with many different ways of grouping particles.

Jet clustering algorithms are designed to cluster the complex structure of final state objects from each collision into jets. These jets reflect physical properties of the partons from hard scattering. Currently at CDF there are three jet clustering algorithms in use: JetClu [28], a cone algorithm combining objects based on relative separation in $\eta - \phi$ space; MidPoint, an algorithm similar to JetClu but having some modifications; and K_T [29], an algorithm combining objects based on their relative transverse momentum as well as their relative separation in $\eta - \phi$ space.

The JetClu algorithm was used in the measurements presented in this dissertation.

2.3.1 Jet Clustering

Jets are reconstructed based on the calorimeter information using a JetClu cone algorithm. The algorithm starts with the highest E_T tower and forms preclusters from an unbroken chain of continuous seed towers with transverse energy above 1 GeV within a window of 7×7 towers centered at the originating seed tower. If a seed tower is outside this window, it is used to form a new precluster. The coordinates of each precluster are the E_T -weighted sums of ϕ and η of the seed towers within this precluster:

$$E_T^{cluster} = \sum_{i=0}^{N_{towers}} E_{T_i}, \quad (2-8)$$

$$\phi^{cluster} = \sum_{i=0}^{N_{towers}} \frac{E_{T_i} \phi_i}{E_T^{cluster}}, \quad (2-9)$$

$$\eta^{cluster} = \sum_{i=0}^{N_{towers}} \frac{E_{T_i} \eta_i}{E_T^{cluster}}. \quad (2-10)$$

The tower centroid (η_i, ϕ_i) is obtained by:

$$\eta^i = \frac{E_{T_i}^{EM} \eta_i^{EM} + E_{T_i}^{HA} \eta_i^{HA}}{E_{T_i}}, \quad (2-11)$$

$$\phi^i = \frac{E_{T_i}^{EM} \phi_i^{EM} + E_{T_i}^{HA} \phi_i^{HA}}{E_{T_i}}, \quad (2-12)$$

where $E_{T_i}^{EM}$ and $E_{T_i}^{HA}$ are transverse energies deposited in the electromagnetic (EM) and hadronic (HA) parts of the i -th calorimeter tower, respectively.

In the next step, all towers with $E_T > 0.1$ GeV within $R = \sqrt{(\Delta\phi)^2 + (\Delta\eta)^2} = 1.0$ of the precluster are merged into a cluster, and its (η, ϕ) -coordinates are recalculated. This procedure of calculating cluster coordinates is iterated until a stable set of clusters is obtained. A cluster is stable when the tower list is unchanged from one iteration to the next. If the clusters have some finite overlap, then an overlap fraction is computed as the sum of the E_T of the common towers divided by the E_T of the smaller cluster. If the fraction is above a cutoff (0.75), then the two clusters are combined. If the fraction is less than the cutoff, the clusters are kept intact. The raw energy of a jet is the sum of the energies of the towers belonging to the corresponding cluster. The momentum of a jet is a scalar sum:

$$p_x = \sum_{i=0}^{N_{towers}} E_i \sin(\theta_i) \cos(\phi_i), \quad (2-13)$$

$$p_y = \sum_{i=0}^{N_{towers}} E_i \sin(\theta_i) \sin(\phi_i), \quad (2-14)$$

$$p_z = \sum_{i=0}^{N_{towers}} E_i \cos(\theta_i), \quad (2-15)$$

where (θ_i, ϕ_i) is the angular position of the i -th calorimeter tower.

2.3.2 Jet Corrections

Corrections are applied to the raw energy to compensate for the non-linearity and non-uniformity of the energy response of the calorimeter, the energy deposited inside the jet cone from sources other than the leading parton, and the leading parton energy deposited outside the jet cone. Here we give a brief review of the applied corrections. A detailed description of this procedure can be found in [30].

The first step is to correct for the η -dependence of the calorimeter response. This correction is especially important in the regions with significant non-uniformities and uninstrumented regions, such as between two halves of the central calorimeter, or between central, wall and plug calorimeters. The correction is based on a good understanding of the central region of the calorimeter. The idea is that in an event with only two jets, their transverse energies should be balanced. The p_T of a “probe” jet, anywhere in the calorimeter is compared to the p_T of a “trigger” jet in the central region, away from uninstrumented regions, $0.2 < |\eta| < 0.6$. The results are shown in Fig. 2-12. The final corrections are derived as continuous functions of p_T and binned functions of η .

The next step is designed to correct for multiple $p\bar{p}$ interactions in the same bunch crossing. This is done by measuring the amount of energy deposited in a randomly chosen cone of radius $R = 1.0$ in minimum bias events, triggered by requiring hits in the CLC counters on either side of the detector. The correction is parametrized as a function of the number of primary vertexes in an event.

The so called “absolute” correction accounts for the non-linear response of the calorimeter. The CDF calorimeters respond differently to particles of various energies. An average correction is determined from dijet Monte Carlo. This correction relies on the

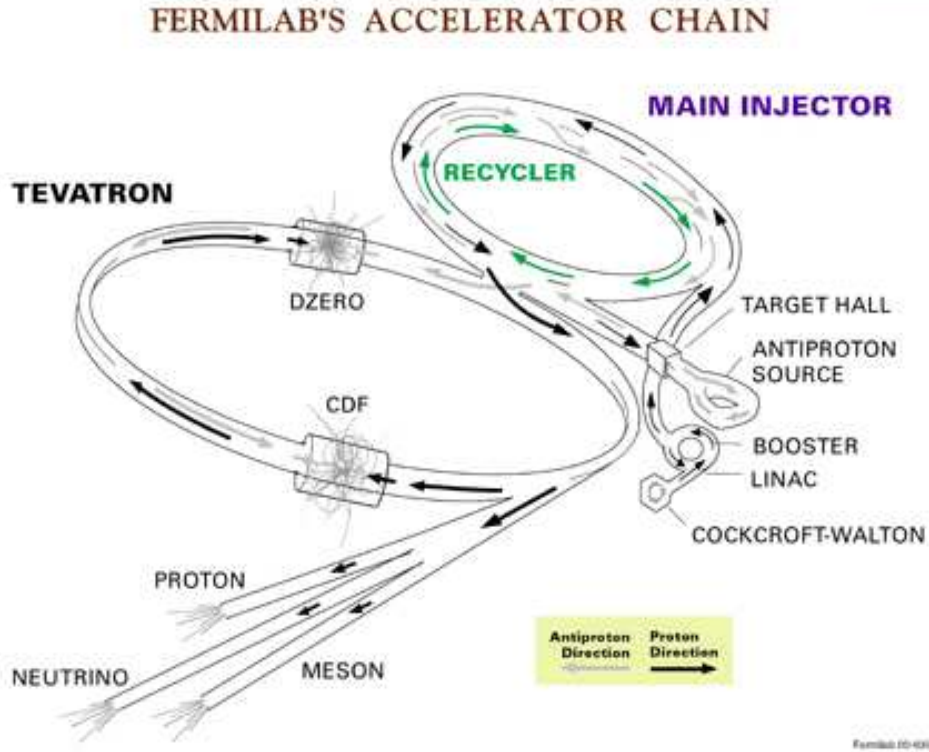


Figure 2-1. Overview of the Fermilab accelerator complex. The chain consists of several individual components: Proton Source (Cockcroft-Walton, Linac and Booster), Main Injector, Antiproton Source (Debuncher, Accumulator and Recycler) and the Tevatron. The detectors, CDF and D0, are also shown.

careful tuning of the detector simulation, based on “in situ” calibrations using data tracks at low energies and test beam data at high energies. The correction is a function of p_T .

Finally, the so called “out-of-cone” correction account for the particle-level energy leakage of radiation outside the clustering cone. It corrects the jet energy back to the parent parton energy. The correction is based on the ratios of jet and parent parton energies obtained from the Monte Carlo.

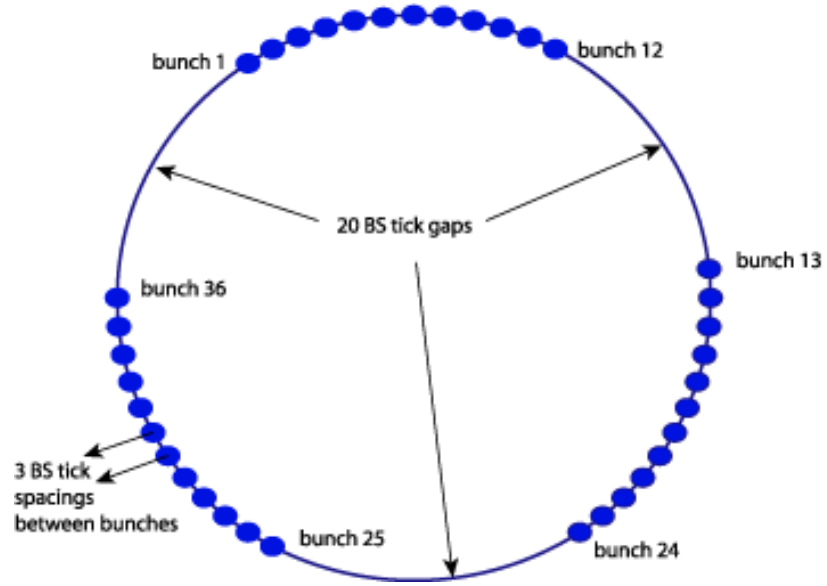


Figure 2-2. Beam structure at the Tevatron.

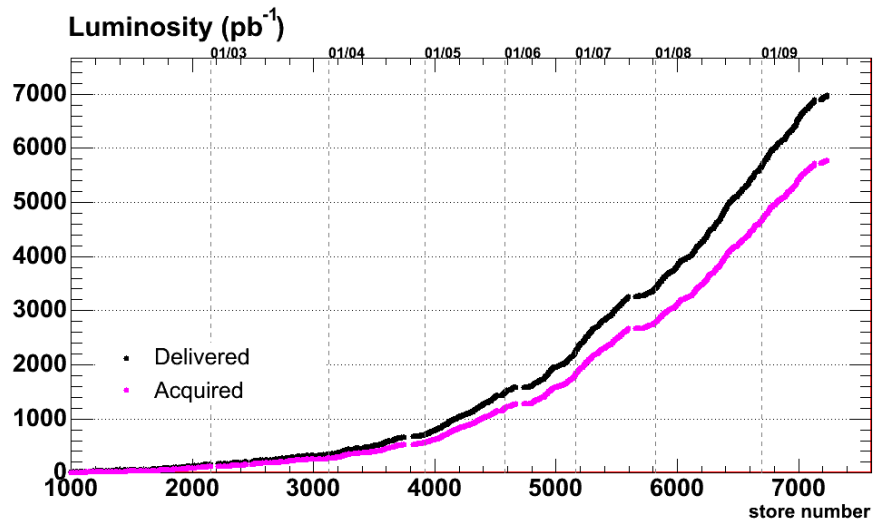


Figure 2-3. The total integrated luminosity delivered by the Tevatron from the beginning of Run II which started in April 2001.

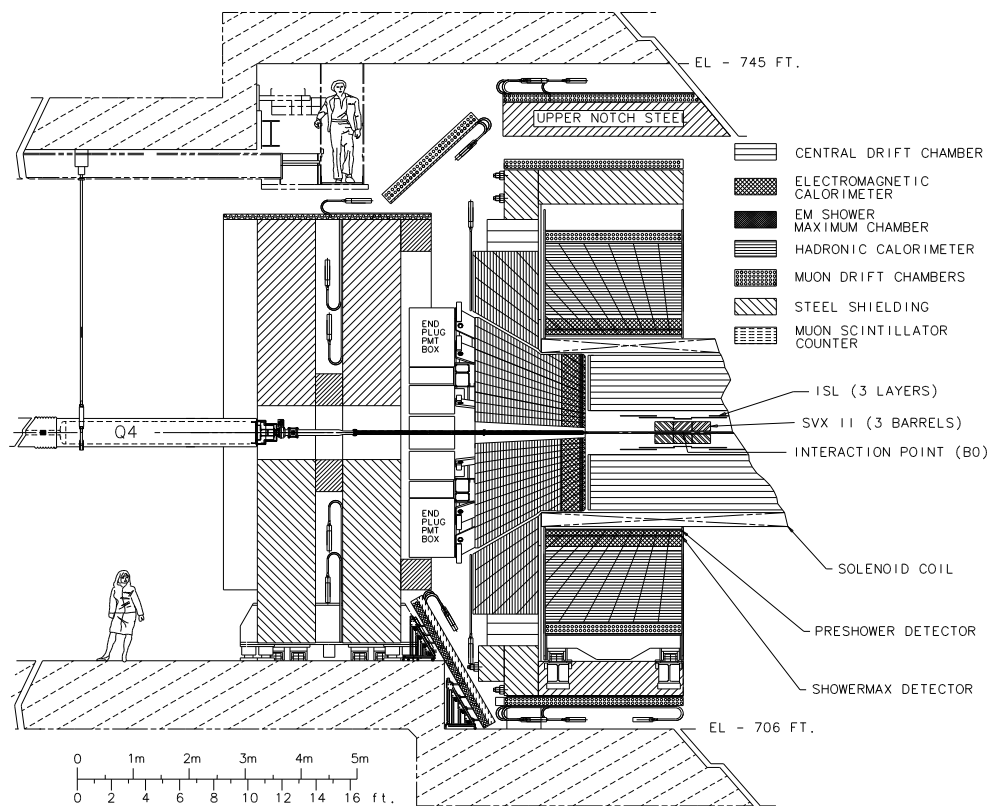


Figure 2-4. The schematic cross-section view of the CDF detector.

CDF Tracking Volume

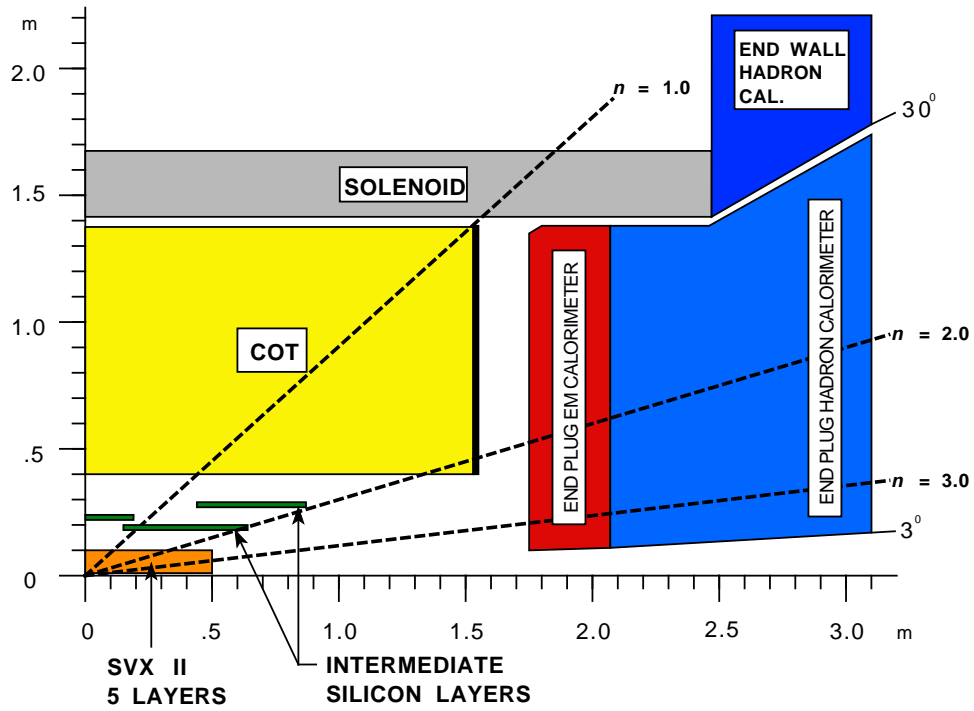


Figure 2-5. The schematic r - z view of one quadrant of the CDF tracking system. Its components: Central Outer Tracker (COT) and the silicon detectors: Layer00 (L00), Silicon Vertex Detector (SVX), and Intermediate Silicon Layers (ISL) are shown.

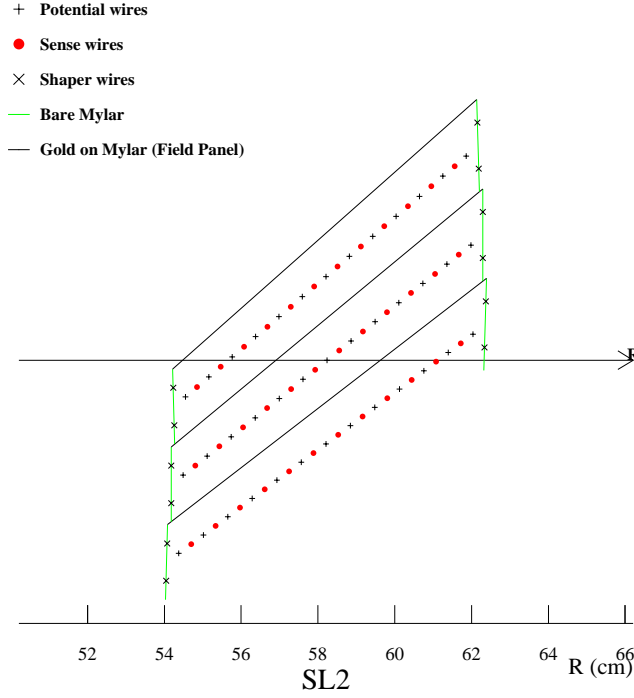


Figure 2-6. Transverse view of the nominal cell layout for COT superlayer 2. The arrow shows the radial direction. The electric field is roughly perpendicular to the field panels. The magnetic field is perpendicular to the plane. The angle between wire-plane of the central cell and the radial direction is 35° .

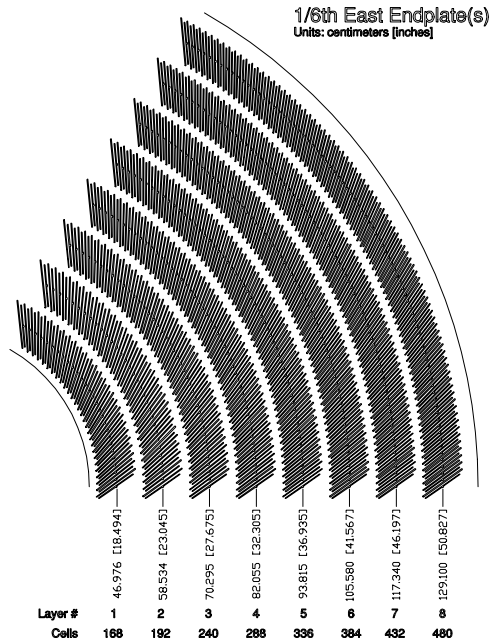


Figure 2-7. 1/6th of the COT east end plate. Shown are the wire-plane slots grouped into eight superlayers.

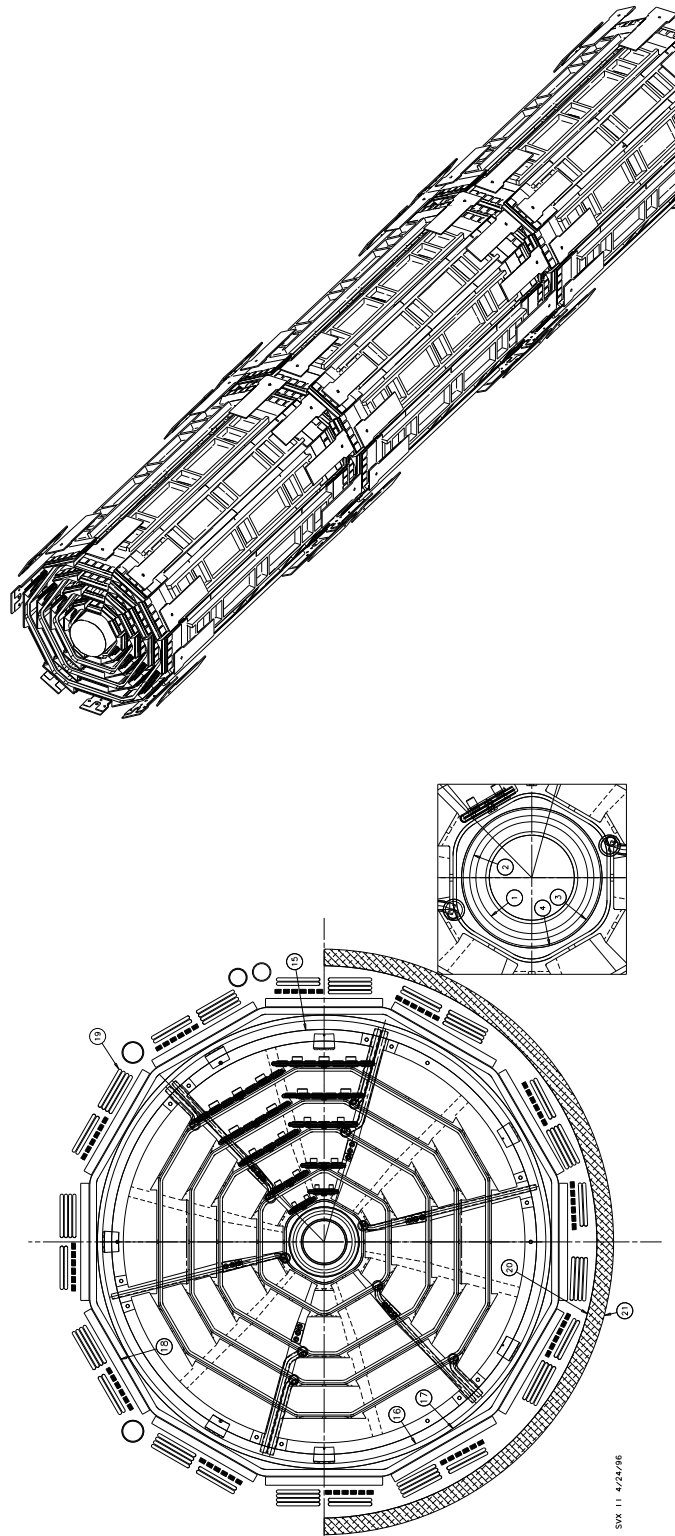


Figure 2-8. SVX bulkhead design. Placement of ladders is shown in two adjacent wedges.

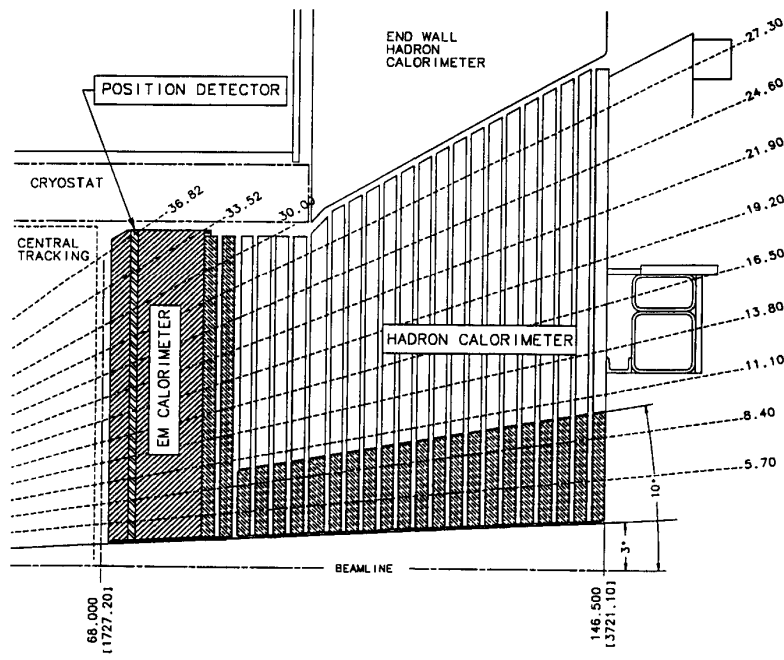


Figure 2-9. Schematic picture of one quadrant of the plug calorimeter including the electromagnetic and hadronic parts. The plug calorimeter has full 2π coverage and extends to $1.1 < |\eta| < 3.6$.

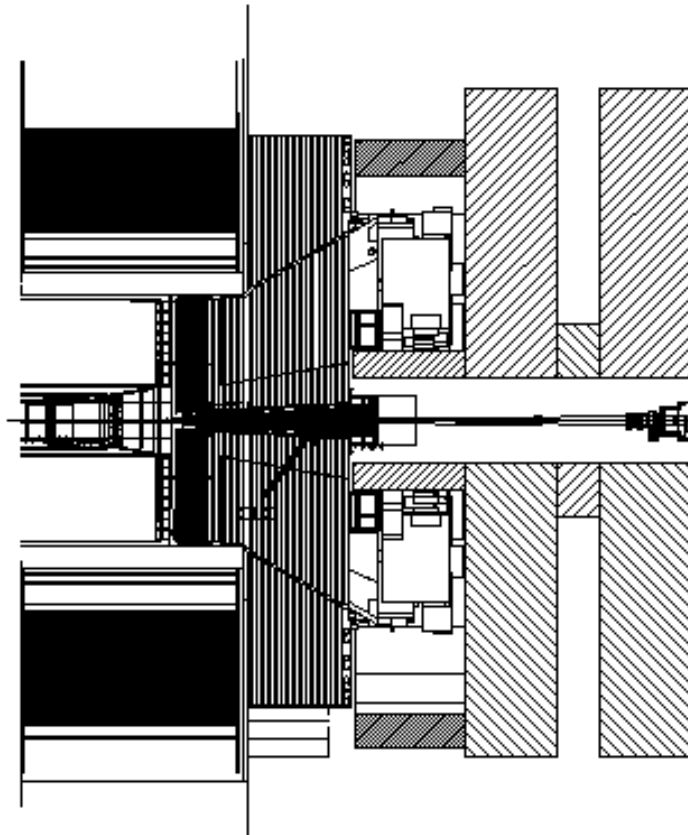


Figure 2-10. The Cherenkov Luminosity Counter at CDF. The detector modules are located within the “3-degree holes” inside the forward and backward calorimeters.

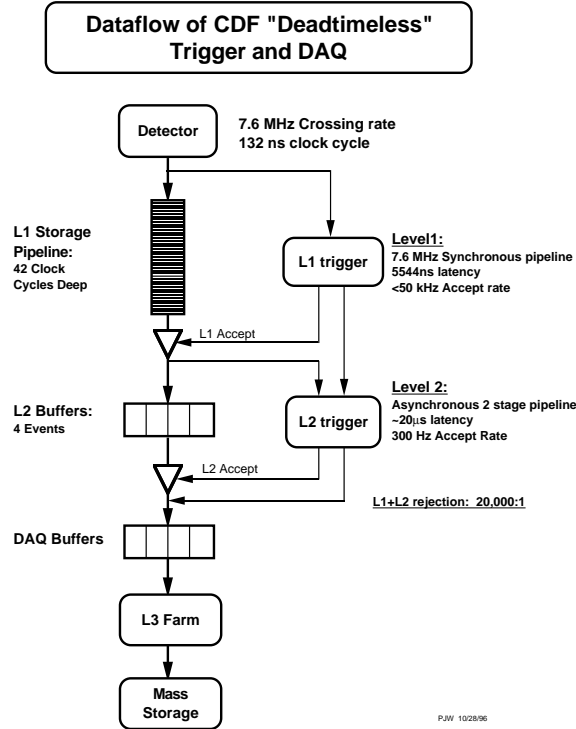


Figure 2-11. Functional block diagram of the CDF data flow. The crossing rate at the Tevatron is actually only 2.5 MHz, but the trigger system was designed for the originally envisioned 7.5 MHz crossing.

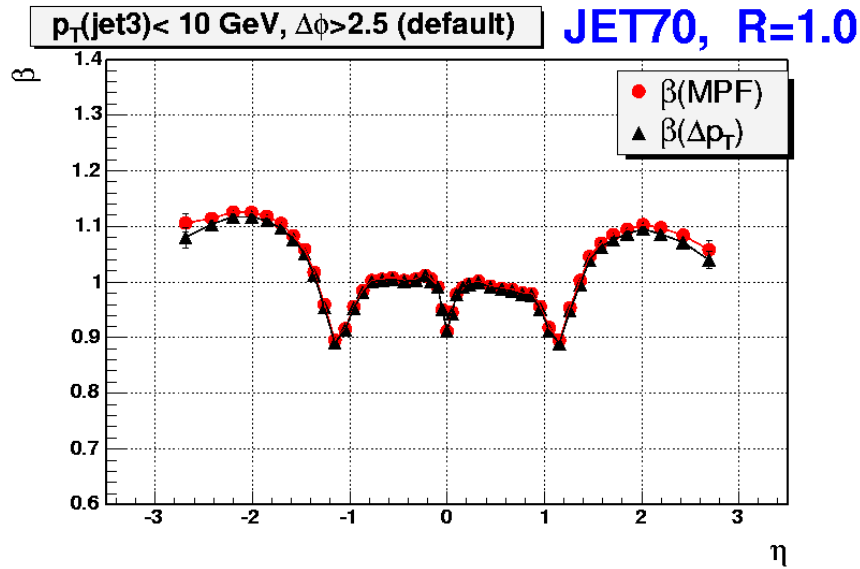


Figure 2-12. The ratio $\beta = p_T^{probe} / p_T^{trigger}$ of transverse momenta of the “probe” and the “trigger” jets using the 70 GeV jet trigger, obtained using two different methods (missing E_T projection fraction and dijet balancing. The “probe” trigger jet has to be in a central region $0.2 < |\eta| < 0.6$, while the probe jet may be anywhere in the calorimeter.

CHAPTER 3 DATA SAMPLE AND EVENT SELECTION

3.1 Data and Monte Carlo Samples

Once $t\bar{t}$ pair is produced, it has no time to form a hadron and top quarks instantly(10^{-25} s) decay almost 100% of the time into $t \rightarrow W^+b$. W boson has option to decay leptonically or hadronically:

$$W \rightarrow l\nu, W \rightarrow q\bar{q}' \quad (3-1)$$

Depending on the decay modes of W boson, $t\bar{t}$ decay falls into three categories:

Category	Decay products	Branching ratio	Signature
Dilepton	$bbl^-l'^+\bar{\nu}\nu'$	5%	2 or more jets, opposite side leptons and missing \cancel{E}_T
Lepton+Jets	$bbq\bar{q}'l\nu$	29%	4 or more jets, 1 lepton and missing \cancel{E}_T
All Hadronic	$bb4q$	46%	6 or more jets

Table 3-1. $t\bar{t}$ decay channels. l corresponds to electron or muon only

Lepton+Jets is considered to be the “golden channel” to perform a measurement in Top Physics. It has a very distinguished signature and fairly large sample. Therefore, all the previous searches for $t\bar{t}$ resonances were performed in lepton+jets channel. Comparing to all hadronic channel, the biggest disadvantage is overwhelming background, which comes dominantly from QCD multi-jet production. For this reason a powerful event selection must be applied, which is described below.

The data events for this analysis are CDF Run II multi-jet events collected in 2002-2008 years(up to period 17). During this time, CDF accumulated $\approx 2.8 fb^{-1}$. In our search we use *TOP_MULTIJET* trigger, which selects the events of our interest during data-taking. It has cross-section of 14nb and $\approx 85\%$ efficiency on SM $t\bar{t}$ all hadronic events.

To describe SM $t\bar{t}$ and resonant $t\bar{t}$ production we use standard CDF Monte Carlo samples. All samples were generated using Pythia event generator, assuming top mass of 175 GeV and $M_{X_0} = \{450, 500, 550, 650, 700, 750, 800, 850, 900\} GeV/c^2$. On the final

step, official CDF simulation and production packages were used to properly reproduce the detector environment.

3.2 Event Selection

To optimize the event selection for M_{X_0} events, we take into account the fact of the $t\bar{t}$ presence in M_{X_0} events and therefore we expect them to have similar topology to the one in SM $t\bar{t}$. So, for the purpose of the event selection we treat SM $t\bar{t}$ sample as our signal. As you will see below, this event selection gives us comparable acceptances for M_{X_0} and SM $t\bar{t}$ events. Obviously, it is not the most optimal. Each event in this analysis must pass three sets of cuts: trigger cuts, clean up cuts and finally Neural Net cut.

TOP_MULTIJET trigger requires:

- Level1: at least one tower with $E_T \geq 10\text{GeV}$
- Level2: at least 4 clusters with $E_T \geq 15\text{GeV}$ and $\sum E_T \geq 175\text{GeV}$
- Level3: at least 4 jets with $E_T \geq 10\text{GeV}$

Further clean up cuts require:

- good run list
- vertex position: $|z| < 60\text{cm}$ and $|z - z_p| < 5\text{cm}$
- \cancel{E}_T significance($\cancel{E}_T/\sqrt{\sum E_T}$): < 3
- tight lepton veto
- 6,7 jets with $|\eta| < 2$ and $E_T > 15\text{GeV}$ after level 5 corrections

After clean-up cuts requirement we have: about 20% efficiency on the SM $t\bar{t}$ events, only 7% of the data events survive after the requirement on 6,7 tight jets, SM $t\bar{t}$ contribution in the data sample is expected to be less than 0.3%. Having the fact that $t\bar{t}$ presense in the data is negligible, it is safe to consider, for the purpose of the event selection, the whole data sample as QCD background and treat SM $t\bar{t}$ sample as our signal.

On the next step we define the set of variables, which distinguish between QCD and SM $t\bar{t}$ events topology. Due to the presence of top quarks in the event, all hadronic SM $t\bar{t}$

production has the main feature of high jet multiplicity with jets E_T around 50GeV (even higher for M_{X_0} events), therefore we expect higher energetic events than for QCD. The fact that top quarks are produced almost at rest leads to another feature of events being central. In addition, we exploit the fact that events contain W bosons and top quarks, by using dijet and trijet invariant masses. Below you can find the list of the variables:

- total transverse energy, $\sum E_T$
- sub-leading transverse energy, $\sum_3 E_T$
- centrality, C
- aplanarity, A
- the minimum dijet mass, M_{2j}^{min}
- the maximum dijet mass, M_{2j}^{max}
- the minimum trijet mass, M_{3j}^{min}
- the maximum trijet mass, M_{3j}^{max}
- $E_T^{1*} = E_T^1 \cdot \sin^2 \theta_1^*$
- $\langle E_T^* \rangle_{3N} = (E_T^{3*} \cdot E_T^{4*} \cdot \dots \cdot E_T^{N*})^{1/(N-2)}$
- FlameNN

ΣE_T is the sum of the transverse energies of all jets in the event. $\Sigma_3 E_T$ is total transverse energy minus the transverse energies of two most energetic jets. *Centrality* is $\frac{\Sigma E_T}{\sqrt{\hat{\sigma}}}$ with $\sqrt{\hat{\sigma}}$ being the invariant mass of all jets. *Aplanarity* is defined as 3/2 of the smallest eigenvalue of the sphericity matrix \hat{S}^{ij} . The sphericity matrix \hat{S}^{ij} is defined in equation 5-2. Minimum and maximum invariant masses are calculated from all possible jets combinations. θ^* is the angle between the jet and the proton beam axis in center of mass frame of all jets.

$$S^{ij} = \frac{\sum_{p=1}^6 (P_p^i \times P_p^j)}{\sum_{p=1}^6 (P_p^2)}, \quad \text{where } i, j = x, y, z \quad (3-2)$$

For the last variable, FlameNN, we exploit the full information from the event about its production and decay through SM $t\bar{t}$ Matrix Element. We calculate ‘minus log

probability' for each event to be the result of SM $t\bar{t}$ decay. We do that at 9 different top mass points, so in the end we have the following quantity:

$$FlameNN = \sum_{k=-4GeV}^{4GeV} -Log(P(m_{top} = 175 + 5k)) \quad (3-3)$$

Fig. 3-2, 3-3 show the comparison of 11 variables used as an input to Neural Net: background dominated data events, SM $t\bar{t}$ and M_{X_0} at 500, 700, 900 GeV. They correspond to the events passed trigger and clean up cuts. As you can see from the plots, there is a quite good separation between QCD dominated data and $t\bar{t}$ events. So in the end, we have all $t\bar{t}$ samples peaked at Neural Net output value equal to 1, and QCD events peaked at 0. The main idea behind Neural Net is described below.

In tables table 3-2 we show number of data events we have after various cuts in our analysis. Table 3-3 shows the same numbers for SM $t\bar{t}$ sample. Additionally, we calculate SM $t\bar{t}$ /QCD, using the following expression: $N_{SM}^{exp} = \epsilon L \sigma$, where ϵ - acceptance, L - total integrated luminosity($2800pb^{-1}$), σ - SM $t\bar{t}$ theoretical cross-section($6.7fb^{-1}$). The number of QCD events is the difference between the observed number of events in the data shown 3-2 in table and the signal expectation. The SVX b-tagger used has a higher efficiency in the Monte Carlo than in the data. Therefore we need to degrade the number of tagged events according to the appropriate scale factor which is $SF = 0.95$.

Table 3-2. Number of events in the multi-jet data after the clean-up cuts and tagging. The integrated luminosity is $L = 2.8fb^{-1}$.

Cut	Events	Fraction (%)
Initial	24283816	100
Trigger and Clean up cuts	11719533	48.2
$N_{tight jets} = 6, 7$	1160091	4.8
1 tag	147076	0.60
2 tag	14656	0.06
1,2 tags and NNet cut	3158	1.3e-02

Table 3-3. Number of events in the SM $t\bar{t}$ Monte Carlo sample.

Cut	Events	Fraction (%)	Expected	S/B
Initial	4719385	100	17000	1e-03
Trigger and Clean up cuts	1876874	39.7	7000	1e-03
$N_{tight\ jets} = 6, 7$	939741	19.9	3700	1/320
1 tag	416786	8.8	1570	1/90
2 tag	173876	3.9	690	1/20
1,2 tags and NNet cut	179781	3.8	680	1/3

Table 3-4. Number of events in the M_{X_0} Monte Carlo samples.

$M_{X_0}[GeV]$	500		700		900	
Cut	Events	(%)	Events	(%)	Events	(%)
Initial	531758	100	531968	100	531922	100
Trigger and Clean up cuts	225208	42.3	189600	35.6	150267	28.2
$N_{tight\ jets} = 6, 7$	117561	22.1	102192	19.2	78066	14.7
1 tag	51783	9.7	44172	8.3	32628	6.1
2 tag	21318	4.0	16326	3.1	10583	2.0
1,2 tags and NNet cut	24931	4.7	29441	5.5	18839	3.5

3.2.1 Neural Net

The neural network, Multilayer perceptron (MLP [66]), we consider in our analysis is implemented in ROOT [67] through the class *TMultiLayerPerceptron*. This is a simple feed-forward network with an input layer, several hidden layers and an output node. The best configuration we found consists of 2 hidden layers with 20 and 10 hidden nodes respectively and a single output node. The output node, NN_{out} , is the variable used to place the final cut on and it ranges from 0 to 1: 0 - background, 1 - signal. Fig. 3-4 shows the configuration we use. The next step is to train neural net to distinguish between signal and background. The aim of the training process is to minimize the total error on a set of weighted examples. The error is defined as the sum in quadrature, divided by two, of the error on each individual output neurons (one in our case). The *TMultiLayerPerceptron* C++ class implements a variety of learning methods, but we consider here only Broyden, Fletcher, Goldfarb, Shanno (BFGS) method which implies the computation of a $N_{weights} \times N_{weights}$ matrix and is considered to be more powerful.

In BFGS method, weights are set to the minimum along the line dened by the conjugate gradient. Parameters are τ and *Reset*, which defines the epochs where the direction is reset to the steepest descent. The values we will be using are the default ones, $\tau = 3$ and *Reset* = 50. We do the training on same number of background and signal events of 940 thousand. We divide each sample on testing and learning samples. After each epoch, training and testing errors are calculated. If we have too few training iterations(epochs), the network will be unable to extract important general features from the training set; too many, and the net will begin to learn the details of the training sample to the detriment of its ability to abstract general features - a process known as over-training. As the result of over-training, training error becomes smaller than testing one. Fig. 3-5 shows that both errors are almost indistinguishable. From the same picture you can see that learning of the neural network is the fast process; in less than about 20 epochs the errors are stable. The output of the neural network, NN_{out} , after the training is shown in Fig. 3-6 as evaluated on the test sample. The training took about 1000 cpu minutes on a standard PC. The outcome of the neural network training is exported as a standalone C++ class, containing all the weights for the network. When we apply back the neural network to the whole sample of 507 thousand multi-jet events and to the $t\bar{t}$ events normalized to the expectation at this level, i.e. $\simeq 2260$ events, we obtain the distributions of 3-7. The optimization of the cut will be based on the maximization of the signal statistical significance, $\frac{S}{\sqrt{B+S}}$. As shown in Fig. 3-7 such a maximum is reached at $\simeq 0.93$. As you can see from the same plot, by introducing FlameNN variable into neural net we gain a factor of $\simeq 2$ in S/B value for the same signal efficiency. In the table 3-5 we show list of acceptances for M_{X0} samples. As you can see from the table, even though we trained neural net on SM $t\bar{t}$ events as signal, for the same neural net cut acceptances values for M_{X0} and SM $t\bar{t}$ are comparable.

3.2.2 QCD Background Modeling

The method used for the background estimate in the all-hadronic channel is based on the parametrization of the jet tagging probability, P , as a function of the jet- E_T , the number of SVX tracks within the jet, N_{trk} , and the number of vertexes, N_{vert} . We define the parametrization in the matrix form, *Tag Rate Matrix*, which provides the probability for a jet to be tagged once we provide jet E_T , N_{trk} , N_{vert} . Once we have the probability for each jet, we can define the probability per event. Equations (3-4) and (3-5) define the probability for each event to be single or double tagged respectively. It's worth mentioning that double tag probability equation (3-5) works up to a constant, due to the fact that most of b-jets are produced in pairs. We obtain the constant normalization factor from QCD dominated region.

$$P_i^+ \prod_{j \neq i} (1 - P_j^+) \quad (3-4)$$

$$P_i^+ P_j^+ \prod_{k \neq i, j} (1 - P_k^+) \quad (3-5)$$

To derive tag rate matrix we use QCD enriched region with 4 and 5 jets. Next step is to extrapolate the to the events with 6 and 7 jets. we define a probability for each event to have 1 or 2 tags. This probability is used as a weight on pre-tagged data events to predict

Table 3-5. Table of acceptances for M_{X_0} Monte Carlo samples.

Mass	acceptance
450	0.042
500	0.047
550	0.053
600	0.057
650	0.058
700	0.056
750	0.052
800	0.046
850	0.040
900	0.036

QCD shape for 1 and 2 tags of any variable, including M_{X0} . Fig. 3-8 - 3-13 show tag rate matrix prediction for the variables in several control regions, using events with 6 or 7 events after clean up cuts.

Obviously, when we use pre-tagged data to predict M_{X0} spectrum for QCD we may have contamination in that sample coming from M_{X0} as well as SM $t\bar{t}$ events. We account for this effect below.

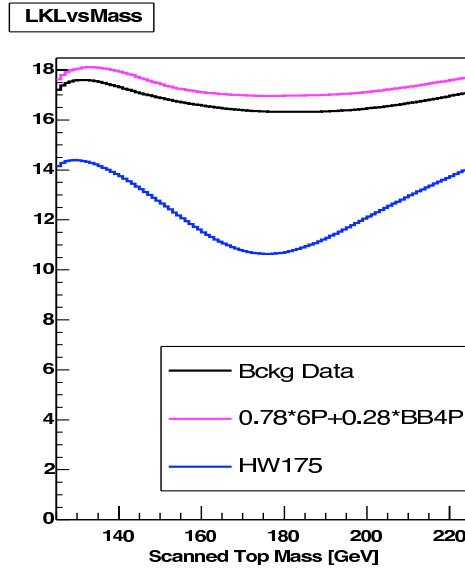


Figure 3-1. Negative log probability vs m_{top} . Blue line corresponds to $t\bar{t}$ sample of $m_{top} = 175$ GeV, while red and black lines are the backgrounds modeled by MC and data respectively

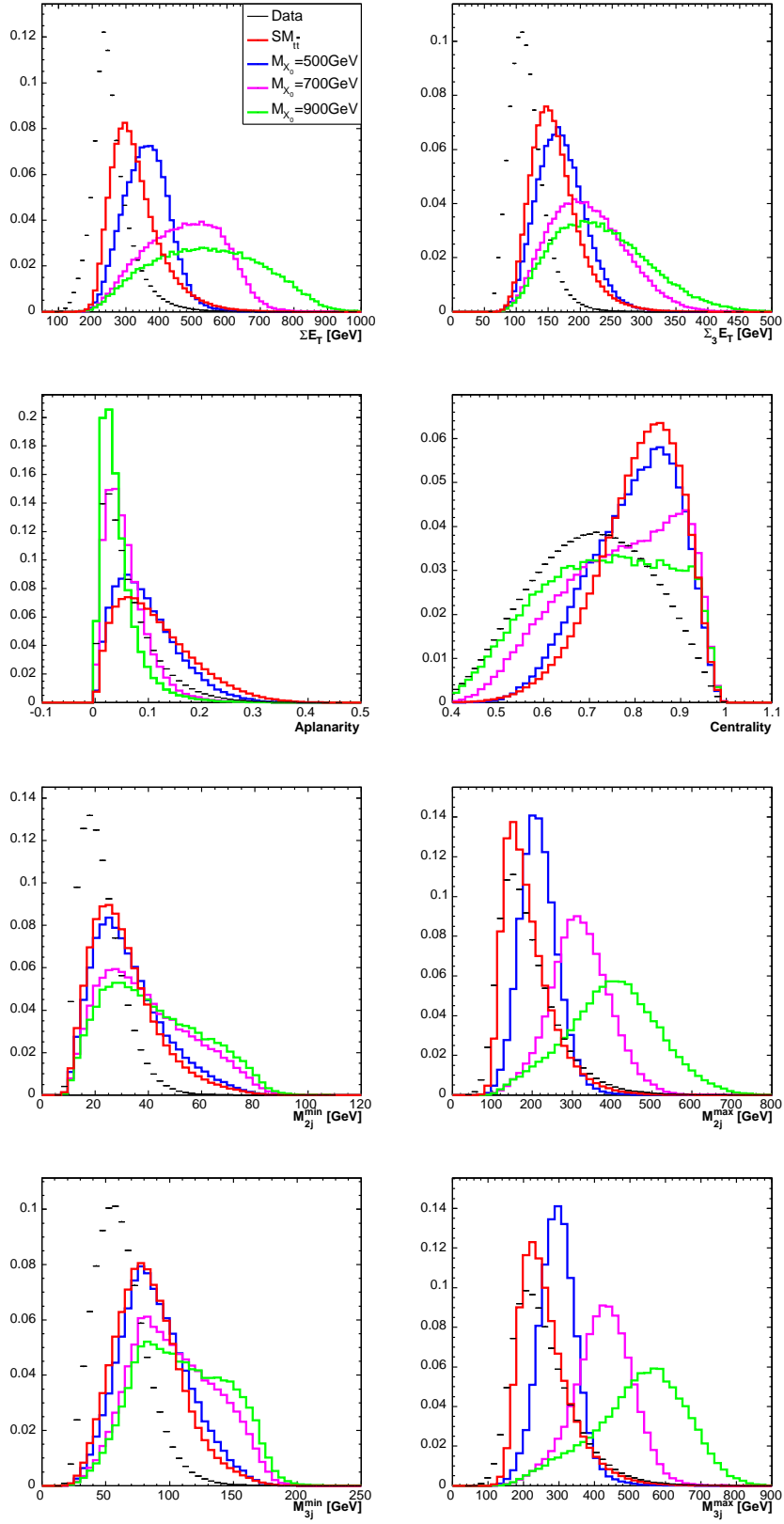


Figure 3-2. Neural net input variables: QCD dominated data - black, SM $t\bar{t}$ - red, 500, 700 and 900 GeV $t\bar{t}$ resonances - blue, magenta and green respectively. All histograms are normalized to unity

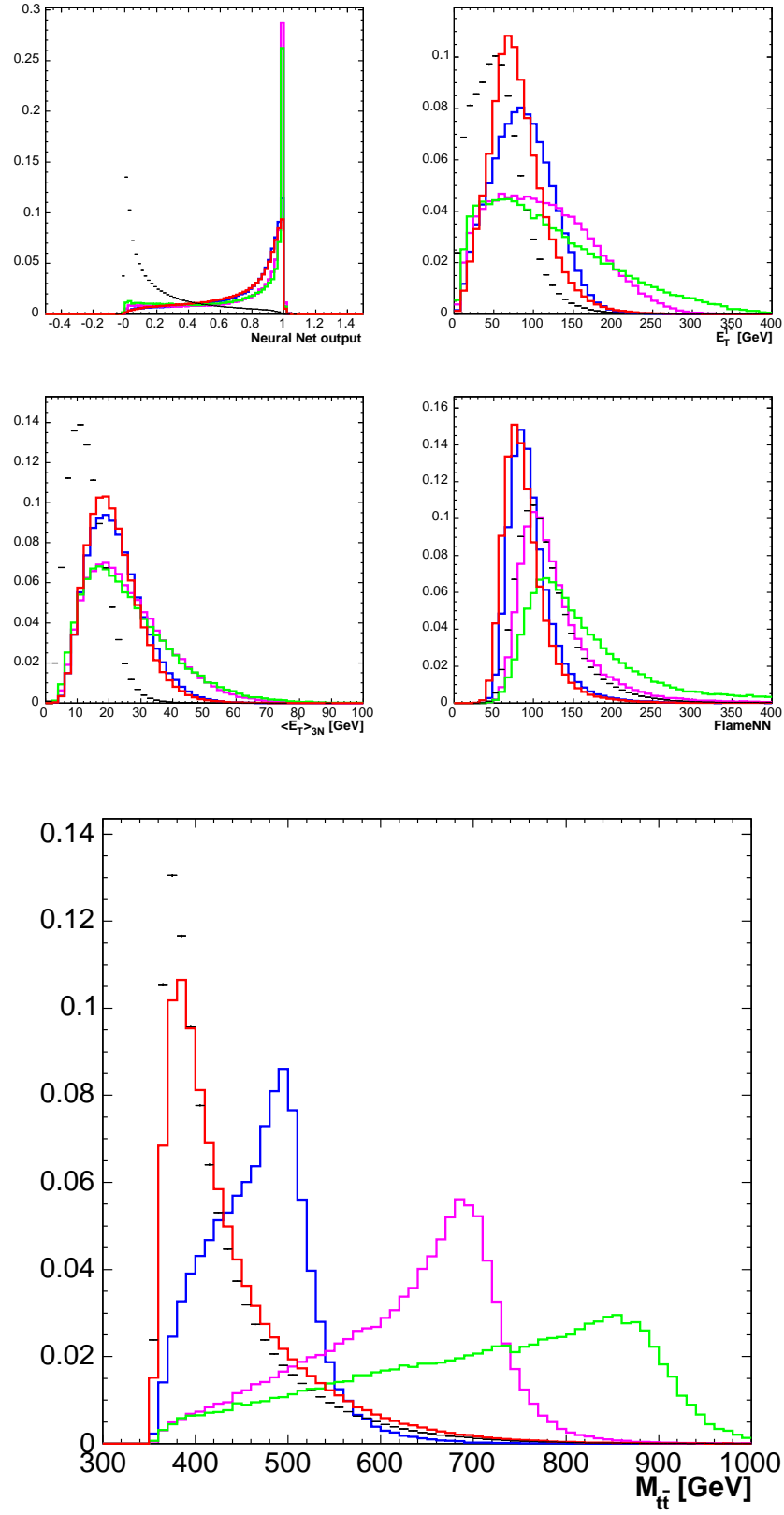


Figure 3-3. Neural net input variables(M_{X_0} and NNet output for the reference): QCD dominated data - black, SM $t\bar{t}$ - red, 500, 700 and 900 GeV $t\bar{t}$ resonances - blue, magenta and green respectively. All histograms are normalized to unity

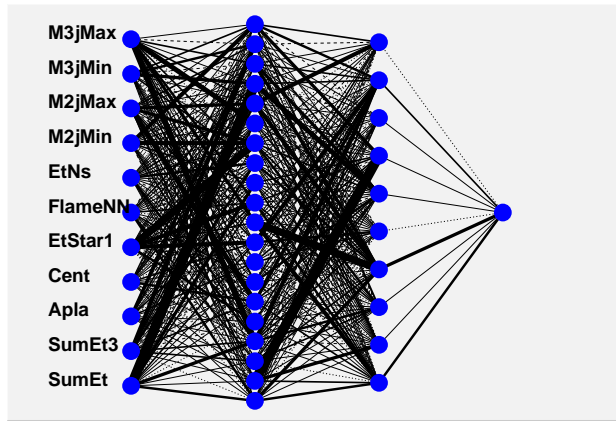


Figure 3-4. Neural net configuration. Synapse thickness is proportional to the weight

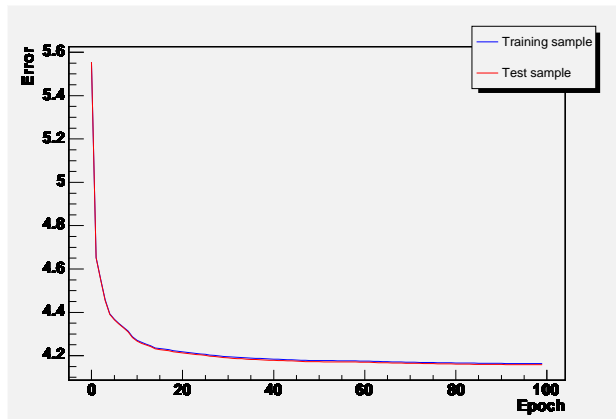


Figure 3-5. Neural net training. Testing(red) and training(blue) errors as a function of training epochs.

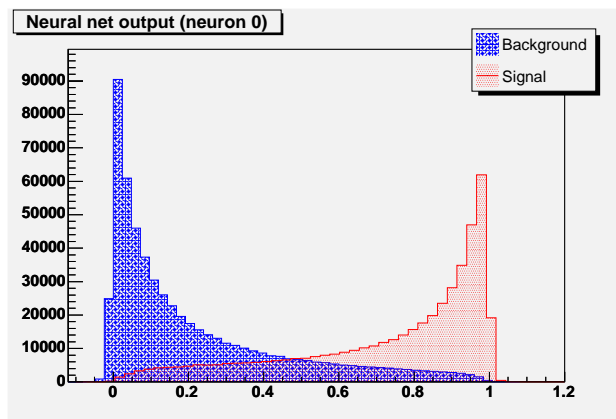


Figure 3-6. Neural net output. Signal(red) and background(blue).

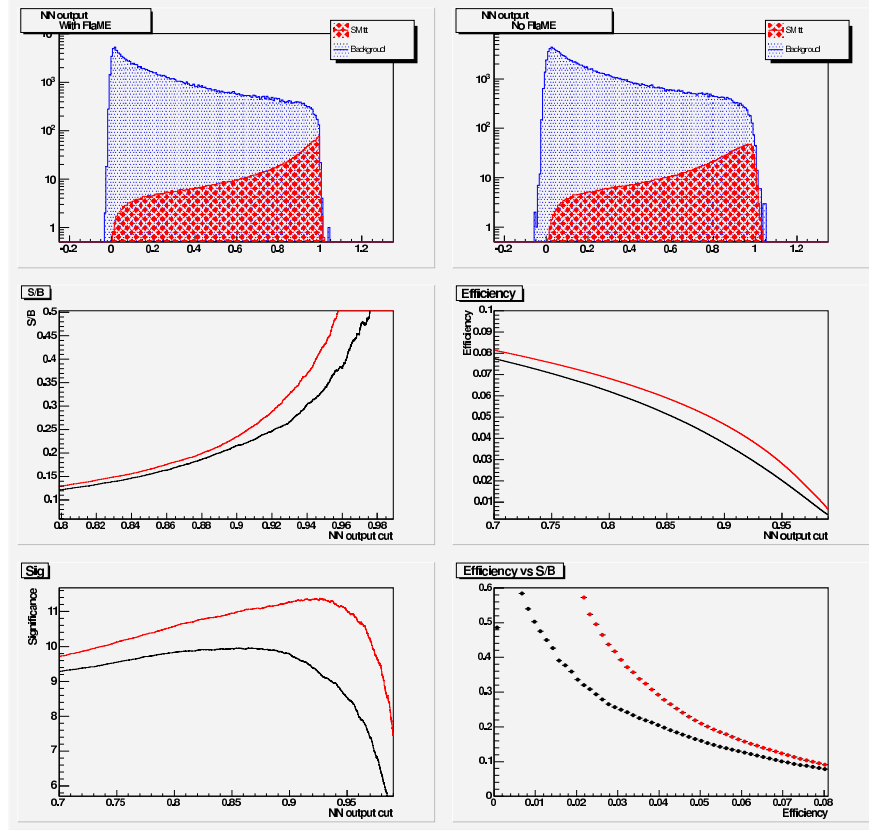


Figure 3-7. Neural net output. Signal is SM $t\bar{t}$, normalized to the number expected of events. Signal(red) and background(blue). Bottom four plots show S/B, Efficiency, Significance and Efficiency vs S/B plots for Neural net configurations with(red) and without(black) FlameNN variable.

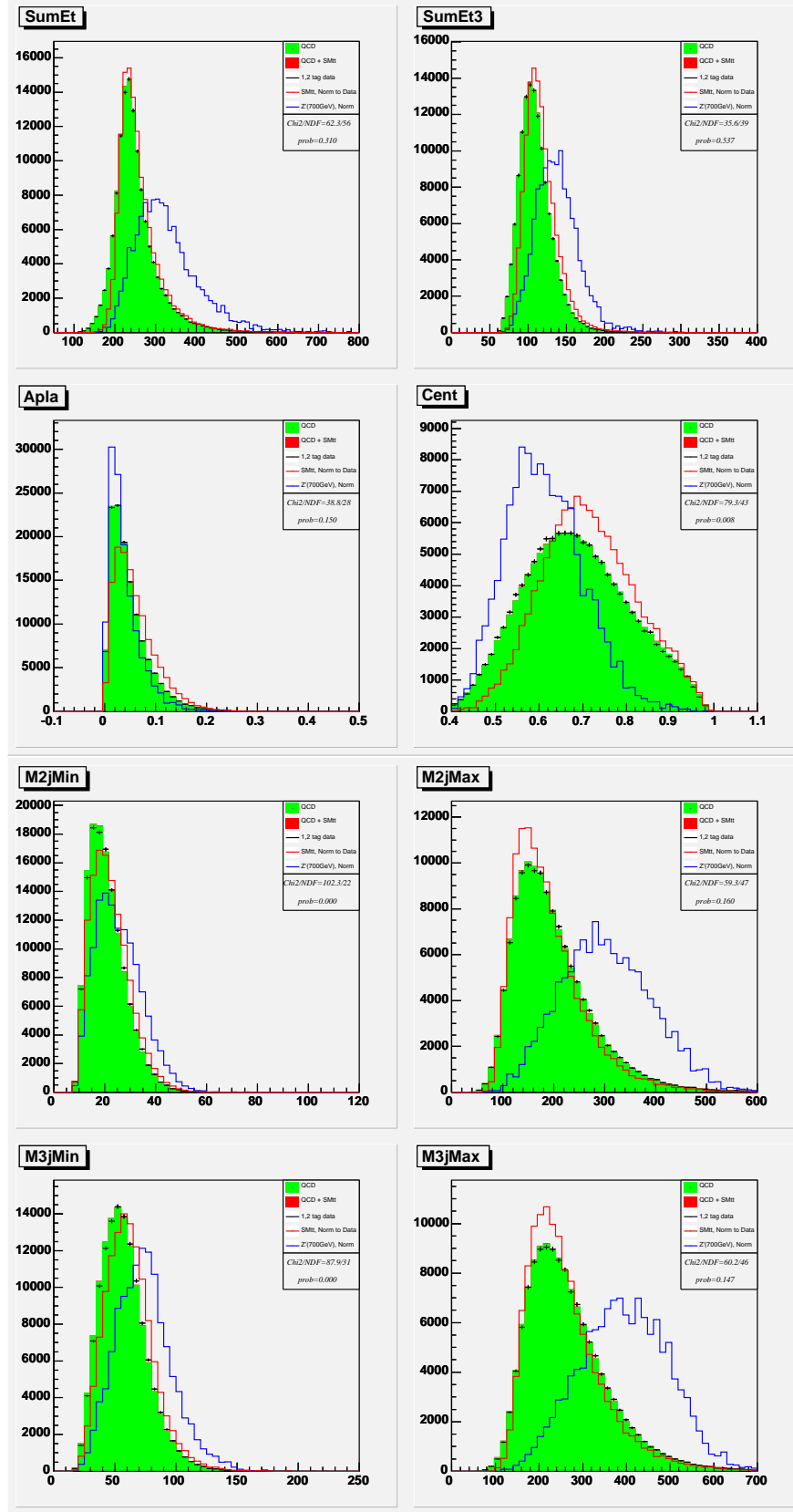


Figure 3-8. First control region: $0 < NNet < 0.25$. Red stack is the prediction by tag rate matrix, black points are actual 1,2 tag data events

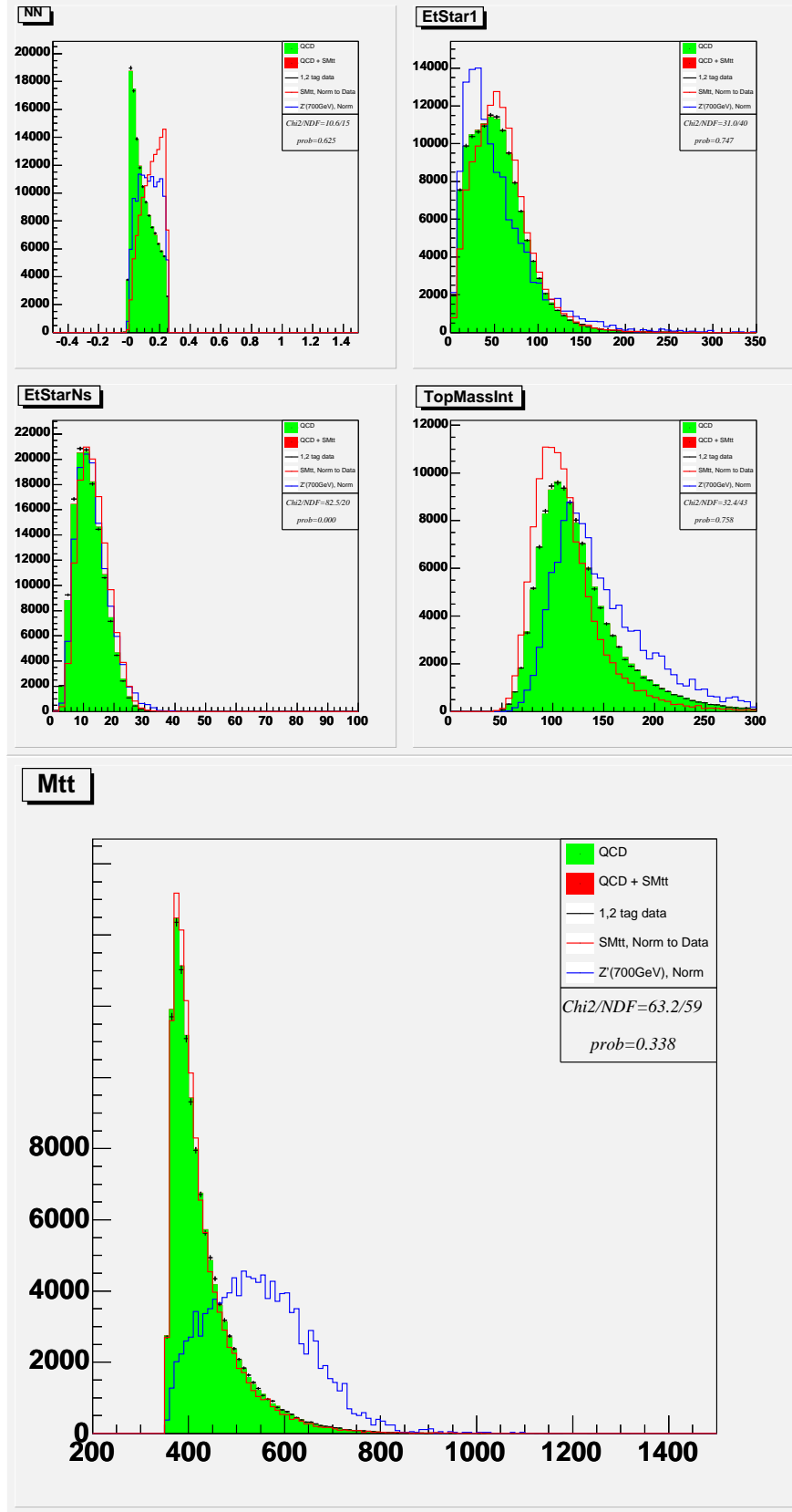


Figure 3-9. First control region: $0 < NNet < 0.25$. Red stack is the prediction by tag rate matrix, black points are actual 1,2 tag data events

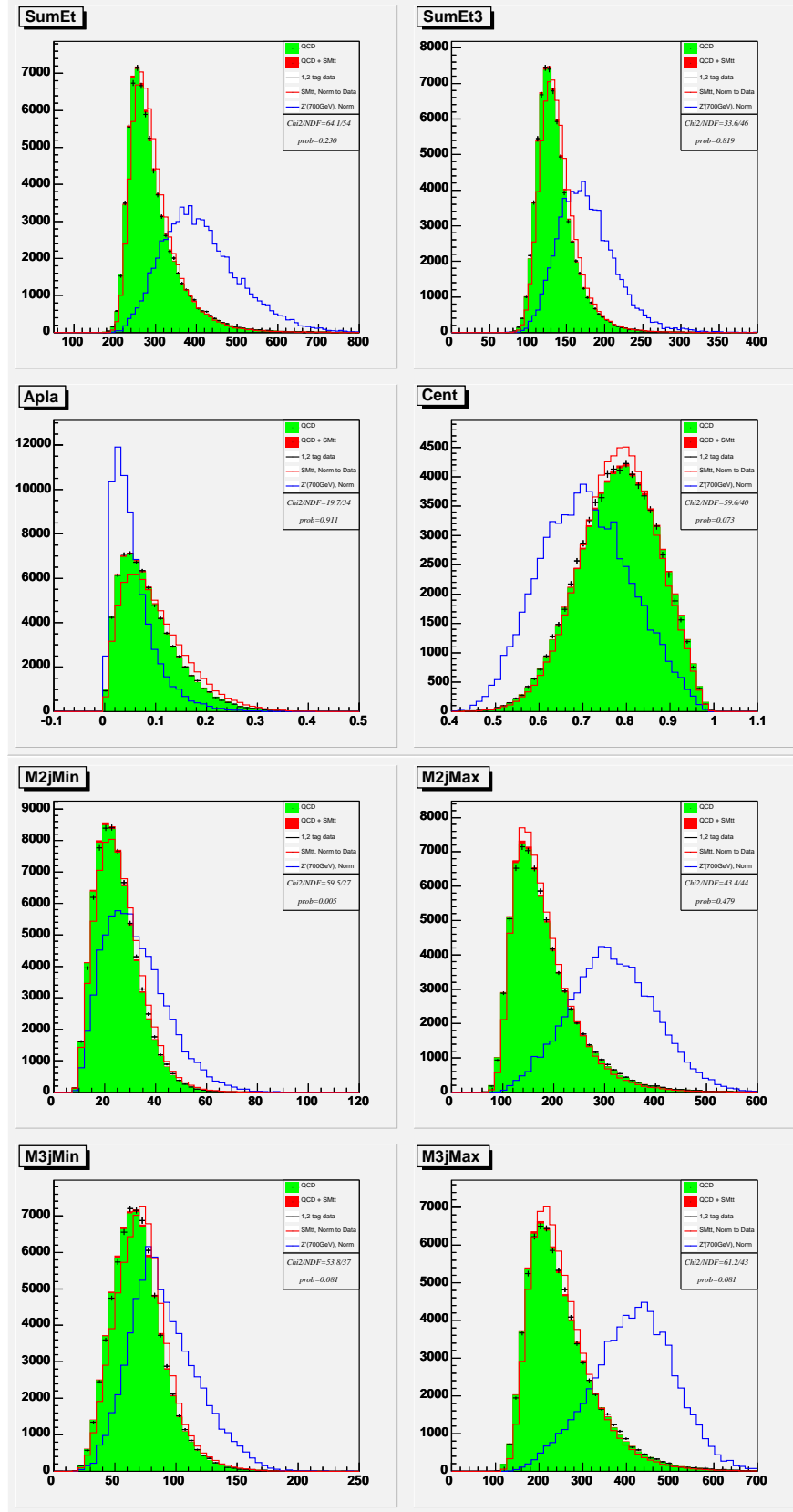


Figure 3-10. Second control region: $0.25 < NNet < 0.75$. Red stack is the prediction by tag rate matrix, black points are actual 1,2 tag data events

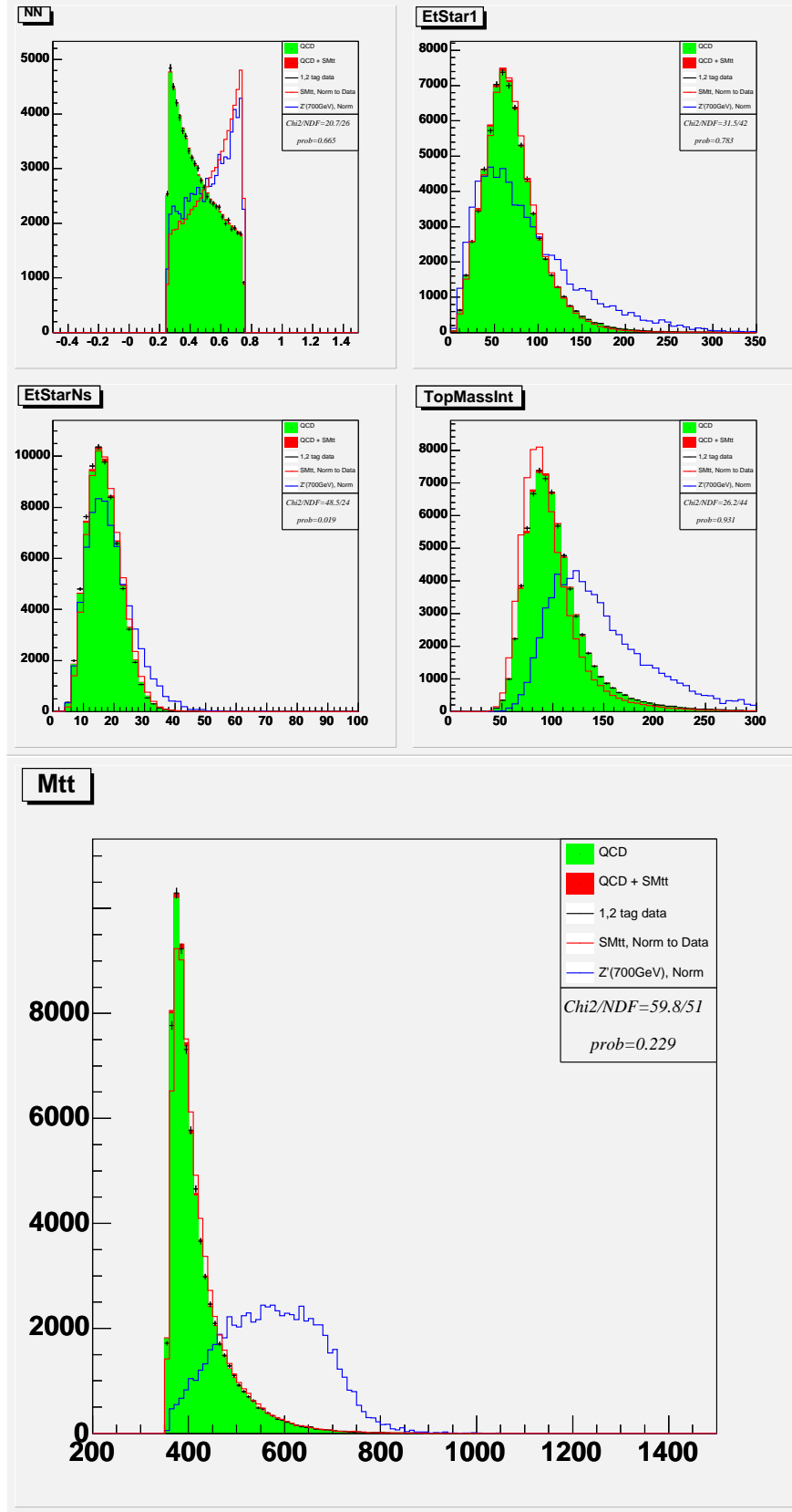


Figure 3-11. Second control region: $0.25 < NNet < 0.75$. Red stack is the prediction by tag rate matrix, black points are actual 1,2 tag data events

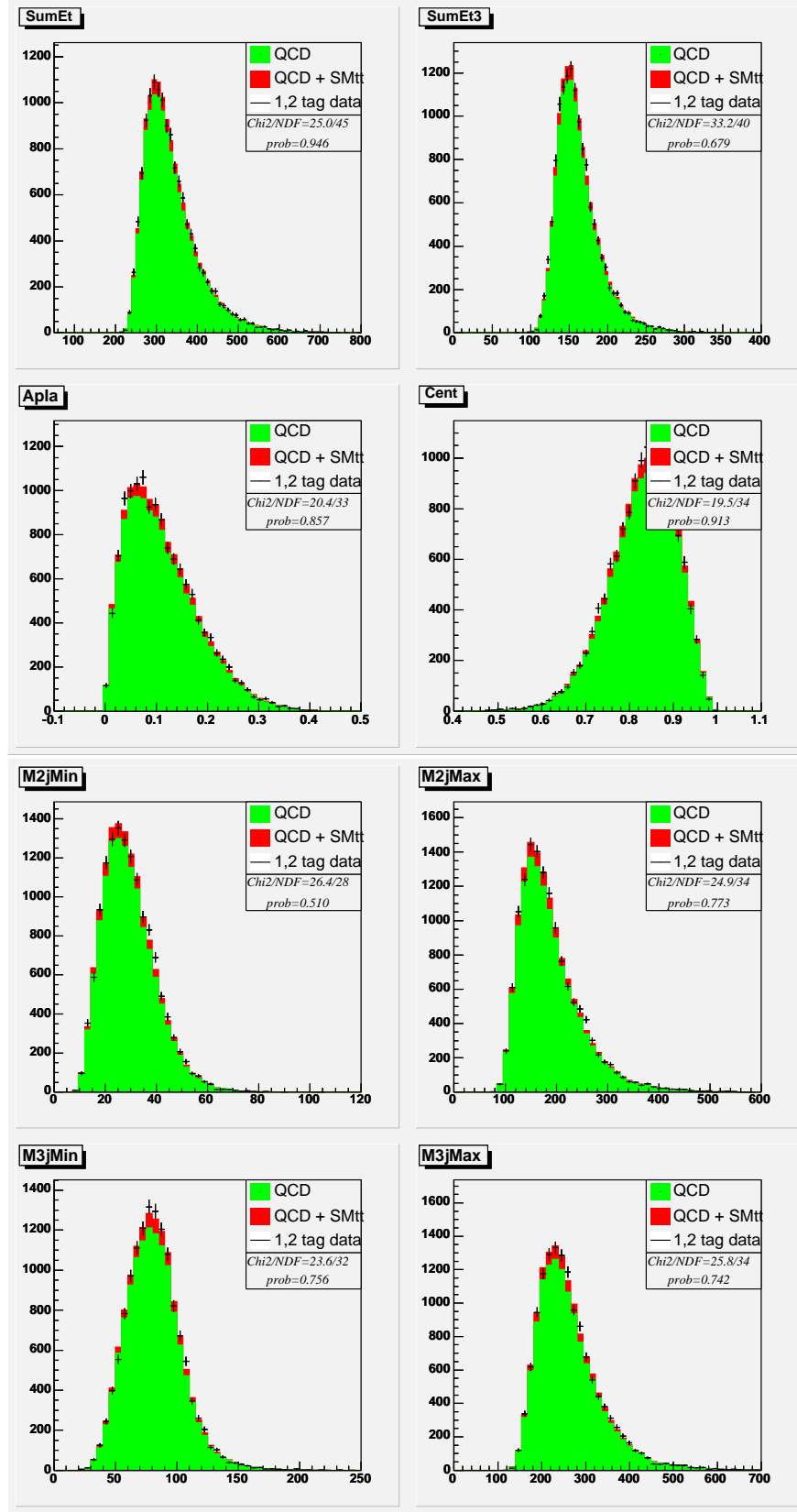


Figure 3-12. Third control region: $0.75 < NNet < 0.93$. Red stack is the prediction by tag rate matrix, black points are actual 1,2 tag data events

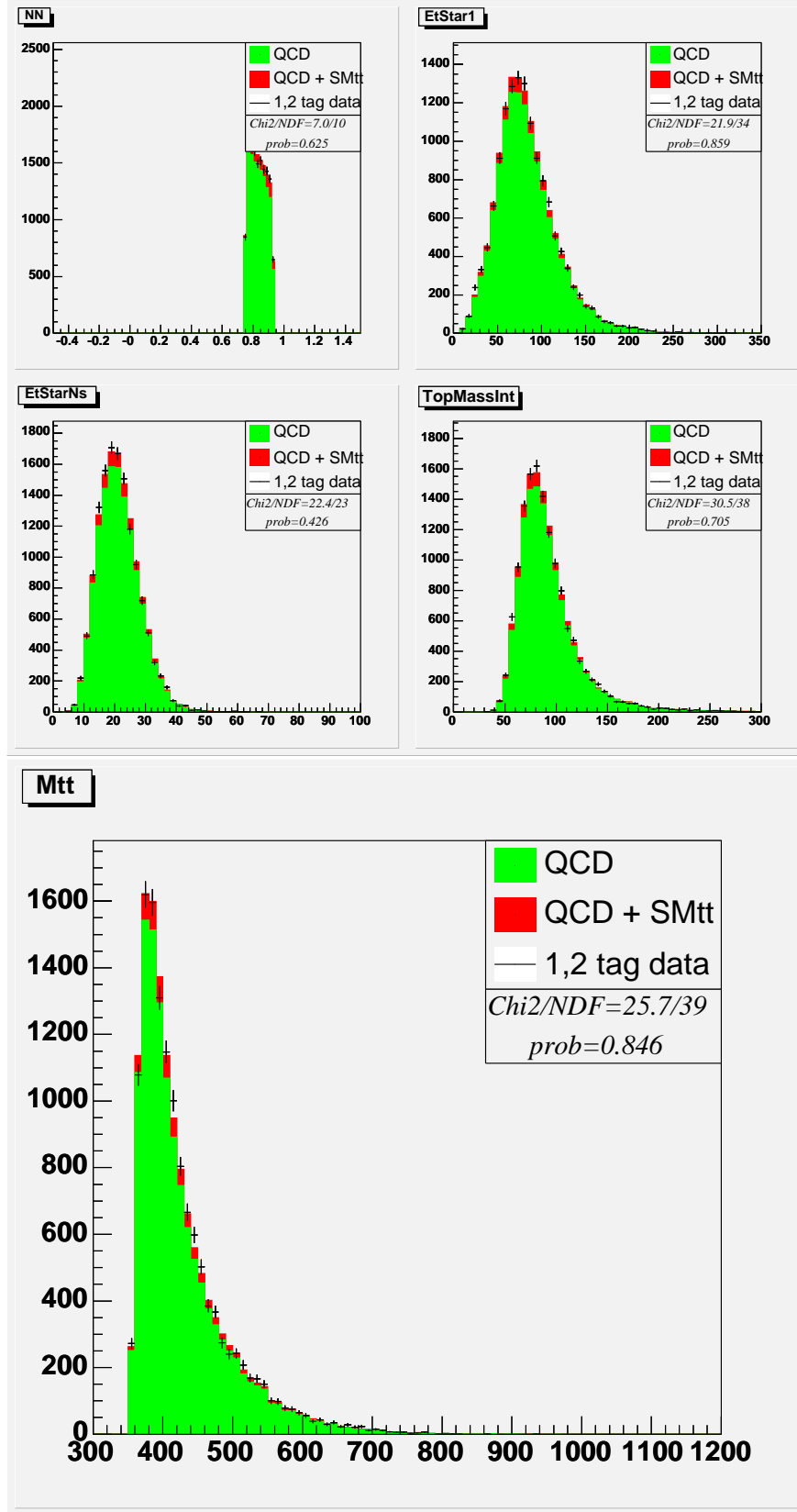


Figure 3-13. Third control region: $0.75 < NNet < 0.93$. Red stack is the prediction by tag rate matrix, black points are actual 1,2 tag data events

CHAPTER 4 FLAME ALGORITHM

4.1 Construction of the Likelihood

We use the leading order (LO) term in the SM $t\bar{t}$ cross section-formula. Therefore the final state is made up of the 6 decay products of the $t\bar{t}$ system only. Let $\vec{p}_i, i = 1 - 6$ be their 3-momenta. In this case the following equation holds true:

$$\vec{P}_6^T = \sum_{i=1}^6 \vec{p}_i = 0$$

and it will be used in all top mass tests we will show in this chapter. In reality we have ISR and FSR which leads to a non-zero \vec{P}_6^T . Still, the average \vec{P}_6^T is null so constraining it to 0 should not bias the result for top mass but maybe only increase the statistical error. For the resonance search analysis though we will use the \vec{P}_6^T distribution from MC and integrate over it since it helps narrow the reconstructed resonance peak.

The probability of a given parton level final state configuration \vec{p}_i is given by:

$$dP(\vec{p}_i|m_{top}) = \frac{1}{\sigma(m_{top})} \int dz_a \int dz_b f_k(z_a) f_l(z_b) d\sigma_{kl}(\vec{p}_i|m_{top}, z_a \vec{P}, z_b \vec{P}) \equiv \pi_{part}(\vec{p}_i|m_{top}) \prod d^3 \vec{p}_i$$

Indices k, l cover the partons types in the proton and antiproton respectively. A sum over both indices is implied. The parton distribution functions (PDFs) are given by $f_k(z)$.

Plugging in the differential cross-section formula

$$d\sigma_{kl}(\vec{p}_i|p_k, p_l) = \frac{|\mathcal{M}_{kl}|^2}{4E_k E_l |v_k - v_l|} (2\pi)^4 \delta^4(p_k + p_l - \Sigma p_i) \prod \frac{d^3 \vec{p}_i}{(2\pi)^3 2E_i}$$

one can obtain the explicit form for $\pi_{part}(\vec{p}_i|m_{top})$. The top mass (m_{top}) enters as a parameter. We combine the probability densities (π) of all available events into a joint likelihood as function of m_{top} :

$$L(m_{top}) = \pi_1 \pi_2 \dots \pi_n$$

Monte Carlo studies show that maximizing this likelihood with respect to the parameter (m_{top}) yields its correct (input) value, as expected.

The treatment of more realistic situations in which we don't measure the final state completely or accurately enough follows the same line of thought, basically we compute the probability density of observing a 6 j :

The jet 3-momenta are denoted by \vec{j}_i and the parton 3-momenta by \vec{p}_i . $T_i(\vec{j}|\vec{p})$ is the probability density that a parton of 3 momenta \vec{p} will end up being measured as a jet of 3 momenta \vec{j} , better known as parton to jet transfer functions. We use different transfer functions for b quarks and lighter quarks so we added an index. If \vec{p}_1 and \vec{p}_2 are the momenta of the b-quarks then $T_1 = T_2 = T_b$ and $T_3 = T_4 = T_5 = T_6 = T_{light}$. In practice we approximate the parton direction with the jet direction which introduces a couple of delta functions in the integral.

Even with b-tagging information there no unique assignment of jets to parton. This indistinguishability is solved by summing over all *allowed* permutations via the $\rho \in S_4$ permutation variable. In this analyses, we found that tagging information does not improve the shape of Z' reconstructed template, so we use all 360 combinations.

The procedure to extract the top mass is the same as in the idealized case of a perfect measurement of the final state discussed before, i.e. combine all events in a joint likelihood and maximize it with respect to the parameter m_{top} .

4.2 The Matrix Elements (ME)

The ME for the diagram $q\bar{q} \rightarrow t\bar{t} \rightarrow W^+bW^-\bar{b} \rightarrow q\bar{q}q\bar{q}b\bar{b}$ is not easily calculable analytically without making any approximation. We found it useful to compute the ME directly using explicit spinors and Dirac matrices because this allows us to compute new, non-SM ME very easily in case we want to incorporate them in the method later on (ex.: spin 0, spin 1, interference, no interference).

Ignoring numerical factors the quark annihilation diagram amplitude is given by

$$\begin{aligned}\mathcal{M}_{q\bar{q}} \approx & \bar{v}(p_{\bar{q}})\gamma^\mu u(p_q) \cdot \bar{u}(p_u)\gamma^\beta(1-\gamma^5)v(p_{\bar{d}}) \cdot \bar{u}(p_d)\gamma^\sigma(1-\gamma^5)v(p_{\bar{u}}) \cdot \\ & \bar{u}(p_b)\gamma^\alpha(1-\gamma^5)\frac{\not{p}_t+m_t}{p_t^2-m_t^2+im_t\Gamma_t}\gamma^\nu\frac{\not{p}_{\bar{t}}+m_t}{p_{\bar{t}}^2-m_t^2+im_t\Gamma_t}\gamma^\rho(1-\gamma^5)v(p_{\bar{b}}) \cdot \\ & \frac{g_{\mu\nu}}{(p_q+p_{\bar{q}})^2} \cdot \frac{g_{\alpha\beta}-P_\alpha^{W+}P_\beta^{W+}/m_W^2}{P_{W+}^2-m_W^2+im_W\Gamma_W} \cdot \frac{g_{\rho\sigma}-P_\rho^{W-}P_\sigma^{W-}/m_W^2}{P_{W-}^2-m_W^2+im_W\Gamma_W}\end{aligned}$$

Considering the masses of the light quarks and leptons negligible we can simplify the expression of the W propagators so the ME reads

$$\begin{aligned}\mathcal{M}_{q\bar{q}} \approx & \frac{\bar{v}(p_{\bar{q}})\gamma^\mu u(p_q)}{(p_q+p_{\bar{q}})^2} \cdot \frac{\bar{u}(p_u)\gamma^\alpha(1-\gamma^5)v(p_{\bar{d}})}{P_{W+}^2-m_W^2+im_W\Gamma_W} \cdot \frac{\bar{u}(p_d)\gamma^\sigma(1-\gamma^5)v(p_{\bar{u}})}{P_{W-}^2-m_W^2+im_W\Gamma_W} \cdot \\ & \bar{u}(p_b)\gamma_\alpha(1-\gamma^5)\frac{\not{p}_t+m_t}{p_t^2-m_t^2+im_t\Gamma_t}\gamma_\mu\frac{\not{p}_{\bar{t}}+m_t}{p_{\bar{t}}^2-m_t^2+im_t\Gamma_t}\gamma_\sigma(1-\gamma^5)v(p_{\bar{b}})\end{aligned}$$

The gluon-gluon production mechanism is described by three diagrams [4-2](#)

The matrix element needed in the cross-section formula is

$$|\mathcal{M}_{gg}|^2 = \frac{1}{64} \sum_{color} |\mathcal{A}_1 + \mathcal{A}_2 + \mathcal{A}_3|^2$$

where \mathcal{A}_i are the amplitudes corresponding to the three diagrams. The color sum covers all possible color configurations for the gluons and quarks. This expression is not optimal with regard to CPU time if we were to do these sums as they stand. We can rewrite it as

$$|\mathcal{M}_{gg}|^2 = \frac{1}{64} \sum_{color} (|\mathcal{A}_1|^2 + |\mathcal{A}_2|^2 + |\mathcal{A}_3|^2 + 2 \cdot \text{Re}\{\mathcal{A}_1\mathcal{A}_2^*\} + 2 \cdot \text{Re}\{\mathcal{A}_1\mathcal{A}_3^*\} + 2 \cdot \text{Re}\{\mathcal{A}_2\mathcal{A}_3^*\})$$

This form is very convenient since the color sums can be evaluated for each individual term regardless of the kinematics because the amplitudes are factorized as $\mathcal{A} = \mathcal{A}_{kin} \cdot \mathcal{A}_{color}$

We can write again

$$|\mathcal{M}_{gg}|^2 = f_1 \cdot |\mathcal{A}_1^{kin}|^2 + f_2 \cdot |\mathcal{A}_2^{kin}|^2 + f_3 \cdot |\mathcal{A}_3^{kin}|^2 + Re\{f_{12} \cdot \mathcal{A}_1^{kin} \mathcal{A}_2^{kin*} + f_{13} \cdot \mathcal{A}_1^{kin} \mathcal{A}_3^{kin*} + f_{23} \cdot \mathcal{A}_2^{kin} \mathcal{A}_3^{kin*}\}$$

All the color summing is encoded in the six constants f_i, f_{ij} . We found these to be 3/16, 1/12, 1/12, -3i/16, 3i/16 and -1/48 respectively. We cross-checked against the analytical formula available for the $2 \rightarrow 2$ process described in the diagrams above and found them in perfect agreement. The procedure just presented works as well for the $2 \rightarrow 6$ process and this is how we compute it.

4.3 Approximations. Change of Integration Variables.

The method as presented involves 28 integrals (P_t, P_z of incoming partons 4-momenta of 6 final partons) plus summing over combinatorics. If for instance we choose to set: the $t\bar{t}$ transversal momentum to zero we would reduce the number of integrals by 2, W or Top on shell -4 integrals, artons and jets have the same direction -12 integrals, all quarks except top are massless -8 integrals. This change is not trivial and we will skip the details. We checked it using HEPG level information and it works very well. The jacobian of the transformation is computed as well and in the implementation we always use these variables.

4.4 Transfer Functions

These functions are defined as the probability for a parton of energy E_p to be associated to a jet of energy E_j . The probability density for the transfer functions is:

$$TF(\vec{j}|\vec{p}) \rightarrow \prod_{i=1}^6 TF(\vec{j}_i|\vec{p}_i) \quad (4-1)$$

The transfer functions are built using $t\bar{t}$ (SM and Z') Monte Carlo samples. More exactly, a jet is associated to a parton if its direction is within a cone of $\Delta R = 0.4$ around the parton direction. We say that a jet is *matched* to the parton if no other jet should satisfy this geometrical requirement. We call an event as being a *matched* event if each of the six partons in the final state has a different jet matched to it. Of all the $t\bar{t}$ Monte

Carlo events passing the kinematical selection defined later, about 50% are matched events.

The jets formed by the decay partons of the W bosons have a different energy spectrum than the jets originating from the b quarks. Thus we form different sets of transfer functions depending on the flavor of the parton the jet has been matched to.

The transfer functions are described using a parameterization in bins of the parton energies and of the parton pseudo-rapidities. Table 1 shows the definition of the binning in pseudo-rapidity. The same definition holds for b-jet transfer function and for W-jets transfer functions.

Bin	$ \eta $
1	$0 \rightarrow 0.2$
2	$0.2 \rightarrow 0.6$
3	$0.6 \rightarrow 0.9$
4	$0.9 \rightarrow 1.4$
5	$1.4 \rightarrow 2.0$

Table 4-1. Definition of the binning in parton pseudo-rapidity for the transfer functions parameterization.

The binning in parton energy is defined such that each bin contains at least 5000 entries and it is wider than 5GeV . This is done in each bin of pseudo-rapidity. For each pseudo-rapidity bin, we have about 30 bins in energy binning definition.

In each bin the transfer function is represented by the distribution of the variable $1 - E_{jet}/E_{parton}$. The distributions is smoothed to remove fluctuations. Examples are shown here [4-3](#)

4.4.1 $M_{t\bar{t}}$ Reconstruction

All the tools developed for the top mass can be turned around to reconstruct any variable of interest, in particular $M_{t\bar{t}}$. Let's assume for a moment that we know which is the right combination. In that case

$$P(\{p\}, \{j\}) = \pi_{part}(\{p\}) \cdot T(\{j\}|\{p\})$$

defines the probability that an event has the parton 4-momenta p and is observed with the jet quantities j . Integrating on the parton variables, given the observed jets, we obtain the probability used for the top mass measurement. However, the expression provides a weight for any parton configuration once the jets are measured. Any quantity that is a function of parton 4-momenta can be assigned a probability distribution based on the "master" distribution above, $M_{t\bar{t}}$ included, and this is our approach.

Technically this amounts to the following integration :

$$\rho(x|\{j\}) = \int \pi_{part}(\{p\}) \cdot T(\{j\}|\{p\}) \cdot \delta(x - M_{t\bar{t}}(\{p\})) \{dp\}$$

with $\rho(x|\{j\})$ being the $M_{t\bar{t}}$ distribution in this case. It should be noted that if we remove the delta function we retrieve the event probability formula used for the top mass measurement method presented before, and therefore all the tests presented before are as relevant for $M_{t\bar{t}}$ reconstruction and there is nothing much to be added except histogramming $M_{t\bar{t}}$ during integration. We use the mean of the $M_{t\bar{t}}$ distribution as our event $M_{t\bar{t}}$ value. This is done for every event. With this method we can reconstruct the $M_{t\bar{t}}$ back to the parton level.

In reality we don't know which is the correct combination so we adopt the top mass solution and sum over all allowed combinations in the previous expression. We expect the right combination to contribute more than the others as it happens for the top mass analysis.

4.4.2 Signal and Background Templates

The MC samples for signal and all other SM backgrounds (besides $t\bar{t}$) are reconstructed using the method described above, i.e. we treat them all as if they were SM $t\bar{t}$ events with $m_{top} = 175$ GeV. Figure 4-4 shows actual signal templates used in analysis. Data events are obviously treated in the same fashion.

- **Signal samples** We generated signal samples with resonance masses from 450 GeV up to 900 GeV, every 50 GeV, using Pythia. The peaks match quite well the true value

of the resonance mass. The shoulder is given by the superposition of mismatched events and fake all hadronic events on top of the nice peak from matched events.

Futhermore, pdf has a smearing effect, especially for the higher Z' masses.

- QCD For QCD we use a template driven from data to extract the shape.
- $SMt\bar{t}$ Template is built from $SMt\bar{t}$ Pythia generated sample with $M_{top}=175GeV$

These templates are used to fit the data. More details on the relative weights and procedure follow in the next sections.

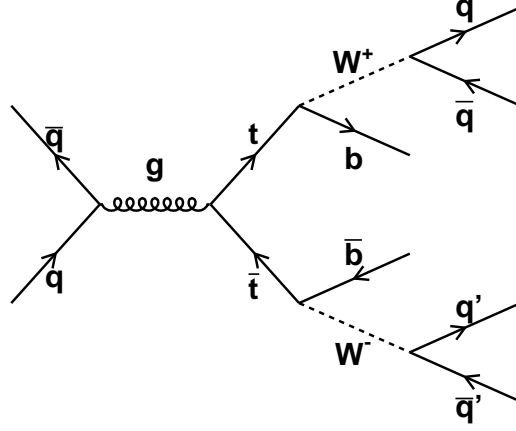


Figure 4-1. Tree level Feynman diagram for the process $q\bar{q} \rightarrow t\bar{t} \rightarrow b\bar{b}q\bar{q}q'\bar{q}'$

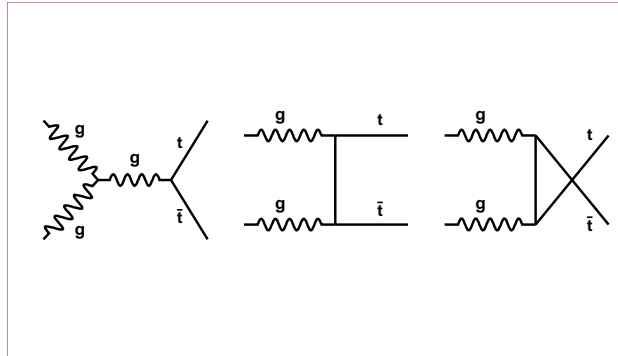


Figure 4-2. Gluon-gluon LO contribution to $t\bar{t}$ production in $p\bar{p}$ collisions

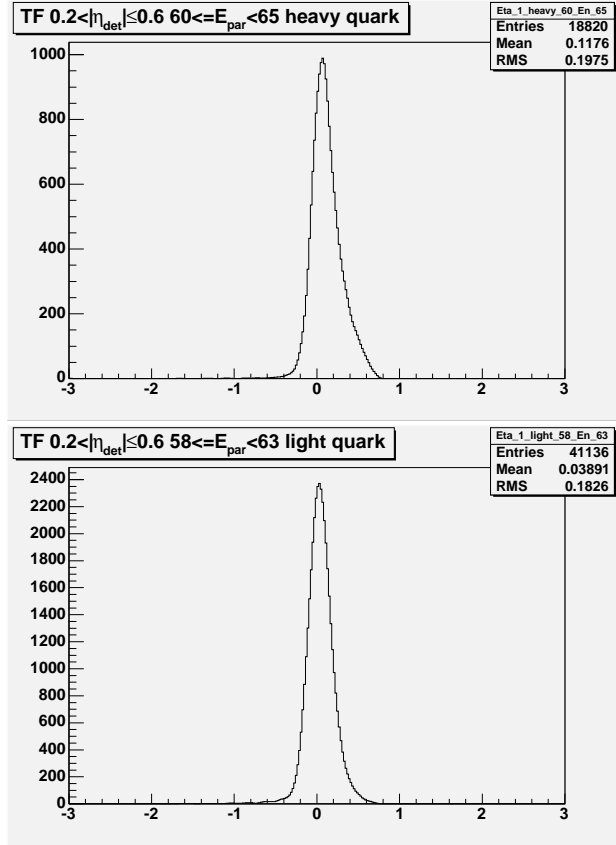


Figure 4-3. Light/B quarks transfer functions ($x = 1 - \frac{E_j}{E_p}$), binned in pseudorapidity region $[0.2, 0.6]$

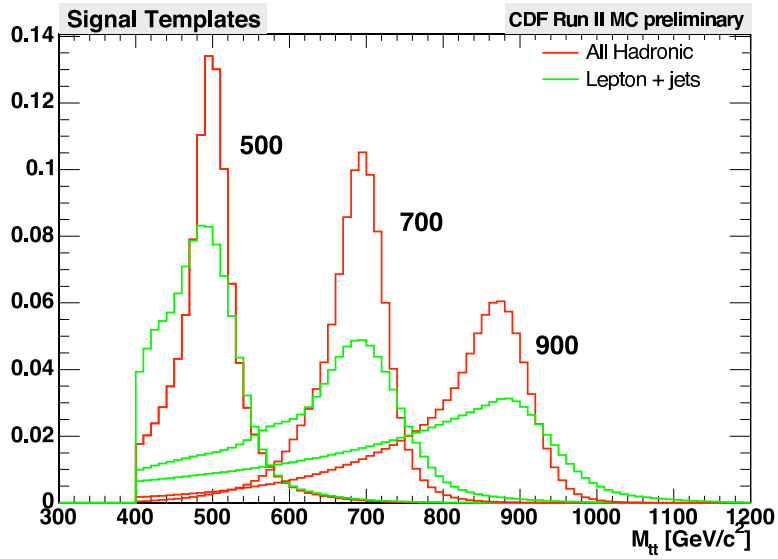


Figure 4-4. $M_{t\bar{t}}$ reconstruction for Z' samples in All hadronic and Lepton plus jets channels

CHAPTER 5 SENSITIVITY

This chapter describes the algorithm used for establishing lower and upper limits for signal cross-section times branching ratio at any desired confidence level (CL). We used a Bayesian approach which was shared with other CDF analyses.

5.1 Upper Limit Setting and Sensitivity Calculation

We implemented the tools to calculate upper/lower limits and measure cross sections for Poisson processes adopting a Bayesian approach; the main idea and suggestions for the implementation can be found in [68, 69].

5.2 Method

Given the observation of some data, $\mathbf{n} = (n_1, n_2, \dots, n_{nbins})$, for example in a mass spectrum, we may want to extract a parameter of interest in this observation; let's call it σ . To infer something about σ we may need also to know other parameters, $\boldsymbol{\nu} = (\nu_1, \nu_2, \dots)$, we are not interested on; these parameters are called *nuisance parameters*. The observation defines a probability density function $f(\mathbf{n}|\sigma, \boldsymbol{\nu})$ for \mathbf{n} , which is, by definition, proportional to the likelihood function of the measurement $\mathcal{L}(\sigma, \boldsymbol{\nu}|\mathbf{n})$, considered as a function of $(\sigma, \boldsymbol{\nu})$.

In Bayesian statistics σ and $\boldsymbol{\nu}$ are considered as random variables which can be represented by probability distribution functions. We can then introduce a prior density $\pi(\sigma, \boldsymbol{\nu})$ for the parameters which describes our knowledge about them before to perform the experiment. The Bayes theorem allows then to connect the likelihood of the measurement to the posterior density of σ and $\boldsymbol{\nu}$ *after* the measurement and update our knowledge about these parameters:

$$p(\sigma, \boldsymbol{\nu}|\mathbf{n}) = \mathcal{L}(\sigma, \boldsymbol{\nu}|\mathbf{n})\pi(\sigma, \boldsymbol{\nu})/p(\mathbf{n}) \quad (5-1)$$

where $p(\mathbf{n})$ is the marginal probability density of the data

$$p(\mathbf{n}) = \int d\boldsymbol{\nu} \int d\sigma \mathcal{L}(\sigma, \boldsymbol{\nu}|\mathbf{n})\pi(\sigma, \boldsymbol{\nu}).$$

To obtain the posterior probability density $p(\sigma|\mathbf{n})$, we integrate over the nuisance parameters $\boldsymbol{\nu}$.

$$p(\sigma|\mathbf{n}) = \int d\boldsymbol{\nu} p(\sigma, \boldsymbol{\nu}|\mathbf{n}) \quad (5-2)$$

From the posterior $p(\sigma|\mathbf{n})$ then we can extract the information about the parameter of interest σ , like the most probable value, upper and lower limits up to a given confidence level, etc...

The application of the described idea to our analysis is pretty straightforward. The data \mathbf{n} we observe is the $t\bar{t}$ mass spectrum, the parameter of interest σ is the resonant $t\bar{t}$ production cross section σ_{X_0} and the nuisance parameters are: for the signal, the integrated luminosity and acceptance; for the background, the integrated luminosity, acceptances and cross sections.

In order to build the likelihood we need also to have the normalized templates for the signal and the backgrounds. We will use the notation T_j with $j \in \{s, \mathbf{b}\}$ for the binned signal and background templates, and T_{ji} for the i -th bin of the j -th template.

Given the above definitions we can write the *expected* number of events in the i -th bin of the spectrum as

$$\mu_i = \int L dt \cdot \sum_{j \in \{s, \mathbf{b}\}} \sigma_j \epsilon_j T_{ji} = \sigma_s A_s T_{si} + \sum_{j \in \{\mathbf{b}\}} N b_j T_{ji}$$

where we split the signal contribution from the backgrounds and we defined the auxiliary variables $A_s = \int L dt \cdot \epsilon_s$ (also called *effective acceptance*) and $N b_j = \int L dt \cdot \sigma_j \epsilon_j$ with $j \in \{\mathbf{b}\}$.

There are now all the ingredients to build the likelihood:

$$\mathcal{L}(\sigma, \boldsymbol{\nu}|\mathbf{n}) = \prod_{i \in \{nbins\}} \mathcal{P}(n_i|\mu_i) = \prod_{i \in \{nbins\}} \frac{(\sigma_s A_s T_{si} + \sum N b_j T_{ji})^{n_i}}{n_i!} e^{-\sigma_s A_s T_{si} - \sum N b_j T_{ji}} \quad (5-3)$$

As we already pointed out, we may not know exactly A_s and the expected number of events from background, $N b_j$; usually we measure these quantities and their errors from other studies. It is customary to take as priors for these parameters a truncated (to

positive values) gaussian to represent our prior knowledge¹. For the signal cross section σ_s the choice is to take a flat density.

5.3 Implementation

5.3.1 Templates

As pointed out in eq. 5-3, to build the likelihood function we need to know the template distributions for the signal and for the background. To create the templates we take official Top group Monte Carlo samples and Pythia generated-showered samples we produced and simulated by ourselves.

The backgrounds considered:

- $SMt\bar{t}$ (ttop75)
- QCD data driven

The signal samples have been generated using Pythia to generate a vector resonance X_0 state decaying 100% in $t\bar{t}$ with masses $M_{X_0} = \{500, 550, 650, 700, 750, 800, 850, 900\} GeV/c^2$ and widths $\Gamma_{X_0} = 1.2\% \cdot M_{X_0}$. We then run the official CDF simulation and production packages.

To generate the templates we run the event selection and then the FlaME reconstruction algorithm, finally fill histograms with $M_{t\bar{t}}$ ditributions. We fit² signal histograms, $SMt\bar{t}$ and QCD templates used as they are.

5.3.2 Templates Weighting

Eq. 5-3 shows that in order to build the likelihood we need to know the number of background events Nb_j for each background. Since the cross sections for the QCD process is unknown we decided to estimate the number of events from QCD as the balance to the total number of *observed* events in CDF after subtracting the *expected* number of signal

¹ Given that the total efficiency is often the product of several efficiencies, the log-normal prior is often used too.

² This set of the fitting functions guarantees a fit with χ^2 probability always above 20%

and $SMt\bar{t}$ events (which can be calculated since the cross sections and acceptances are known).

In the end the weights for each samples are given in order to satisfy:

$$N_{CDF}^{TOT} = \int \mathcal{L} dt \cdot (\sigma_s \epsilon_s + \sigma_{t\bar{t}} \epsilon_{t\bar{t}}) + QCD^{cont} \quad (5-4)$$

5.3.3 Z' Contamination in QCD Template

From Eq. 5-3 we have, number of events in bin “i”:

$$\begin{aligned} \mu &= \sigma_s A_s T_s + \sigma_{t\bar{t}} A_{t\bar{t}} T_{t\bar{t}} + N_{QCD}^{pure} T_{QCD}^{pure} \\ N_{QCD}^{pure} T_{QCD}^{pure} &= N_{QCD}^{cont} T_{QCD}^{cont} - \sigma_s A_s^{cont} T_s^{cont} - \sigma_{t\bar{t}} A_{t\bar{t}}^{cont} T_{t\bar{t}}^{cont} \end{aligned}$$

Comparing signal templates of predicted and observed values we can assume:

$$T_s = T_s^{cont}$$

So, finally we get:

$$\mu = \sigma_s (A_s - A_s^{cont}) T_s + \sigma_{t\bar{t}} A_{t\bar{t}} T_{t\bar{t}} + N_{QCD}^{cont} T_{QCD}^{cont} - \sigma_{t\bar{t}} A_{t\bar{t}}^{cont} T_{t\bar{t}}^{cont}$$

5.3.4 Data Structure and Algorithm

The functions obtained from the fits are then used to generate smooth templates which are fed into the upper limit and cross section calculation algorithm. The background information is normalized and saved in an array of objects, each element containing: a template histogram, expected number of events per each background, uncertainty on the number of events. Signal information is saved in a similar object with structure: template histogram, effective acceptance $A_s = \epsilon_s \cdot \int L dt$, uncertainty on the acceptance.

Thus the algorithm implementation allows us to easily:

- include or exclude a background
- change the Nb_j/pb^{-1} (events per inverse pb from $j - th$ background)
- change the δNb_j (uncertainty on events from $j - th$ background)
- change signal mass template
- change ϵ_s and $\delta\epsilon_s$ (signal acceptance and its uncertainty)
- change the total integrated luminosity of the PE

5.3.5 Calculation of Posterior

After building the likelihood for a given observation \mathbf{n} according to eq. 5-3 we need to calculate the posterior density for σ_s according to eqs. 5-1, 5-2.³ It is worthwhile to rewrite the equation 5-1 according to our notations.

$$p(\sigma_s; A_s, N_{\mathbf{b}}|\mathbf{n}) = \mathcal{L}(\sigma_s; A_s, N_{\mathbf{b}}|\mathbf{n}) \pi(\sigma_s; A_s, N_{\mathbf{b}}) \quad (5-5)$$

To obtain the posterior probability density for σ_s we carry out the integration on the nuisance parameters A_s and $N_{\mathbf{b}}$ adopting a Monte Carlo method. Following this idea and the suggestions in [69] page 20, we implement the “Sample & Scan” method. We repeatedly (1000 times) sample the priors $\pi(A_s)$ and $\pi_j(N_{b_j})$, which are truncated gaussians with respective widths of δA_s and δN_{b_j} . Then we scan (200 bins) the σ_s up to some value where the posterior is negligible. At each scan point we increment the corresponding bin in a histogram of σ_s with a weight equal to $\mathcal{L}(\sigma_s, A_s, N_{\mathbf{b}}|\mathbf{n}) \cdot \pi(\sigma_s|A_s, N_{\mathbf{b}})$. This yields the posterior density for σ_s .

5.3.6 Cross Section Measurement & Limit Calculation

Once calculated the signal cross section posterior p.d.f we can extract the limit or, if we observe some signal, measure the cross section. We define as our estimator for the cross section the most probable value of the distribution. This assumption is supported by many linearity tests we run both with fake signal templates (gaussians) and with real X_0 templates. Figure 5-1 shows the results of the tests with fake gaussian signal templates of 800 and 900 GeV/c^2 masses (60 GeV/c^2 width) and with FlaME templates for X_0 masses from 650 to 900 GeV/c^2 at an integrated luminosity equal to $\int \mathcal{L} = 1000 pb^{-1}$.

³ Actually we do not calculate this integral since we do not calculate the marginal posterior $p(\mathbf{n})$. So the posterior pdf we calculate is not normalized. This is not a problem since all the infos we are extracting from the posterior are independent from normalization (upper and lower limits, mode, mean, median).

To calculate the limit up to an α confidence level (in our case will be $\alpha = 0.95$) we followed two approaches. The first one looks for a value UL_0 which satisfies

$$\frac{\int_0^{UL_0} p(\sigma|n)}{\int_0^\infty p(\sigma|n)} = \alpha \quad (5-6)$$

The second aims to calculate an interval defined by LL and UL which satisfy

$$\frac{\int_{LL}^{UL} p(\sigma|n)}{\int_0^\infty p(\sigma|n)} = \alpha \quad (5-7)$$

and

$$p(LL|n) = p(UL|n) \quad (5-8)$$

The definitions of UL_0 and UL coincides when $LL = 0$, this happens when there is no or little signal and so the p.d.f peaks close to zero; when signal contamination is increased the p.d.f. peaks far away from the zero and the LL is consistently different from zero.

With these procedures we can extract UL_0 , LL and UL per each PE. Figure 5-2 shows an example of posterior for a PE with input signal of 2 pb , $M_{X_0} = 900\text{ GeV}/c^2$ and total integrated luminosity $\int \mathcal{L} = 1000\text{ pb}^{-1}$. We run many (1000) PEs for each configuration (M_{X_0} , integrated luminosity) and we then fill histograms with the MPV, UL_0 , LL and UL ; for the MPV, UL_0 and UL the median of the histograms are then considered as our estimators, while for the LL we defined the fraction of PEs with $LL \neq 0$ as an estimation of the power of the algorithm in discriminating the presence of a signal out of the background.

5.4 Systematic Errors Accounting

We distinguish between two kinds of systematic uncertainties, acceptance systematics and shape systematics. The first one, mentioned in section 5.2, is due to uncertainty on the signal acceptance or on the backgrounds acceptances or cross sections and does not affect the templates. The effect of these kind of uncertainties has been incorporated into the likelihood by introducing the nuisance parameters priors which reflect their uncertainty and then integrating over them as described in 5.3.5.

Shape systematic uncertainties not only affect the acceptances but also the template shapes, therefore they must be handled in a different way.

5.4.1 Shape Systematics

A change on Jet Energy Scale, initial and final state radiation, parton distribution function, etc. modifies the signal and backgrounds acceptances as well as their templates. To incorporate these systematics uncertainties we adopt the same approach described in [70].

5.4.2 Jet Energy Scale

After applying the energy correction algorithm to jets we are left with some residual uncertainty to the Jet Energy Scale (JES). The effect on the measured X_0 cross section is evaluated by applying a $\pm 1\sigma$ shift on the JES and then running the full reconstruction on signal and background samples; the resulting change in the cross section as a function of the cross section itself is then interpreted as the uncertainty on the X_0 cross section.

The procedure consists in generating pseudoexperiments with shifted templates and acceptances and analyzing them with correct templates and acceptances⁴. The procedure is applied for the integrated luminosity scenario 2.8 fb^{-1} , for 20 signal cross sections $\sigma_{X_0} = 0.25, 0.50 \dots 5.00\text{ pb}^{-1}$ and for 5 input signal masses $M_{X_0} = 500 \dots 900\text{ GeV}/c^2$. for each mass and for both positive and negative JES shifts 5-3.

5.4.3 ISR & FSR

To investigate the effect of the ISR and FSR uncertainties on the analysis we followed the old prescription from top mass group and the method describes in the previous section. We specifically generated Z' samples with ISR/FSR more/less, built the templates using FlaMEalgorithm. Next, we generated PEs with shifted templates and acceptances; the PEs have been then analyzed with the nominal templates and acceptances.

⁴ This to mimic the approach to analysis of the *real* data.

5.4.4 PDFs Uncertainty

One way to estimate PDF uncertainties is by reweighting the events according to a new set of PDFs and check the effect. In this case we change each of the 20 PDF eigenvalues up and down by their errors and thus obtain 40 shifted templates for each unshifted template. The overall acceptance variation is at the order of 1% which is covered by the prior uncertainty on acceptance. The remaining effect if any is due to template shape changes. However, a Kolmogorov-Smirnoff test applied between the central template and the shifted templates returns invariably 1.0000 which confirms our assumptions that PDF uncertainties are negligible for our search.

5.4.5 Overall Shape Systematic Uncertainties

Since we consider each shape systematic uncertainty as independent and gaussian-like, we can calculate the total effect of the shape uncertainties by summing in quadrature each contribution ($\delta\sigma_{X_0}$) versus the signal cross section. Fig. 5-5 shows the shifts for the five signal masses $M_{X_0} = 500 \dots 900 \text{ GeV}/c^2$ at an integrated luminosity of $\int \mathcal{L} = 2.8 \text{ pb}^{-1}$.

5.4.6 Incorporating the Shape Systematics

To incorporate a shape systematics into the bayesian machinery we considered the uncertainty on cross section $\delta\sigma_{X_0}(\sigma_{X_0})$ as a gaussian uncertainty on each point of the posterior probability density function. We then convolute the two according to:

$$PDF_{SYS}(\sigma_{X_0}) = \int_0^\infty \frac{1}{\delta\sigma_{X_0}\sqrt{2\pi}} \exp\left(-\frac{1}{2}\left(\frac{\sigma_{X_0} - \sigma'}{\delta\sigma_{X_0}}\right)^2\right) PDF(\sigma') \cdot d\sigma' \quad (5-9)$$

In performing this calculation we have to pay attention to the finite lower bound (zero) on the integration. The resulting convoluted function has to be still bounded to non negative values. To obtain that the convolving function has to be a normalized truncated gaussian limited to positive values only. The smearing procedure can be applied for each systematics indipendently since the convolution satisfies $(f \otimes g) \otimes h = f \otimes (g \otimes h)$ Fig. 5-6 shows the effect of the smearing on a posterior distribution functions.

5.4.7 Expected Sensitivity With Shape Systematics

After applying the smearing procedure due to shape systematics we calculated the expected sensitivity. Fig. 5-7 shows the expected sensitivity for the two integrated luminosity scenarios $\int 1000 pb^{-1}$.

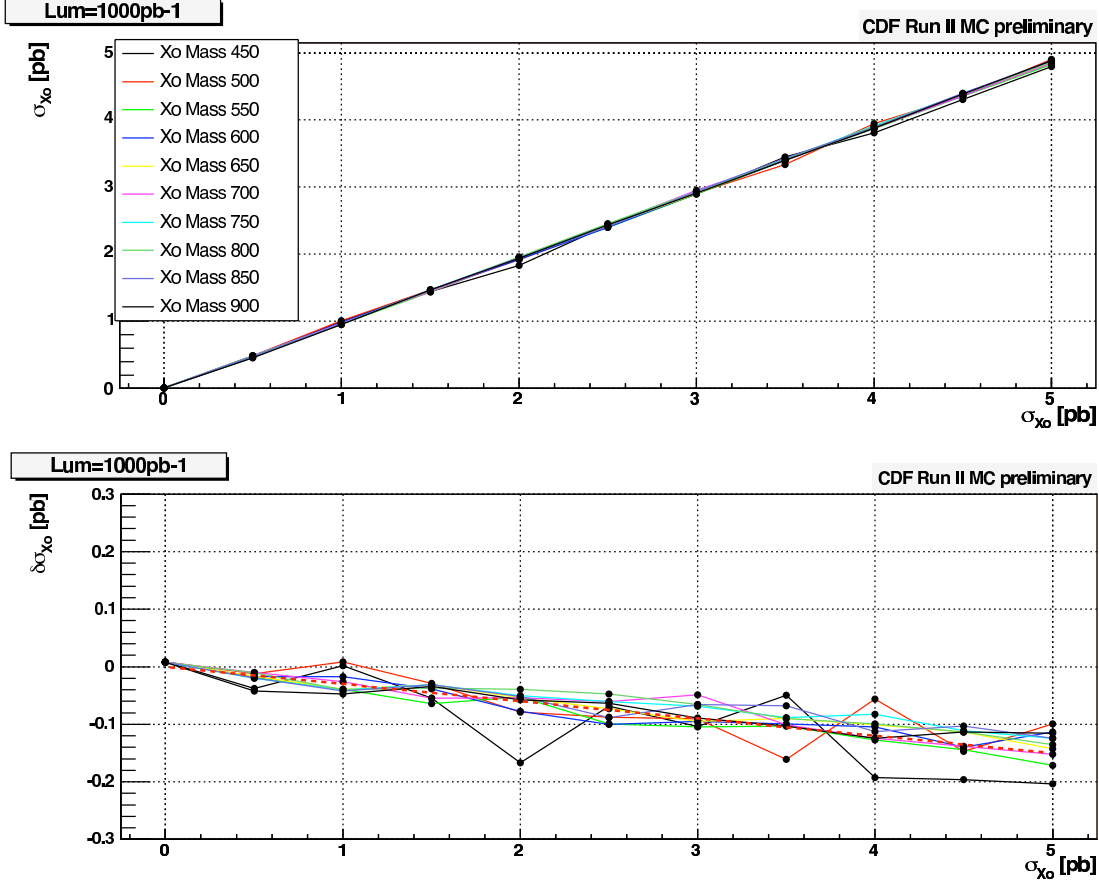


Figure 5-1. Linearity test. The top plots show the input versus the reconstructed cross section after 1000 PE at integrated luminosity $\int \mathcal{L} = 1000 pb^{-1}$. Bottom plots shows deviation from linearity in expanded scale. We estimate the deviation to be about 2%(Red dotted line).

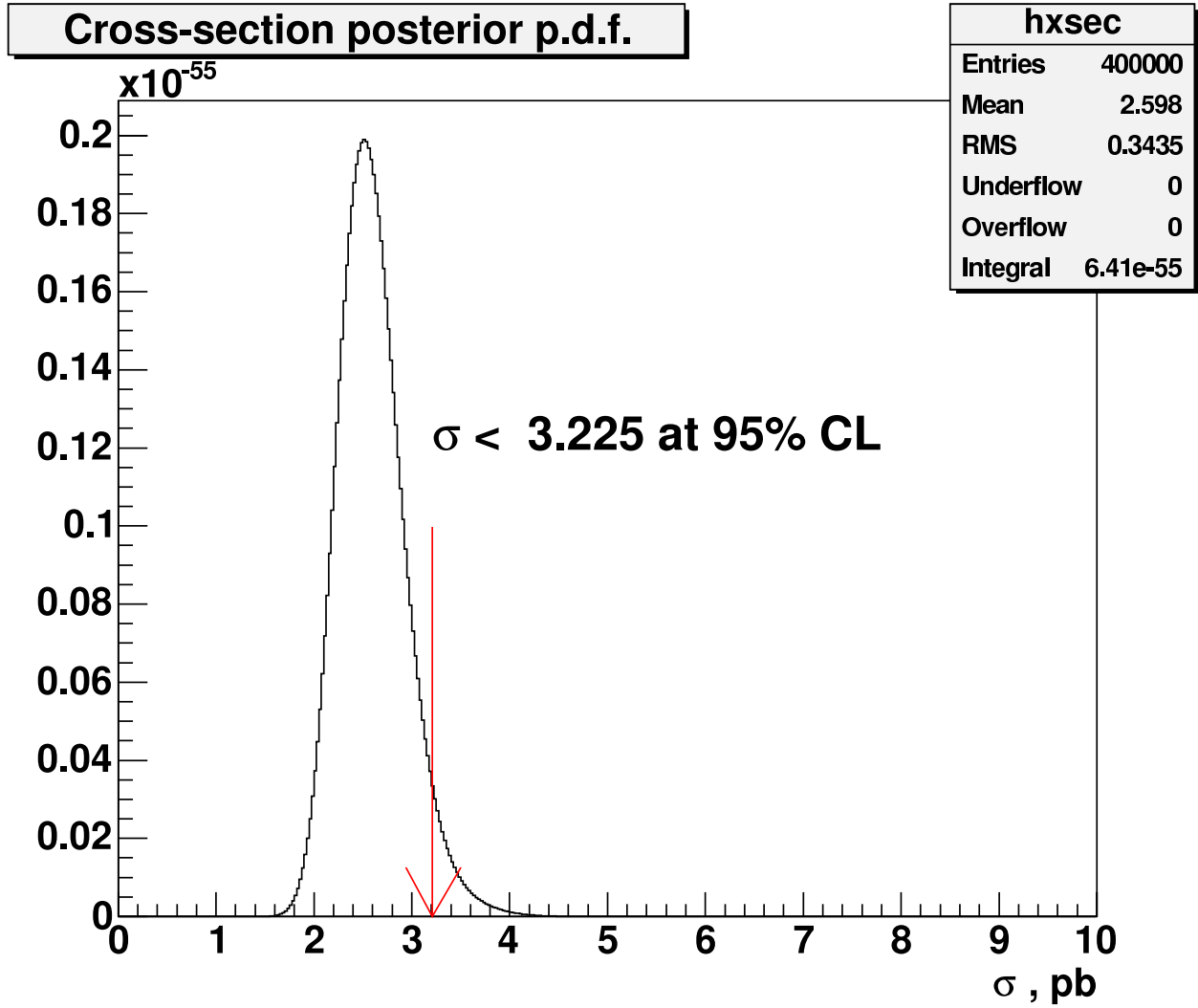


Figure 5-2. Posterior probability function for the signal cross section. The most probable value is assumed as estimator for the cross section. From the posterior we also extract 95% CL upper limit and lower limit. The red arrow and the quoted value correspond to the 95% CL UL_0 .

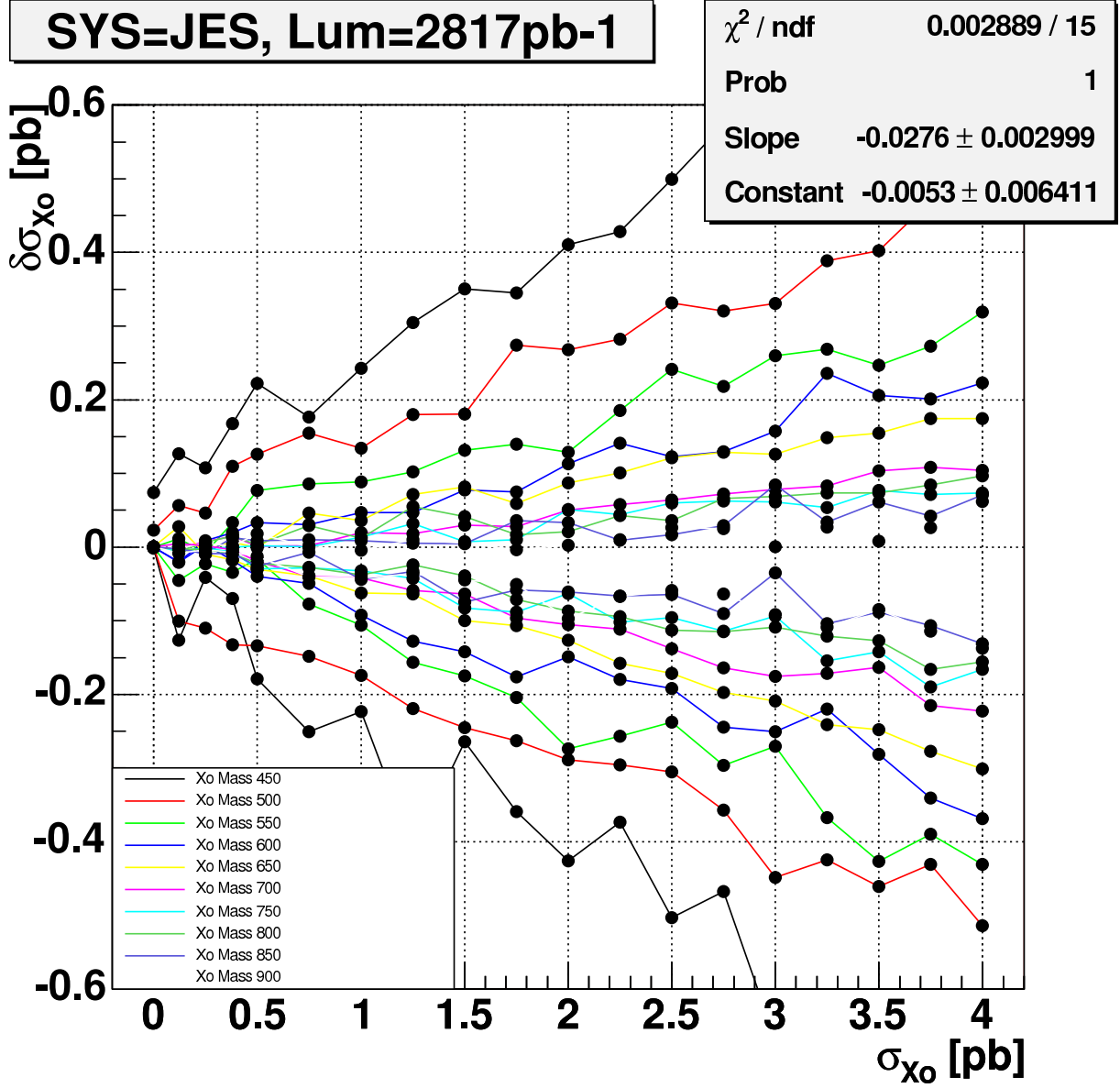


Figure 5-3. Cross section shift due to JES uncertainty for luminosity scenarios $\int \mathcal{L} = 2.8 \text{ fb}^{-1}$. The shift is assumed to be the uncertainty on the cross section due to JES.

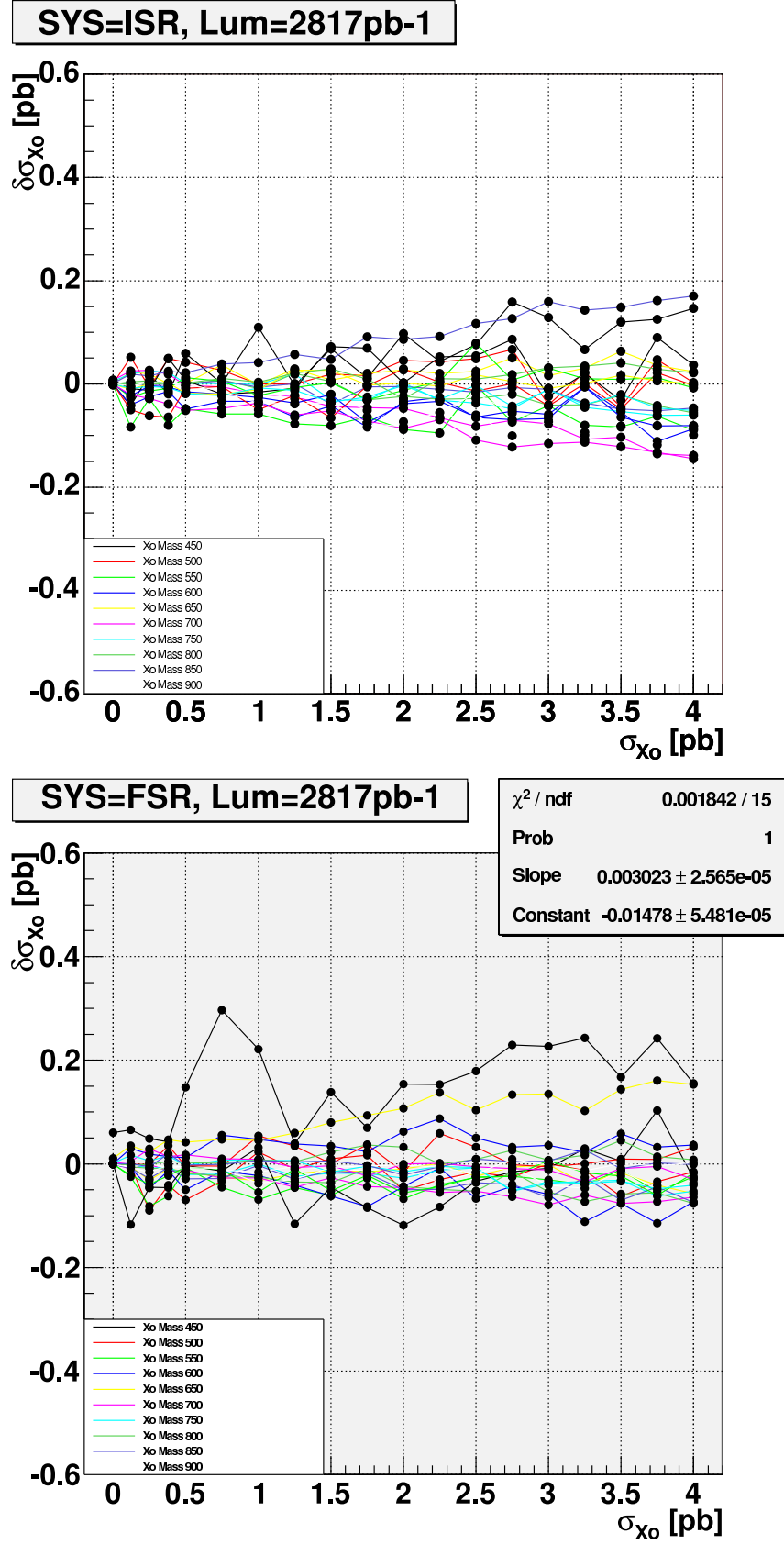


Figure 5-4. Cross section shift due to ISR and FSR uncertainties.

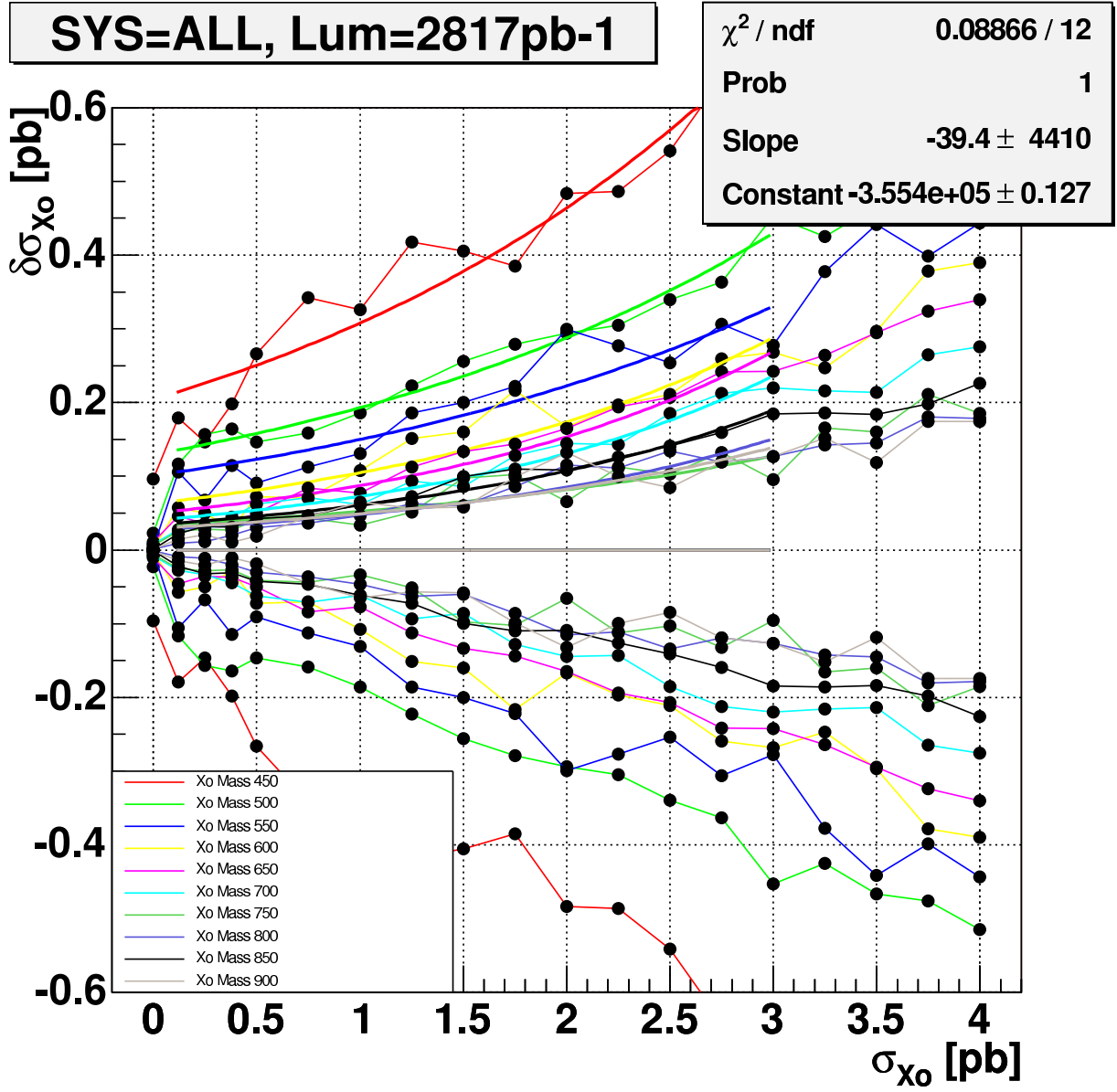


Figure 5-5. Total shape systematic uncertainty versus input signal cross section.

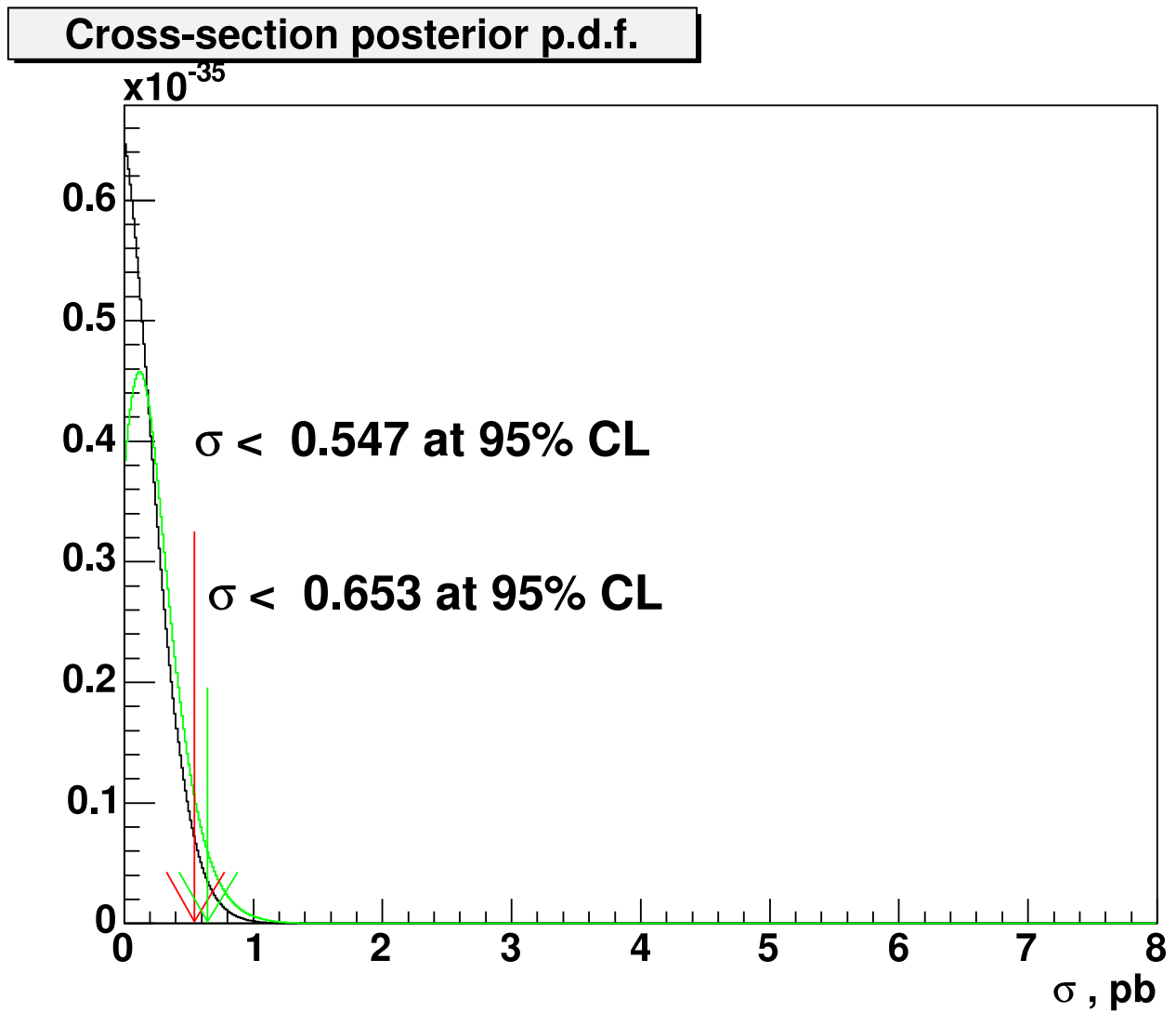


Figure 5-6. Posterior probability function for the signal cross section. The smeared p.d.f. (green) shows a longer tail than the unsmeared one (black). As a consequence the UL_0 quoted on the plot is shifted to higher values with respect to the one calculated on unsmeared posterior.

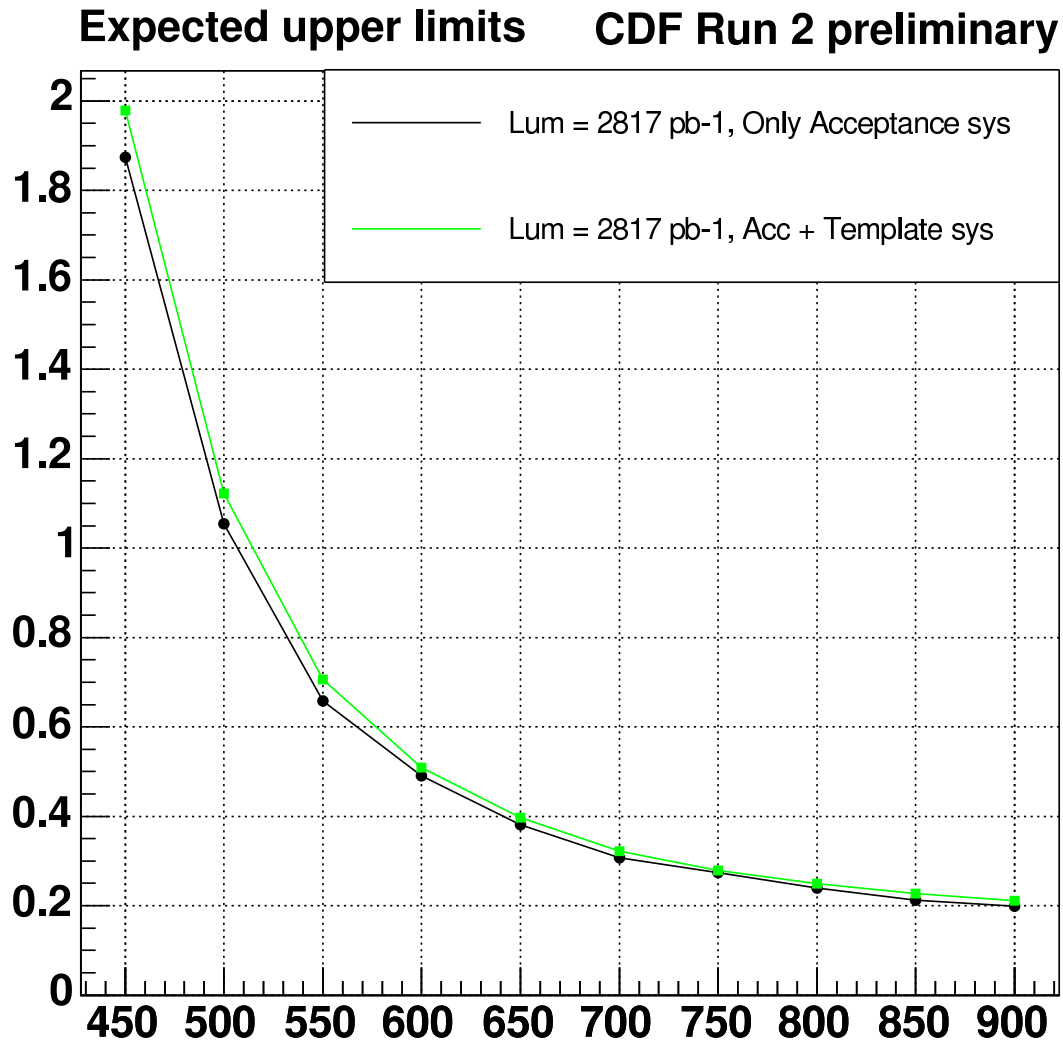


Figure 5-7. Upper limits at 95% CL. The curves shows the results for two luminosity scenarios and both including or excluding the contribution from shape systematic uncertainties.

CHAPTER 6

RESULTS

There are 3177 events passing the event selection and after applying FlaME reconstruction the $M_{t\bar{t}}$ spectrum is shown in Figure 6-1, left plot. 19 events were not reconstructed which means there were no solutions satisfying the W and top mass constraints. The two top quarks and W's are forced to be on shell.

The right plot shows events containing 2 b-tagged jets only, however the upper limits will be calculated using events with 1 or 2 b-jets.

Figure 6-3 shows the spectrum above the 400 GeV cut together with the SM expectation. The 95% confidence level upper limits on signal cross section from data together with the SM expected upper limits are shown in Figure 6-4.

The bands define 68% and 95% CL on the expected upper limit. The central value is the median of the histogram of upper limits from 1000 pseudoexperiments, as mentioned before, and the bands are defined by integrating half the interval on both sides - i.e. 34% of the area on each side of the median in the case of the 68% CL band.

6.1 Conclusion

We have presented a search for resonance production of $t\bar{t}$ pairs decaying in all jets final state. We used the matrix element approach for invariant mass, $M_{t\bar{t}}$, reconstruction, which was implemented in the FlaME algorithm. We as well developed the limit setting methodology used to establish lower and upper limits at any confidence level, incorporating systematics.

The 2.8 fb^{-1} of data collected at CDF shows no indication for new $t\bar{t}$ resonant production mechanisms. Assuming leptophobic topcolor-assisted resonance production, we can exclude resonance masses below $805\text{ GeV}/c^2$. It is the first $t\bar{t}$ resonance search in all jets final state.

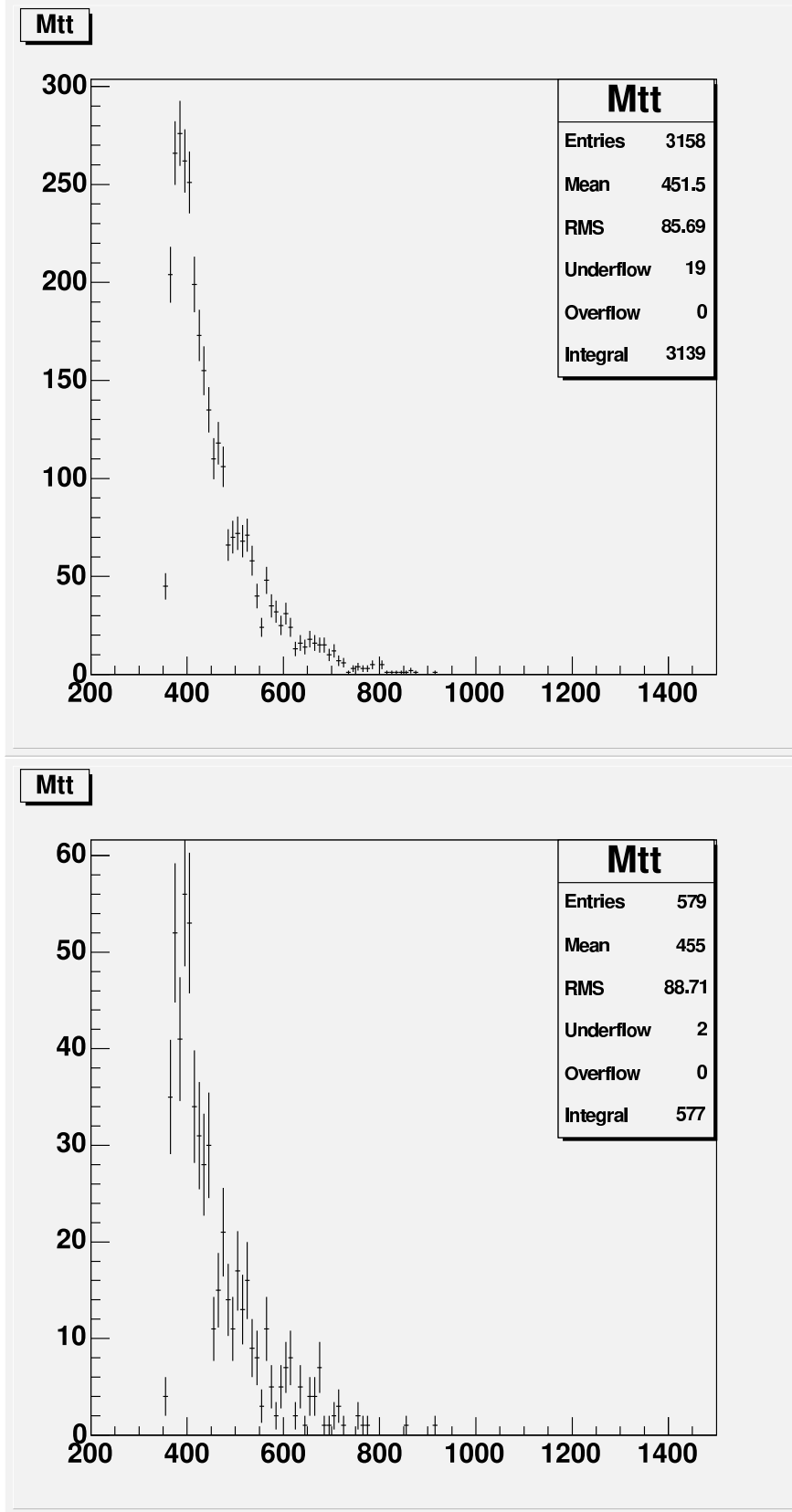


Figure 6-1. $M_{t\bar{t}}$ in CDF Run 2 data, 2.8 fb^{-1}

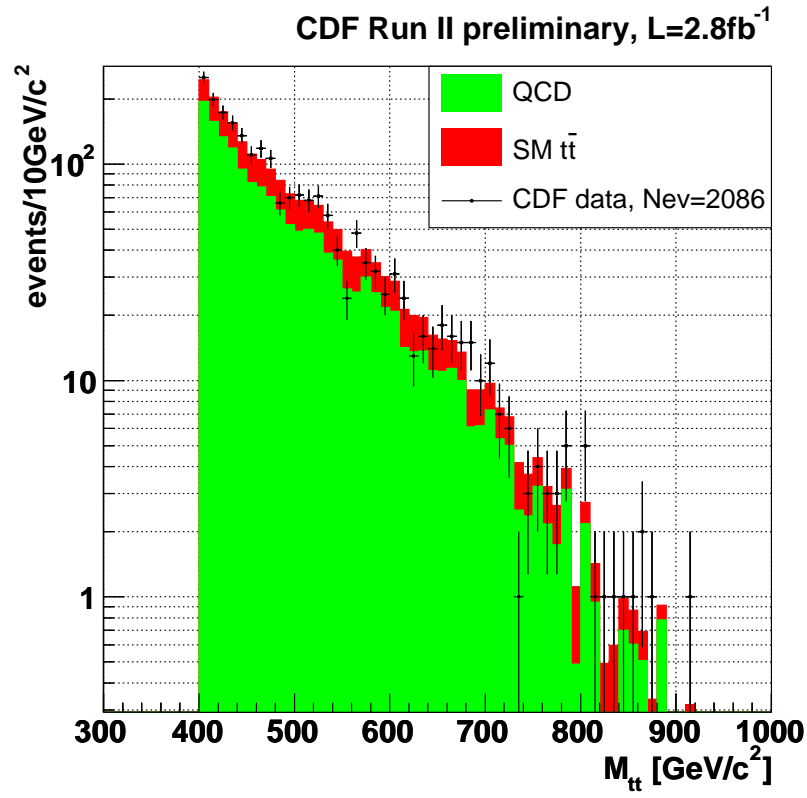
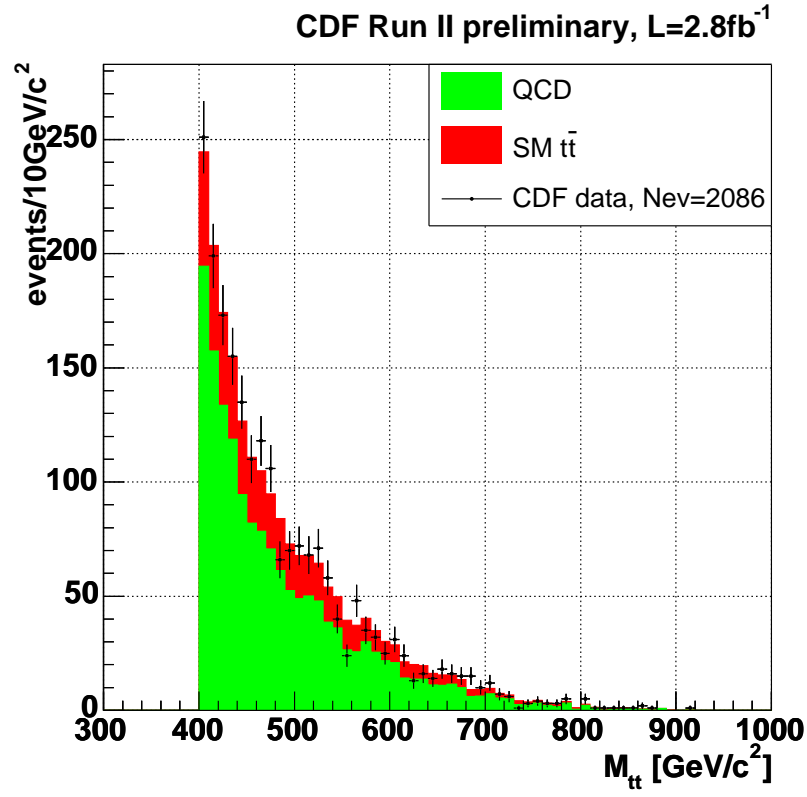


Figure 6-2. $M_{t\bar{t}}$ in CDF Run 2 data, 2.8fb^{-1}

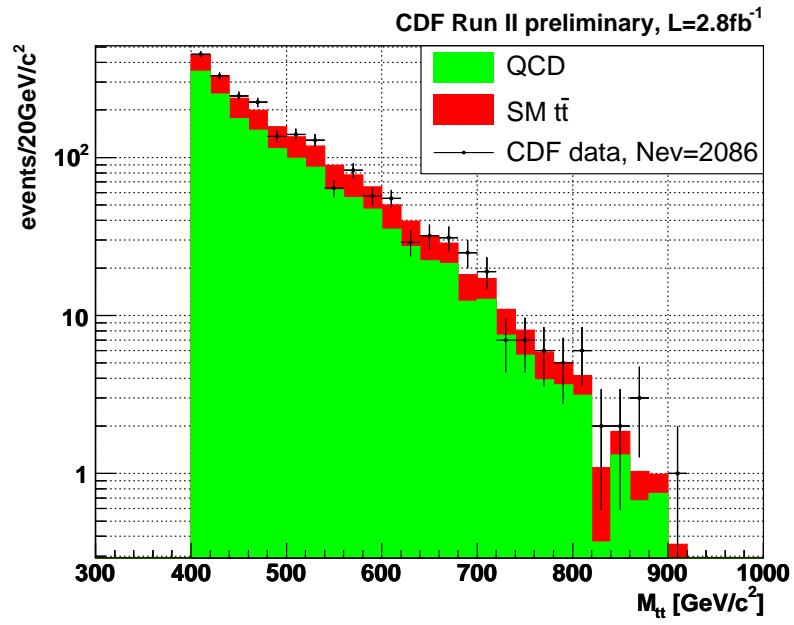
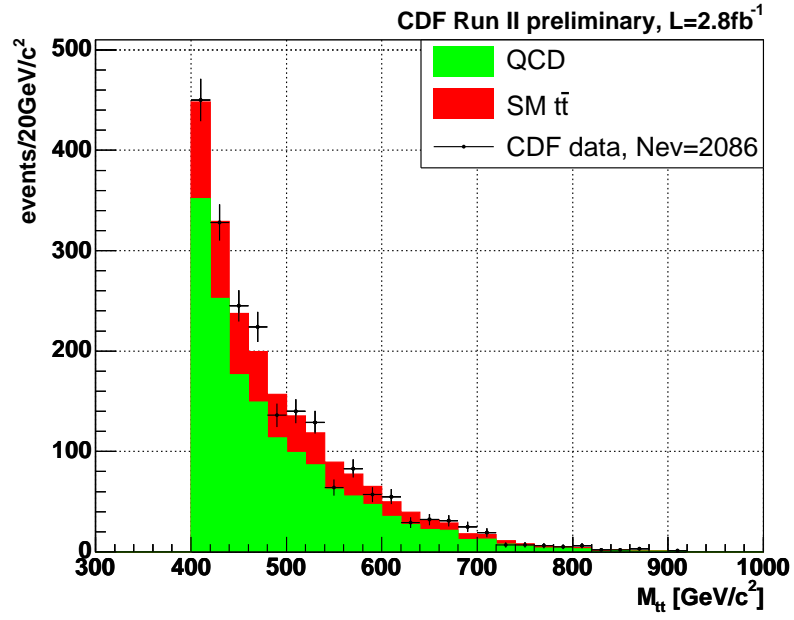


Figure 6-3. $M_{t\bar{t}}$ in CDF Run 2 data with coarser binning, 2.8 fb^{-1}

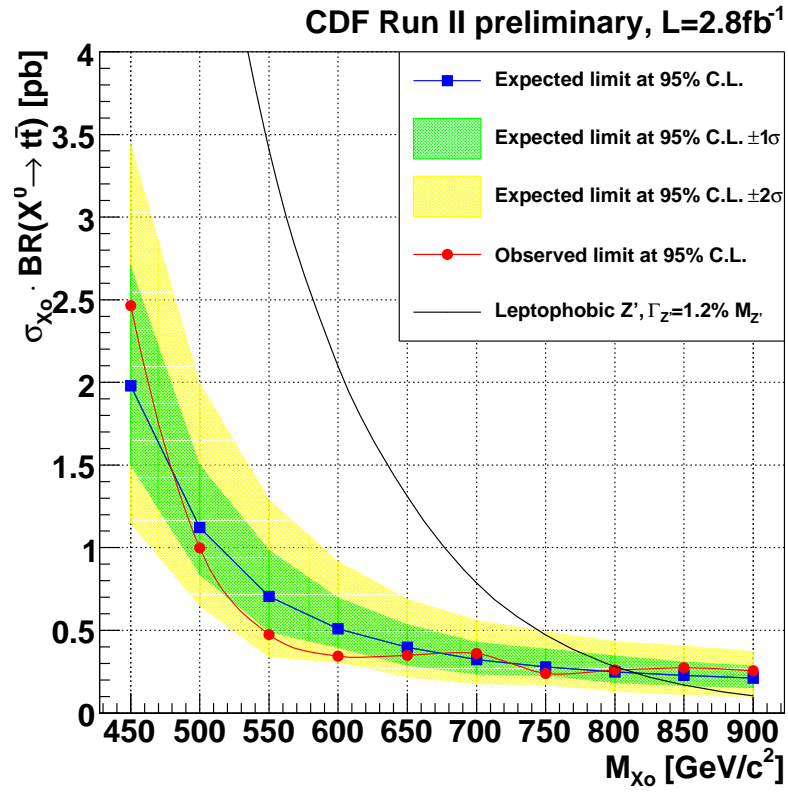


Figure 6-4. Resonant production upper limits in CDF Run 2 data, 2.8 fb^{-1}

REFERENCES


- [1] P. W. Higgs, Phys. Lett. **12**, 132 (1964).
- [2] F. Abe *et al.*, Phys. Rev. Lett. **74**, 2626 (1995); S. Abachi *et al.*, Phys. Rev. Lett. **74**, 2632 (1995).
- [3] A discussion of the motivation for a top quark inside the Standard Model can be found in: J.H. Kuhn, Lectures delivered at 23rd SLAC Summer Institute, (1995); hep-ph/9707321.
- [4] V.M. Abazov *et al.* (D0 Collaboration), Phys. Rev. D **67**, 012004 (2003).
- [5] T. Affolder *et al.* (CDF Collaboration), Phys. Rev. D **64**, 032002 (2001); Erratum-ibid. D **67**, 119901 (2003).
- [6] D. Acosta *et al.* (CDF Collaboration), Phys. Rev. D **71**, 052003 (2005).
- [7] D. Acosta *et al.* (CDF Collaboration), Phys. Rev. D **93**, 142001 (2004).
- [8] D. Chakraborty, J. Konigsberg and D.L. Rainwater, Ann. Rev. Nucl. Part. Sci. **53**, 301 (2003).
- [9] M. Cacciari *et al.*, JHEP **0404**, 068 (2004); N. Kidonakis and R. Vogt, Phys. Rev. D **68**, 114014 (2003).
- [10] [Tevatron Electroweak Working Group], (2009) [arXiv:hep-ex/0412071].
- [11] S.L. Glashow, J. Iliopoulos and L. Maiani, Phys. Rev. D **2**, 1285 (1970).
- [12] S. Eidelman *et al.*, Phys. Lett. B **592**, 1 (2004).
- [13] F. Abe *et al.* (CDF Collaboration), Phys. Rev. Lett. **79**, 3585 (1997); B. Abbott *et al.* (D0 Collaboration), Phys. Rev. Lett. **82**, 4975 (1999); T. Affolder *et al.* (CDF Collaboration), Phys. Rev. D **62**, 012004 (2000); V.M. Abazov *et al.* (D0 Collaboration), Phys. Rev. Lett. **88**, 151803 (2002).
- [14] LEP Electroweak Working Group, <http://lepewwg.web.cern.ch/LEPEWWG/>. To be published (2005).
- [15] P. Azzi *et al.*, CDF and D0 Collaborations and The Tevatron Electroweak Working Group, hep-ex/0404010.
- [16] ALEPH, DELPHI, L3 and OPAL Collaborations and The LEP Working Group for Higgs Boson Searches, Phys. Lett. B **565**, 61 (2003).

- [17] H. Haber and R. Hempfling, Phys. Rev. Lett. **66**, 1815 (1991); Y. Okada, M. Yamaguchi and T. Yanagida, Prog. Theor. Phys., **85**, 1 (1991); J. Ellis, G. Ridolfi and F. Zwirner, Phys. Lett. B **257**, 83 (1991); J. Ellis, G. Ridolfi and F. Zwirner, Phys. Lett. B **262**, 477 (1991); R. Barbieri and M. Frigeni, Phys. Lett. B **258**, 395 (1991).
- [18] S. Heinemeyer, W. Hollik and G. Weinglein, Eur. Phys. J. C **9**, 343 (1999); G. Degrossi, S. Heinemeyer, W. Hollik, P. Slavich and G. Weinglein, Eur. Phys. J. C **28**, 133 (2003).
- [19] S. Heinemeyer and G. Weinglein, hep-ph/0412214 (2004).
- [20] A review of dynamical electroweak symmetry breaking models can be found in: C.T. Hill and E.H. Simmons, Phys. Rept. **381** 235 (2003); Erratum-ibid. **390**, 553 (2004).
- [21] Fermilab Beams Division, **Run II Handbook**, http://www-bdnew.fnal.gov/pbar/run2b/Documents/RunII_handbook.pdf , (1999).
- [22] D. Acosta *et al.* (CDF Collaboration), Phys. Rev. D **71**, 032001 (2005) [arXiv:hep-ex/0412071].
- [23] The CDF II Detector Technical Design Report, Fermilab-Pub-96/390-E.
- [24] K. A. Bloom *et al.* (CDF Collaboration), “Track reconstruction for the CDF silicon tracking system”
- [25] J. Elias *et al.*, Nucl. Instrum. Meth. A **441**, 366 (2000).
- [26] S. Cabrera *et al.* (CDF Collaboration), Nucl. Instrum. Meth. A **494**, 416 (2002).
- [27] E. J. Thomson *et al.*, IEEE Trans. Nucl. Sci. **49**, 1063 (2002).
- [28] F. Abe *et al.* (CDF Collaboration), Phys. Rev. D **45**, 1448 (1992).
- [29] S. D. Ellis and D. E. Soper, Phys. Rev. D **48**, 3160 (1993) [arXiv:hep-ph/9305266].
- [30] A. Bhatti *et al.*, Nucl. Instrum. Meth. A **566**, 375 (2006) [arXiv:hep-ex/0510047].
- [31] T. Sjostrand, Phys. Lett. B **157**, 321 (1985); M. Bengtsson, T. Sjostrand and M. van Zijl, Z. Phys. C **32**, 67 (1986); T. Sjostrand and M. van Zijl, Phys. Rev. D **36** (1987) 2019.
- [32] R. Field, presented at Fermilab ME/MC Tuning Workshop, Fermilab, October 4, 2002; R. Field and R.C. Group (CDF Collaboration), arXiv:hep-ph/0510198.
- [33] G. Marchesini and B. R. Webber, Nucl. Phys. B **310**, 461 (1988); I. G. Knowles, Nucl. Phys. B **310**, 571 (1988); S. Catani, B. R. Webber and G. Marchesini, Nucl. Phys. B **349**, 635 (1991).

- [34] S. Weinberg, Phys. Rev. D **13** 974 (1976); L. Susskind, Phys. Rev. D **20** 2619 (1979).
- [35] C.T. Hill, Phys. Lett. B **266**, 419 (1991).
- [36] M. Cacciari et al., JHEP 0404:068 (2004); N. Kidonakis and R. Vogt, Phys. Rev. D **68**, 114014 (2003) .
- [37] D. Cronin-Hennessy, A. Beretvas, P.F. Derwent, Nucl. Instrum. Meth. A **443**, 37-50 (2000).
- [38] S. Van Der Meer *et al.*, Phys. Rep. **58**, 73 (1980).
- [39] R. Blair *et al.* (CDF Collaboration), Fermilab Report No. FERMILAB-Pub-96-390-E, Section 12 (1996).
- [40] D. Acosta *et al.* (CDF Collaboration), Phys. Rev. D **71** 032001 (2005).
- [41] D. Acosta *et al.* (CDF Collaboration), Nucl. Instrum. Meth. A **461** 540-544 (2001).
- [42] C.S. Hill *et al.* (CDF Collaboration), Nucl. Instrum. Meth. A **530** 1 (2004).
- [43] A. Sill *et al.* (CDF Collaboration), Nucl. Instrum. Meth. A **447** 1-8 (2000).
- [44] T. Affolder *et al.* (CDF Collaboration), Nucl. Instrum. Meth. A **453** 84 (2000).
- [45] T. Affolder *et al.* (CDF Collaboration), Nucl. Instrum. Meth. A **526** 249-299 (2004).
- [46] L. Balka *et al.* (CDF Collaboration), Nucl. Instrum. Meth. A **267** 272-279 (1998); S. Bertolucci *et al.* (CDF Collaboration), Nucl. Instrum. Meth. A **267** 301-314 (1998).
- [47] M. Albrow *et al.* (CDF Collaboration), Nucl. Instrum. Meth. A **480** 524-545 (2002); R. Blair *et al.* (CDF Collaboration), Fermilab Report No. FERMILAB-Pub-96-390-E, Section 9 (1996); G. Apollinari *et al.* (CDF Collaboration), Nucl. Instrum. Meth. A **412** 515-526 (1998).
- [48] A. Artikov *et al.* (CDF Collaboration), Nucl. Instrum. Meth. A **538** 358-371 (2005).
- [49] P. Gatti, “Performance of the new tracking system at CDF II”, CDF Note 5561.
- [50] W. Yao, K. Bloom, “Outside-In silicon tracking at CDF”, CDF Note 5991.
- [51] H. Stadie, W. Wagner, T. Muller, “VxPrim in Run II”, CDF Note 6047.
- [52] J.F. Arguin, B. Heinemann, A. Yagil, “The z-Vertex Algorithm in Run II”, CDF Note 6238.
- [53] CDF collaboration, Jet Energy Group, “Jet Energy Corrections at CDF”, CDF Note 7543.

- [54] A.A. Bhatti, K. Hatakeyama, “Relative jet energy corrections using missing Et projection fraction and dijet balancing”, CDF Note 6854.
- [55] B. Cooper, M. D’Onofrio, G. Flanagan, “Multiple interaction corrections”, CDF Note 7365.
- [56] A. Bhatti, F. Canelli, “Absolute corrections and their systematic uncertainties”, CDF Note 5456.
- [57] J.F. Arguin, B. Heinemann, “Underlying event corrections for Run II”, CDF Note 6293.
- [58] A. Bhatti, F. Canelli, L. Galtieri, B. Heinemann, “Out-of-Cone corrections and their Systematic Uncertainties”, CDF Note 7449.
- [59] R. Wagner, “Electron Identification for Run II: algorithms”, CDF Note 5456.
- [60] J. Bellinger, “A guide to muon reconstruction and software for Run 2”, CDF Note 5870.
- [61] D. Glenzinski, “A detailed study of the SECVTX algorithm”, CDF Note 2925.
- [62] D. Acosta, “Introduction to Run II jet probability heavy flavor tagging”, CDF Note 6315.
- [63] L. Cerrito, A. Taffard, “A soft muon tagger for Run II”, CDF Note 6305.
- [64] P. Azzi, A. Castro, A. Gresele, J. Konigsberg, G. Lungu and A. Sukhanov, “New kinematical selection for All-hadronic $t\bar{t}$ events in the Run II multijet dataset”, CDF Note 7717.
- [65] P. Azzi, A. Castro, A. Gresele, J. Konigsberg, G. Lungu and A. Sukhanov, “B-tagging efficiency and background estimate in the Run II multijet dataset”, CDF Note 7723.
- [66] MLPfit: A Tool for Multi-Layer Perceptrons,
<http://schwind.home.cern.ch/schwind/MLPt.html>.
- [67] R. Brun and F. Rademacher, <http://root.cern.ch/>.
- [68] Luc Demortier, A Fully Bayesian Computation of Upper Limits for Poisson Processes, CDF Note 5928
- [69] Luc Demortier, A Fully Bayesian Computation of Upper Limits for the CDF Higgs Search, Talk given at CDF Statistics Committee Meeting, July 23, 2004
- [70] CDF note 6888, ”Search for $t' \rightarrow Wq$ Using Lepton Plus Jets Events” R. Erbacher, R. Roser, J. Conway, A. Lath, R. Hughes, R. Marginean, E. Thomson, B. Winer

BIOGRAPHICAL SKETCH

 and applied to the Department of Physics at Tbilisi State University. In 2001 Iuri graduated with honors from Tbilisi State University with B.S. in Physics, *Summa Cum Laude*. During his bachelors studies, Iuri took a research assistant position at the Joint Institute of Nuclear Research in Dubna, Russia. In 2003 Iuri was admitted to graduate school at University of Florida. After completion of the course requirements, he moved to Fermilab in 2005 for research within the CDF collaboration under the supervision of Prof. Jacobo Konigsberg. His research was focused on t/\bar{b} resonance search in multi jets final state. He also played key role to the operations of the Cherenkov Luminosity Counter (CLC) at CDF.